DESIGN, DEVELOPMENT, AND MODELING OF A COMPACT, FIELD-GRADE CIVIL INFRASTRUCTURE CRACK DETECTOR DEVICE

By

Alisha M. Elmore

Submitted to the graduate degree program in Civil, Environmental, and Architectural Engineering and the Graduate Faculty of the University of Kansas in partial fulfillment of the requirements for the degree of Doctor of Philosophy.

Chairperson Dr. Stanley T. Rolfe

Co-Chairperson Dr. Ronald M. Barrett

Dr. Jian Li

Dr. Manuel A. Diaz

Dr. Steven D. Schrock

Date Defended: July 14, 2014

The Dissertation Committee for Alisha M. Elmore

certifies that this is the approved version of the following dissertation:

DESIGN, DEVELOPMENT, AND MODELING OF A COMPACT, FIELD-GRADE CIVIL INFRASTRUCTURE CRACK DETECTOR DEVICE

Co-Chairperson Dr. Stanley T. Rolfe

Co-Chairperson Dr. Ronald M. Barrett

Date Approved: August 28, 2014

ABSTRACT

Currently the nation's aging bridge infrastructure is approaching and in some cases exceeding its initial design life averaging more than forty years. Under these conditions steel bridges are susceptible to fatigue cracks at stress ranges below their material yield strength. In order to evaluate the remaining service life of these structures under their current operating conditions, it is important to accurately locate and identify active cracks within the material. Early detection of cracks and defects within a structure can provide inspectors and bridge maintenance personnel with viable information that can be used in the design and selection of an appropriate retrofit or repair technique that can be used to extend the service life of the bridge structure. Bridge inspections are typically conducted every two years primarily using visual inspection techniques. The active crack sensing tool designed and analyzed in this study is based on the robust and high sensing capabilities of piezoceramic materials. This dissertation presents the analytical, computational, and experimental results of a novel approach to identifying and characterizing cracks in steel bridge structural components using a piezoceramic sensor. Using the newly designed Piezoelectric Active Crack Tip Sensor (PACTS) tool, it was possible to detect an active crack with an opening displacement of 0.056 mm [0.0022 in] could be sensed under dynamic loading conditions. By using a crack opening linear trend (COLT) analysis, the crack tip position could be located within 3 mm [1/8 in] without the use of correction or modification factors. The results of the research provide a foundation in establishing an inspection tool capable of identifying damage detection within an in-service structure. The identification of an active crack and the ability to locate the crack tip of a material provides bridge inspectors and maintenance personnel with valuable information related to the current bridge condition that could be used for maintenance, repair, or replacement of bridges structures in an effort to ensure the safe passage of people and goods across the nation.

ACKNOWLEDGEMENTS

First and foremost, I would like to give all honor and glory to God our savior. Through him all things are possible. This dissertation would not have been possible without the time, energy, and support of so many people. I was fortunate to be in the right place at the right time to engage in this research study.

I am forever indebted to my committee chairs, Dr. Stanley Rolfe and Dr. Ron Barrett. Both of you took a chance on a new idea and encouraged me to pursue a research topic that was close to my heart and in-line with my future career goals and objectives. I am especially grateful to Dr. Stanley Rolfe for the financial support of me and my project. I would like to thank him for being an amazing and supportive professor, researcher, and advisor. His belief in me and my idea provided me with the strength to stay the course. Dr. Barrett, I doubt I have the words to fully express my appreciation for your technical expertise and your unwavering support. Your ability to facilitate interdisciplinary research and your appreciation for innovation and new technology reminded me why I entered a PhD program. Thank you for re-establishing my belief in research and its potential for real world development and application.

I would also like to thank my committee members Dr. Jian Li and Dr. Steven Schrock for allowing me think outside of the box and for providing me with clarification and technical advice throughout this project. Dr. Li, as a new member of the structures faculty your area of interest in SHM encouraged me to investigate and expand my research project. For his optimism, energy, and support of my academic career, I would like to extend my appreciation and thanks to Dr. Steven Schrock. Thank you for making me laugh, when I was on the verge of tears, and for your generosity in supporting my quest for knowledge.

Special thanks to my long distance committee member Dr. Manuel Diaz for his time, energy, guidance, and overall kindness during my graduate studies. You encouraged me to take this journey and I was fortunate to have you and your family along for the ride. Thank you for keeping me grounded in the real world during my theoretical adventures here at KU.

There are several KU students and faculty that helped make this research possible, whether by means of encouragement or discouragement. Both methods drove me to succeed and steadied my resolve.

I would like to thank the CEAE laboratory staff, Matt Maksimowicz, Eric Nicholson, and David Woody. Thank you for your willingness to help me in all of my destructive laboratory needs. Your eagerness to help me create things so that we could break them, always made me smile.

I would also like to take this opportunity to thank Dr. Glenn Light, Alan Puchot, and members of their NDE Technology Department group for allowing me to tour their facility and helping me navigate through the research process including how to accept and overcome research obstacles. Additional thanks to other SwRI members and groups including Dr. Steve Dellenback, Dr. Albert Parvin, Dr. Kevin Smart, and Dr. David Weiland. Your experiences and encouragement were greatly appreciated. Thank you for allowing me to view your projects and

understand the importance of research in developing new tools and techniques that have relevant real world applications and meet industry needs.

I would also like to extend a very special thank you to my friends and former professors Dr. Alberto Arroyo, Dr. Andrew Jones, Dr. Reginald Parker, and Dr. Richard Campbell for their support and words of encouragement that they have provided ever since my departure from their respective institutions.

To my family:

Mom, I could not have done this without all of your prayers and support. There is no way to I can list all the ways you helped me through this but I will try. Thank you for listening to me vent my frustrations; thank you for encouraging me to stick with it; thank you for keeping me on track when I would get tunnel vision and only focused on research; thank you for sending me money, flying me home, and making sure that I had some sort of quality of life; thank you for calling and encouraging me to be strong every day. When I was contemplating giving up, you were there to support me. Your belief in me helped me through a many of days. You struggled through this adventure with me every step of the way and although I will spend the rest of my life trying to repay you, there is no amount of money or time that could reimburse you for the unconditional love and support that you have given me. So I congratulate you on our accomplishment. Thanks.

Dad, thank you so much for your financial and technical support throughout this project. Thank you for allowing me to run through my data and experimental procedures for hours during my trips home. Your real world experience and technical skills were invaluable.

To my brother and my very special niece, thank you for providing me with a place to escape when I needed to step away and evaluate my progress. The trips to the zoo, Lego-Land, and Chuck-E-Cheese were always appreciated distractions.

Finally, I would like to thank my best friend, Karl Eisenacher, for his love and continuous support during my tenure at KU. Thank you for supporting me in my decision to engage in this uphill PhD battle. I appreciate all the trips you made to Kansas and of course the use of your travel miles so that I could return home when I needed a break. I would also like to thank you for all your help in organizing and finishing my dissertation including your amazing programming and CAD support during these critical times. This dissertation could not have been compiled without you.

This dissertation is dedicated to the memory of my grandmother, Mrs. Edith Dixon, my cousin Joseph “Bug” Robinson Jr., my friend and former classmate Tavius James, and my favorite bridge inspector Mr. Bill Loar. Although you could not be here physically to celebrate this accomplishment, the memory of your smiles, determination, love, and drive for success have helped motivate me to rise above the struggles and successfully complete this journey. The joy of this accomplishment belongs to all of you. Rest in Peace.

TABLE OF CONTENTS

LIST OF FIGURES

LIST OF TABLES

LIST OF ABBREVIATIONS

AASHTO -- American Association of State Highway and Transportation Officials
ACS -- Artificial Crack System
AE -- Acoustic Emissions
ASCE -- American Society of Civil Engineers
ASNT -- American Society of Nondestructive Testing
C_{ij} -- Elastic Stiffness Matrix
CLPT -- Classic Laminated Plate Theory
COD -- Crack Opening Displacement
Colt -- Crack Opening Linear Displacement
$C_{q\text{-stored}}$ -- Charged stored using the PACTS tool design circuit
CT -- Computed Assisted Tomography
D_{FH} -- Distance from PACTS Tool Centerline to Contact Surface
ε^{0}_{ij} -- Mid-plane Strain
ε_{ij} -- Strain
κ_{ij} -- Plate Curvature
E_b -- Bond Material Modulus of Elasticity
E_p -- Piezoceramic (PZT) Modulus Elasticity
E_s -- Substrate (Aluminum) Modulus of Elasticity
ET -- Eddy Current Testing
f -- PACTS Tool Excitation Frequency
FHWA -- Federal Highway Administration
G -- Shear Modulus of Rigidity
g_{31} -- Strain Developed per Applied Charge Density where stress is Applied in the 1-Direction and the Electrodes are Applied Perpendicular to the 3-axis
Gap -- Gap or Length of PACTS Tool Web
KDOT -- Kansas Department of Transportation
KU -- University of Kansas
LEFM -- Linear Elastic Fracture Mechanics
M_{ij} -- Resultant Laminate Moments
MT -- Magnetic Particle Testing
NBIS -- National Bridge Inspection Standards
NDE -- Nondestructive Evaluation

NDI -- Nondestructive Investigation
NDT -- Nondestructive Testing
NHI -- National Highway Institute
N_{ij} -- Resultant Laminate Forces
PACTS -- Piezoelectric Active Crack Tip Sensor
PAUT -- Phased Array Ultrasonic Testing
PAWS -- Piezoelectric Wafer Active Sensors
PE -- Pulse Echo
POD -- Probability of Detection
PT -- Penetrant Testing
PZT -- Lead-Zirconate-Titanate
Q_{ij} -- Reduced Elastic Stiffness Matrix
R -- Resistance
RT -- Radiography Testing
SHM -- Structural Health Monitoring
S_{ij} -- Compliance Matrix
t_b -- Bond Layer Thickness
t_p -- PZT Layer Thickness
t_s -- Substrate Layer Thickness
TT -- Through Transmission
U.S. -- United States
UT -- Ultrasonic Testing
v -- Poisson's Ratio
VI -- Visual Inspection
V_{piezo} -- Voltage in the PZT Layer
V_{sensed} -- Voltage Sensed by the PACTS System
VT -- Visual Testing
W -- Width of PACTS tool flanges
Δx -- Crack Opening Displacement

PAGE LEFT INTENTIONALLY BANK

CHAPTER 1: INTRODUCTION

1.1 Research Motivation

In 2013, the condition of the nation's bridge infrastructure was reported as "mediocre" and received a C+ in ASCE's Infrastructure Report Card. This rating is primarily due to the structural condition of the 607,380 bridges within the Federal Highway system and the growing cost associated with their condition (ASCE 2013). The average age of the United States' (U.S.) bridge infrastructure is forty-two years and nearly 11% of these structures are classified as structurally deficient (FHWA 2011). With the majority of these bridges exceeding their initial 50 year design life and replacement of each structure financially unfeasible, it is important to monitor and assess their structural capacity on a routine basis in order to identify maintenance and repair needs. Therefore, reliable and efficient inspection methods and techniques must be explored and developed to assist in the overall analysis of a bridges ability to maintain its structural stability under service loads.

Since approximately 30% (181,000) of the nation's bridge inventory are steel structures, it was determined that the development of a viable inspection tool could assist inspectors in the identification of active cracks within steel members. Early crack detection can assist bridge maintenance personnel in developing cost-effective maintenance and repair plans in lieu of high cost bridge replacements. Additionally, early crack detection allows bridge engineers to evaluate the remaining service life of the structure and prioritize repair and replacement needs based on available funding.

1.2 Research Objective

The objective of this dissertation was to evaluate the use of a Lead-Zirconate-Titanate (PZT) piezoceramic material as an active sensor in the detection and characterization of cracks in steel structures. PZT sensors were selected due to their ability to convert the small mechanical displacements into electrical signals including voltage or charge. The sensitivity of the PZT and design of the substrate geometry accurately identified active cracks in a material and the location of the crack tip. The design presented in this dissertation will provide bridge engineers an opportunity to conduct bridge inspections and detect crack growth without requiring large scale equipment. Additionally, the accurate identification of the crack tip location could assist bridge engineers and managers in the development and implementation of accepted repair techniques including the drilling of crack arrest holes.

The new Piezoelectric Active Crack Tip Sensor (PACTS) inspection tool was investigated through a proof-of-concept testing program that included experimental testing, numerical modeling, and closed form solutions. This research resulted in the development of a compact and portable crack detection system that can be used to monitor and investigate crack activity in metallic structural elements using piezoelectric materials.

1.3 Organization of the Dissertation

This dissertation is divided into seven chapters in addition to five appendices.

> Chapter 1 defines the motivation and research objective in addition to the organizational layout of the dissertation.

Chapter 2 identifies the background information related to the benefits of inspections and advanced nondestructive techniques used in the identification of cracks and defect within bridge structures. This chapter also presents a brief literature review of piezoelectric materials and their applications in bridge inspection and structural health monitoring techniques.

Chapter 3 summarizes the material selection process used to create the general design of the PACTS tool.

Chapter 4 outlines the modeling methods and techniques used for the PACTS tool analysis including finite element analyses and closed form solutions using classic laminated plate theory.

Chapter 5 is a presentation of the optimization process used to identify a tool geometry that would be used for experimental testing.

Chapter 6 is the Proof of Concept section that presents the finite element analysis and test results that illustrate the sensing capabilities of the PACTS tool.

Chapter 7 provides a summary of the research findings, conclusion, and a recommendation of future work.

The five appendices provide additional details related to the tool material properties, finite element analysis input parameters, test and manufacturing procedures, design plans, optimization results, and the raw data from experimental testing.

CHAPTER 2: LITERATURE REVIEW & BACKGROUND

The development of a new inspection tool and sensor required a fundamental understanding of fatigue and fracture concepts, types of bridge inspections, and bridge inspection methods currently in use. This chapter will provide a brief overview of fatigue and fracture including its application in the analysis of in-service structures. Afterwards, the identification of the bridge inspection types and inspection methods used will be presented, including current applications of PZT in the in the inspection of existing structure.

2.1 Fracture Mechanics Overview

Steel structures are subjected to routine inspection in order to identify discontinuities within the material of structural members. Discontinuities can include variations in microstructure, cracks, laps, and inclusions. This section provides an introduction into the area of fatigue and fracture mechanics and the effects of crack lengths and location on the integrity of structural components. Cracks are considered narrow planar discontinuities in a materials that were previously or should be continuous (Hellier 2013). Cracks are typically the result of fabrication techniques, event-induced damage, or the effects of continuous operation under service conditions. They can appear as surface, subsurface, and internal cracks.

When dealing with fracture mechanics or fatigue, it is important to understand the difference in ductile and brittle material failure. Ductile materials undergo and are primarily dominated by a yielding period prior to fracture and/or breakage, while brittle materials have little if any yielding or deformation prior to failure. Brittle fracture is a type of failure in structural materials that usually occurs without prior plastic deformation and at extremely high speeds, up to 2133 m/s [7000 ft/s] in steels (Barsom and Rolfe 1999). They occur with little or no elongation or reduction in area and with very little energy absorption. Primarily design considerations prefer ductile materials that may exhibit some signs of distress while undergoing yielding prior to ultimate failure. Since the failure of most structures including bridges, buildings, airplanes pose a significant danger to public health, safety, and welfare, it is important to inspect and monitor cracks or other discontinuities within these structures.

2.1.1 Fracture Mechanics

Fracture mechanics, in general, is the study of cracks and crack propagation. It plays a significant role in improving the performance and life of mechanical structures and their components. Fracture mechanics applies strength of material properties including stress and strain to assist in the design and maintenance of various structures. When discussing fracture mechanics, it is important to identify the primary modes or movements of crack surfaces. There are three types of crack surface displacements (Figure 2-1). In Mode I or *opening mode*, the two fractured surfaces are perpendicular to each other and are being “pulled” in opposite directions and appear to open the crack. In Mode II or *shear mode*, the two fracture surfaces slide over each other perpendicular to the crack. This mode appears to attempt to “shear” off the two surfaces. Mode III or *tearing mode*, is where the two surfaces slide over each other in a direction parallel to the crack front (Barsom and Rolfe 1999). Mode III produces a “scissoring motion” at the crack front (Sanford 2003). Primarily Mode I, opening mode, is considered the most important mechanism controlling failure, since growing cracks tend to position themselves in a direction to minimize or eliminate the effects of Mode II and III (Sanford 2003). This research and proof of concept study focused on Mode I crack surface displacements.

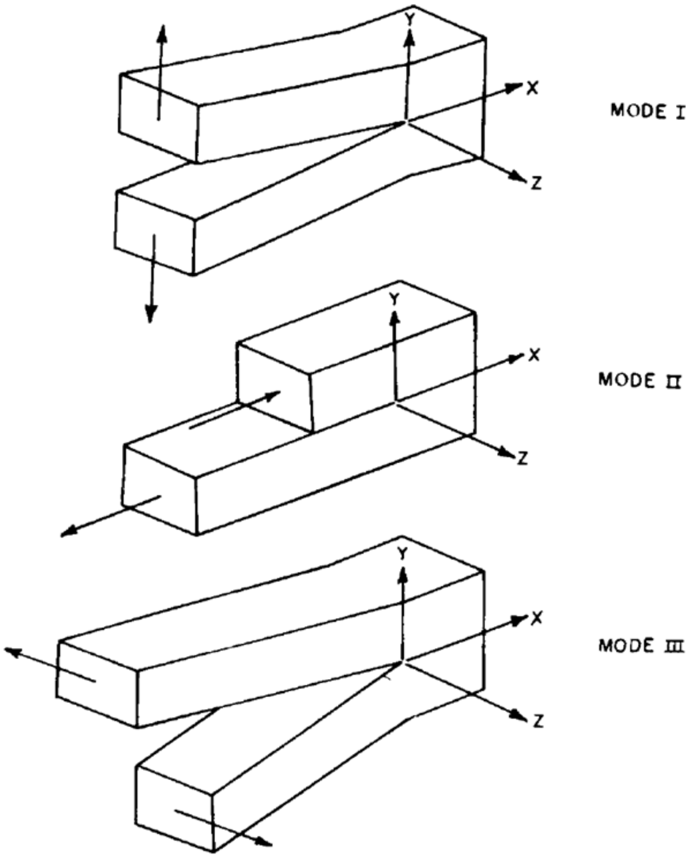

Figure 2-1: Three basic modes of crack surface displacements (Barsom and Rolfe 1999).

A number of large structures including aircraft, pressure vessels, buildings and bridges have initial imperfections that resemble cracks. These imperfections can be sharp notches or discontinuities in the material. Fracture mechanics can be used in the design, inspection, and forensic analysis of these types of structures. Fracture mechanics allows engineers to determine allowable stress levels on a structure with a known flaw size; to determine inspection times by allowing engineers to calculate the critical crack size at failure for a member; and it can be used to determine the fatigue crack growth rate to establish an acceptable design life of a new structure or the fatigue life of a pre and post in-service structure. The use of fracture mechanics after a structural failure in forensic analysis can help identify crack initiation points which could potentially establish responsibility and accountability of any catastrophic failures.

The implementation of fracture mechanics principles in design and analysis procedures can be instrumental in providing safe and cost effective structural elements and facilities. The concepts of fracture mechanics can be simplified into basic engineering principles including stress, strain, and material properties. The driving force for fracture mechanics is the stress intensity factor, K_I, which is analogous to the calculated nominal stress. The relationship between stress intensity factor, K_I, the applied stress, σ, and the crack size, a, for three crack geometries is shown in Figure 2-2. The Edge Crack geometry was used to analyze the effectiveness of the PACTS tool.

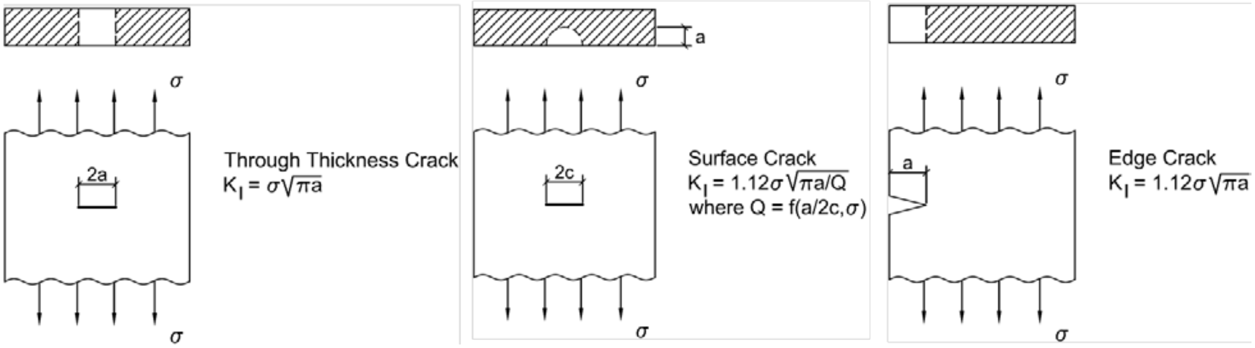

Figure 2-2: Stress Intensity factor, K_I, values for different crack geometries (Barsom and Rolfe 1999).

The resistance force or the fracture toughness, K_C, is a material property similar to the yield strength of materials used in design. Fracture toughness is the amount of energy a material can absorb before brittle failure. It describes the material's resistance to fracture and can be determined by integrating the area under the stress-strain curve or experimentally using ASTM International test standards (2012). K_I and K_C can be used in the design and assessment of structures by assisting engineering in determining allowable stress ranges, critical flaw sizes, and selecting materials that would optimize the design of metal structures (Figure 2-3).

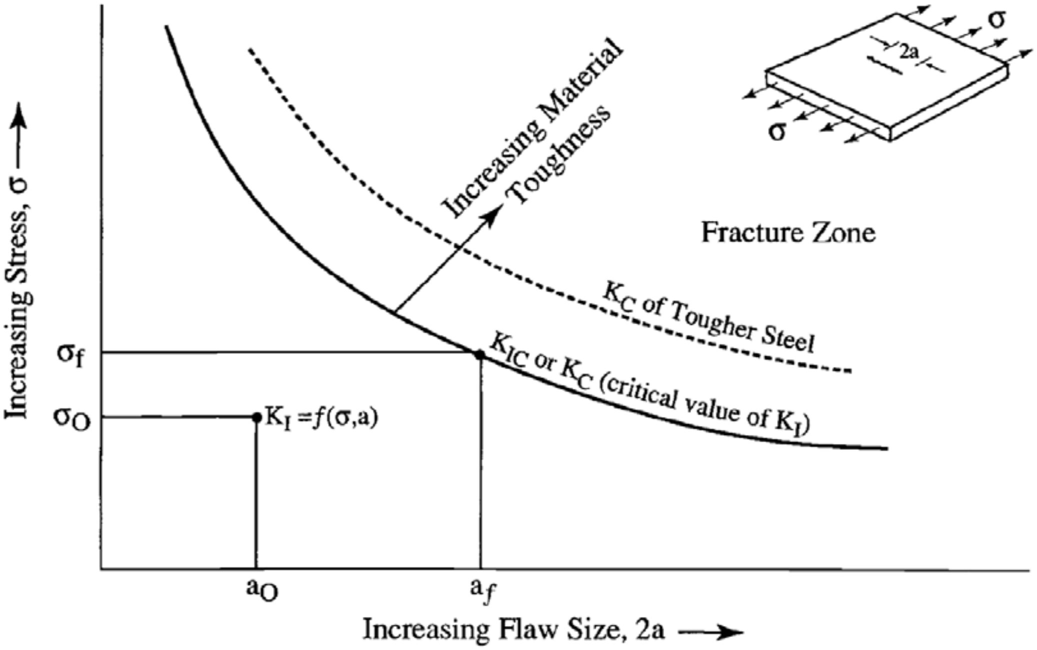

Figure 2-3: Relationship between stress, initial flaw size, and material toughness (Barsom and Rolfe 1999).

2.1.2 Fatigue

In the previous section the fracture behavior was outlined for flaws under monotonically increasing loads. However, most structures including bridges, ships, and aircraft are subjected to repeated loads that may fluctuate in magnitude (Barsom and Rolfe 1999). Fatigue damage in structures occurs due to repeated loading that is usually below the allowable yield strength of the material used. This occurs due to stress risers or regions where the localized stress exceeds the yield stress of the material. Stress risers can include welds, imperfections, and geometrical changes in non-welded components. After numerous cycles of load fluctuation, the localized material damage can initiate a fatigue crack and then propagate the crack throughout the member. Fuchs and Stephens stated in their 1980 text that "*the ultimate cause of all fatigue failures is that a* *crack has grown to a point at which the remaining material can no longer tolerate the stresses or strains, and sudden fracture occurs*" (1980). The total fatigue life of a structure, N_t, includes the number of loading cycles required to initiate a crack, N_i, and the number of cycles to propagate the crack, N_p (Equation 2:1).

$$N_t = N_i + N_p \qquad \textbf{Equation 2:1}$$

When analyzing fatigue crack growth, it is important to note that the crack propagation rate is dependent on the change in crack size (Δa) and the applied stress range (Δσ). Therefore accurate and quality inspection reports identifying cracks and crack growth can be used in evaluation of fatigue life and propagation, thus assisting maintenance departments in determining retrofit, repair, or replacement requirements for their structures inventory.

Based on the information used to determine the fatigue life and the relationship between the applied stress, flaw size, and fracture toughness (Figure 2-3), it can be concluded that to increase the fatigue life of a structure, a designer should consider lowering the stress range (Δσ), minimizing the flaw size (Δa), or increasing the fracture toughness of the materials used. Literature indicates that reducing the flaw size or the stress range for structure provides a larger effect on the fatigue life then increasing the toughness of the material (Barsom and Rolfe 1999; Fuchs and Stephens 1980; Sanford 2003). However, in order to decrease the applied stress range of an in-service bridge structure, it typically requires restricting traffic loads by reducing the posted load limit of the bridge. This method is effective at extending the fatigue life, but it is not a viable option in rural or remote locations where alternative routes are unavailable. Therefore, early crack identification is a significant factor in establishing and extending the fatigue life of a structure. Early crack identification can be used by bridge engineers in the design, selection, and application of feasible retrofit materials and techniques, which could result in the use of higher K_C materials that can increase fatigue life. Therefore, proper inspections that accurately identify and characterize cracks can be used to analyze and monitor the structural performance and fatigue life and minimize the potential effects and disruptions to traffic patterns and commute times.

2.1.3 Fitness for Service

The same principles and practices used in design to prevent fracture failure can be used to evaluate in-service bridges and potentially extend service life. The average age of the nation's bridges is forty two years and they are steadily approaching their initial design life (FHWA 2011). A Fitness for Service assessment considers the age of a structure in addition to its actual in-service loading conditions, crack or flaw sizes, and the material toughness (Wells 1981). Fitness for Service was initially described by Alan Wells in the early 1960s and more recently referred to as "common sense engineering" by Stanley Rolfe (1993). Fitness for Service analysis can be conducted pre or post in-service conditions. Although there are no specific guidelines for the fitness for service procedure in bridge inspections, the American Society for Mechanical Engineers (ASME) has outlined a procedure using fracture mechanics principles to determine the maximum acceptable flaw size that can be tolerated before exceeding allowable values in nuclear power plant components (2010). The fundamental first step of their procedure includes performing a quality inspection that identifies and characterizes actual flaw sizes and locations. However, in order to successfully identify cracks it is important to identify the types of inspections conducted on in-service bridge structures.

2.2 Types of Bridge Inspections

Inspection of transportation structures assists owners in ensuring the safe passages of people and goods across the federal highway system. If properly conducted and documented, regular and sporadic inspections of bridges can help ensure the structural integrity of its members and provide pertinent information necessary to properly maintain each structure. Throughout the life of a bridge structure, the type of inspection conducted may vary depending on the structural integrity and age of the structure and its members. In accordance to the American Association of State Highway and Transportation Officials (AASHTO) Manual for Bridge Evaluation, there are seven bridge inspection types (2008).

- Initial Inspection

  An Initial Inspection is the first inspection conducted on a new or widened bridge structure. This inspection identifies the required information regarding the bridge geometry, layout, and length that is recorded in the structure's inventory record. Additionally, it defines the baseline condition of the bridges structural members and identifies any existing problem.

- Routine Inspection

  A Routine Inspection is a periodic inspection conducted on a regularly scheduled basis. This inspection type is used to determine the physical and functional condition of a bridge. Current conditions are compared to previous Routine and Initial inspection condition ratings to ensure the bridge meets its serviceability requirements. Routine inspections are typically conducted from the ground or deck level and may not include a hands-on inspection of individual structural members. It provides a cursory inspection of the overall structure. Routine inspections are required and satisfy the National Bridge Inspection Standards (NBIS) requirements for periodic comprehensive inspections of in-service structures.

- In-Depth Inspection

  In-Depth Inspections include a hands-on inspection of one or more bridge members. They are also conducted in order to identify potential deficiencies that were not investigated or detectable during Routine Inspections. In-Depth inspections may require the use of additional nondestructive testing (NDT) techniques outside of visual inspection.

- Special Inspection

  Special Inspections are conducted in order to evaluate and monitor known defects or conditions, including areas susceptible to distortion induced fatigue cracking and foundation settlement or scour. Since the inspected area is localized, Special Inspections do not meet the NBIS requirements for comprehensive periodic inspections. The inspections are typically conducted by inspectors familiar with potential consequences of the deficiency and skill in the inspection method required to adequately evaluate the structural performance.

- Fracture-Critical Inspection

  Fracture-Critical Inspections are performed on steel bridges with fracture critical members whose failure would probably result in the inability of the bridge structure to perform its load carrying function and/or the collapse of a portion or the entire bridge. This inspection type includes the identification of fracture critical members and the development of a plan to inspect these members.

- Underwater Inspection

  Underwater Inspections are conducted on channel crossings to locate the bottom of the channel and determine the structural integrity of underwater substructure components, by identifying and evaluating scour and undermining conditions. This inspection type can be conducted from above the water surface level for shallow crossings but may require diving or other techniques in deeper waters.

- Damage Inspection

  Damage Inspections are unscheduled inspections conducted in order to assess the structural damage resulting from environmental factors including hurricanes and earthquakes in addition to human actions such as over height truck strikes of low clearance bridge structures as illustrated in Figure 2-4. The primary goal of Damage Inspection is to determine if there is a need for further action including structural repair and/or emergency load restrictions, or replacement.

Figure 2-4: Tractor trailer collision resulting in a non-scheduled Damage Inspection to evaluate the structural integrity of the steel deck plate girder bridge. (Photo Credit: A. Elmore, NY)

Each inspection method described in this section requires trained and qualified personnel and all inspections should be documented and filed for future review. During inspections, where cracks are identified, it is important to properly characterize each crack by documenting the crack location, length, and size.

2.3 Civil Infrastructure Inspection Methods

Routine inspections are typically conduced every two years on bridge structures within the United States (U.S.). Although the U.S. has approximately 200,000 steel bridges, visual nondestructive evaluations (NDE) are still the primary inspection method used, with occasional validation performed using dye penetrant and magnetic particle tests (FHWA 2011; NDEC 2010). The probability of detection (POD) using visual techniques varies greatly and may be highly impacted by human behavior and environmental factors and conditions (FHWA 2001; Hellier 2013). Advanced NDE methods used in the inspection of steel bridge structures include ultrasonic, eddy current, radiography, and acoustic emissions These advanced methods have been investigated by the Federal Highway Administration's (FHWA) NDE Center, and have been successful in helping to identify surface or near-surface cracks on steel bridge systems (NDEC 2010). However, the usage of these advanced techniques is limited to "special," non-routine bridge inspections. During routine inspections, bridge inspectors typically visually identify cosmetic imperfections that appear to be "active" cracks then document and recommend the use of advanced techniques to verify and characterize cracks and volumetric changes within the structure.

Nondestructive Testing Evaluation or Testing (NDE/NDT) techniques used for structural evaluation allow inspectors and maintenance personnel to evaluate the structural condition and/or integrity of the bridge without invasive destructive testing requirements. NDT methods can identify maintenance and repair needs during inspections and helps to identify structural health monitoring (SHM) needs which involves providing continuous monitoring of in-service structures. The NDE methods outlined in this section include visual, dye penetrant, magnetic particle, eddy current, and radiography test methods. Additionally, piezoelectric materials are introduced and their application in ultrasonic and acoustic emissions testing.

When considering the effectiveness of inspection techniques used, the probability of detection (POD) is the method generally used. POD is the probability of detecting a given crack or discontinuity under specific conditions and techniques. Although, the POD values vary depending on the method or technique used, it is important to note that generally the POD of an inspection method increases with increasing flaw or crack size. Figure 2-5 illustrates that as the normalized flaw size increases, using eddy current array (ECA) test, the POD curve approaches one, where defects are always detected. Each NDE method has a detection limit where the POD is small and approaches zero.

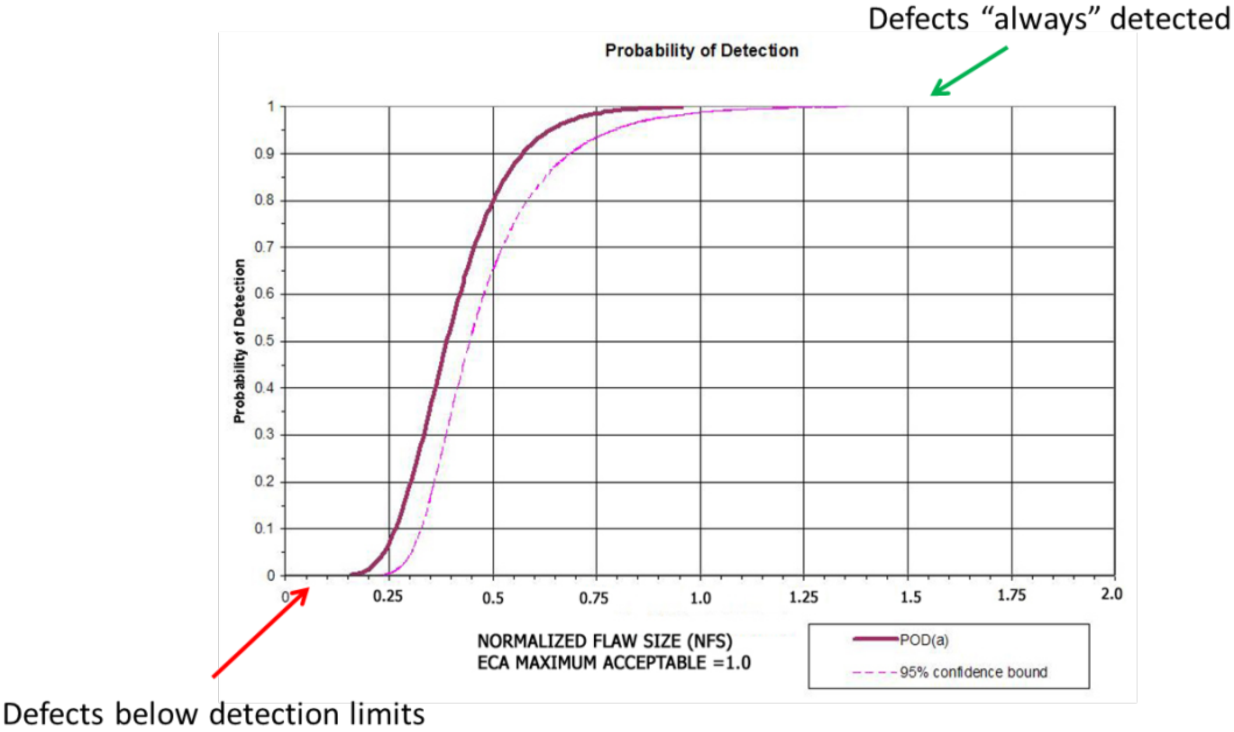

Defects “always” detected

Defects below detection limits

Figure 2-5: Probability of detection curve with 95% confidence bound for eddy current array inspection method (HSE 2006).

The literature review of NDT methods used in the inspection of in-service steel bridges is not intended to be an all-inclusive list. It primarily focuses on the current and most common techniques used specifically for the inspection of steel bridge superstructures in addition to those specifically identified and used by the Kansas Department of Transportation (KDOT).

2.3.1 Visual Inspection

Visual Inspection (VI) methods evaluate the presence of surface discontinuities with the use of normal eyesight alone or the addition of optical instruments including magnifying glasses, artificial light, and or mirrors. VI is the most commonly used method of structural evaluation and is considered a cost effective means of evaluating surface discontinuities of various structural components or an entire bridge system (FHWA 2001; Hellier 2013; Purvis 1988; Whisler 2013). Typical discontinuities identified using VI methods include corrosion, the misalignment of parts, physical and cosmetic damage, and surface cracks. VI is the initial safe guard in minimizing crack growth and brittle failure. The results of VI are used in the monitoring of bridge condition and scheduling of bridge maintenance.

In 2001, the FHWA published a report that investigated the reliability of visual inspection. During their investigation, 49 inspectors from 25 state transportation agencies were evaluated. It was determined that the inspection reports had “significant variability” between inspectors. The variation in assigned bridge condition ratings correlated with individual inspectors’ Fear of Traffic, Visual Acuity and Color Vision, Light Intensity, Inspector Rushed Level, and the perceptions of Maintenance Complexity, and Accessibility (FHWA 2001). It was also noted that the independent use of VI for In-Depth or Special Inspections may not identify any deficiencies outside of those located during Routine Inspections.

Although VI results and observations vary, its significance in the area of bridge inspections was adequately described by Purvis in the following statement:

> "In most situations the only method available to detect flaws in a bridge member is visual inspection. It is important to identify the flaws early in the typical crack-development scenario. If the defect is identified as soon as it can be seen by the inspector, the service life of the member often has been reduced by more than 80 percent (Purvis 1988)."

VI is the first method of defect detection used within the inspection industry. VI can be a low cost effective means of inspection. Training requirements are primarily experience based and require little advanced training. However, VI results can vary depending on the inspector's ability and overall thoroughness. Using the method of VI, may require that the area to be inspected be cleaned including the removal of debris, paint, or rust. Additional lighting or other optical stimulation may be required to adequately inspect critical areas. Inspectors using this method should be familiar with the area susceptible to cracking; be able to identify the crack; and be willing to get close enough to visually see the crack. Cracks identified using VI are typically validated using advanced inspection techniques.

2.3.2 Advanced Techniques

2.3.2.1 Liquid or Dye Penetrant

The application of a viscous liquid or dye to the surface being inspected enhances the appearance of surface discontinuities in solid nonporous materials. Penetrant testing (PT) utilizes capillary action of the surface to pull penetrant into the surface discontinuities. The application of PT is used in detection of sharp fatigue cracks and is usually selected based on the results of VI. Properly used PT can also help determine the extent of a crack already identified by VI. Dye penetrant is one of the two standard practices used by the FHWA and KDOT for the inspection of steel girders where fatigue cracks are a concern (Jalinoos 2009; Whisler 2013). Visible and fluorescent penetrants are available for PT inspections. At a minimum, fluorescent penetrant testing will require penetrant, cleaner, and a black light. Under the illumination of black light, a visual contrast between the crack and the material surface is observed (Figure 2-6). Automated PT equipment is available and primarily used in manufacturing production quality assurance.

PT is a portable, low cost, and sensitive technique used in the detection of surface discontinuities in solid nonporous material. However, its effectiveness can be impacted by surface conditions and preparation. PT has been used effectively in small localized areas; however, their application on large scale sections has been classified as impractical, time consuming, and "messy" (FHWA 2012; Hellier 2013; Whisler 2013). Although PT training requirements are minimal, the results of the PT testing should be analyzed by experienced inspectors.

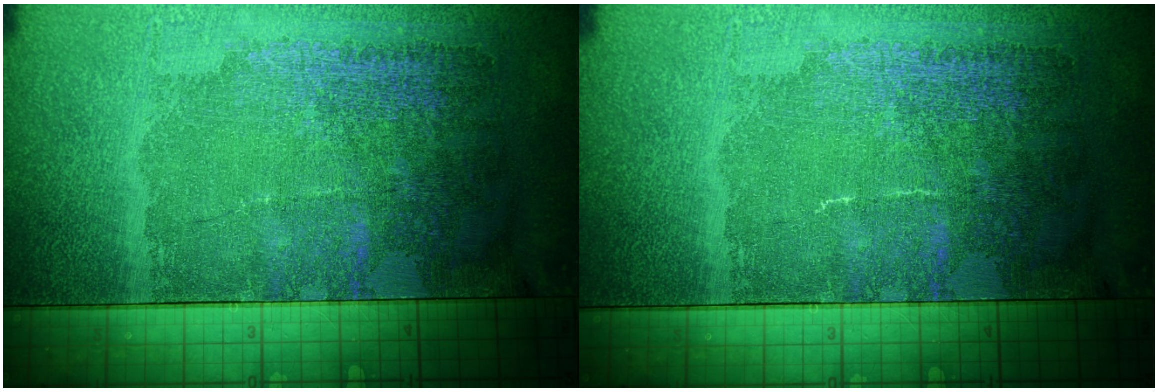

Figure 2-6: Penetrant testing used in the detection of distortion induced fatigue cracks in a steel girder under dynamic load.

2.3.2.2 Magnetic Particle

Similarly to PT, magnetic particle testing (MT) is used in combination with VI in order to locate surface and near-surface discontinuities in materials that are capable of being magnetized. In MT, a magnetic field is applied to the material surface, then iron or magnetic iron oxide particles are sprayed over the magnetized surface. The magnetic particles attach to the edges of the defect in order to reveal its location. In dark non-illuminated areas, the location of the attached fluorescent particles can be determined using ultraviolet light, therefore producing a visual contrast between the particles and the material surface (Hellier 2013; Jalinoos 2009). Additionally, magnetic particle is one of the two standard practices used by the FHWA for the inspection of steel girders where fatigue cracks are a concern (Jalinoos 2009).

MT advantages include rapid test results within minutes of particle application and easily interpretable results for surface and near surface discontinuities. MT is a versatile technique where variations in particle sizes can identify different crack sizes and provide sharper imaging. Similarly to PT, MT has been used effectively in small localized areas; however, their application on large scale sections has been classified as impractical and time consuming (FHWA 2012; Hellier 2013; Whisler 2013).

2.3.2.3 Eddy Current

Eddy Current testing (ET) uses an electrical circuit or coil to create a magnetic field. The coil is then placed over a conductive material where opposing alternating currents, or eddy currents, are generated. When the generated current flow is obstructed by a defect, it results in a change in the electromagnetic field. Eddy current electromagnetic field changes can be identified on an oscilloscope.

ET is one of the primary NDE tools used on steel structures to identify surface and near surface cracks (Jalinoos 2009; Whisler 2013), especially at weld connections. When properly positioned, ET can accurately locate defects and identify the crack tip. In order to correctly locate and identify defects using ET, the defect must cross the eddy current flow as shown in Figure 2-7. However, the probes sensitivity to magnetic particles including weld materials can influence ET results. Other limitations include the training requirements to operate and interpret ET results as well as high equipment cost. ET testing is a time consuming method of inspection that requires large equipment and focuses on localized areas (Hellier 2013; Whisler 2013).

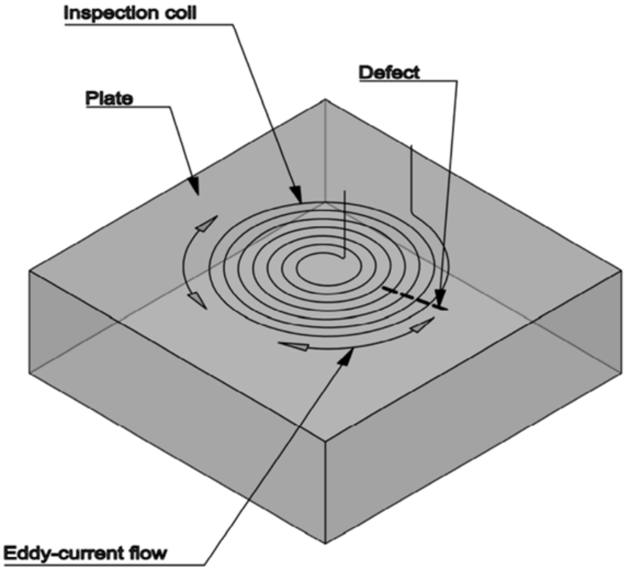

Figure 2-7: Pancake - type coil applied to a flat surface with the defect crossing the eddy currents.

2.3.2.4 Radiography

Radiography is a through transmission inspection tool that provides a volumetric inspection of a solid surface by penetrating x-rays or gamma rays through the material. In traditional scans, the through transmission results appear on the radiographic film located on the other side of the test specimen Figure 2-8. However, if only one side of the material is accessible, a backscatter technique can be employed. Radiography testing (RT) use is limited due primarily to radiation exposure safety concerns. Exposure time, dosage, and the distance from the source should be monitored to limit potential adverse radiation effects.

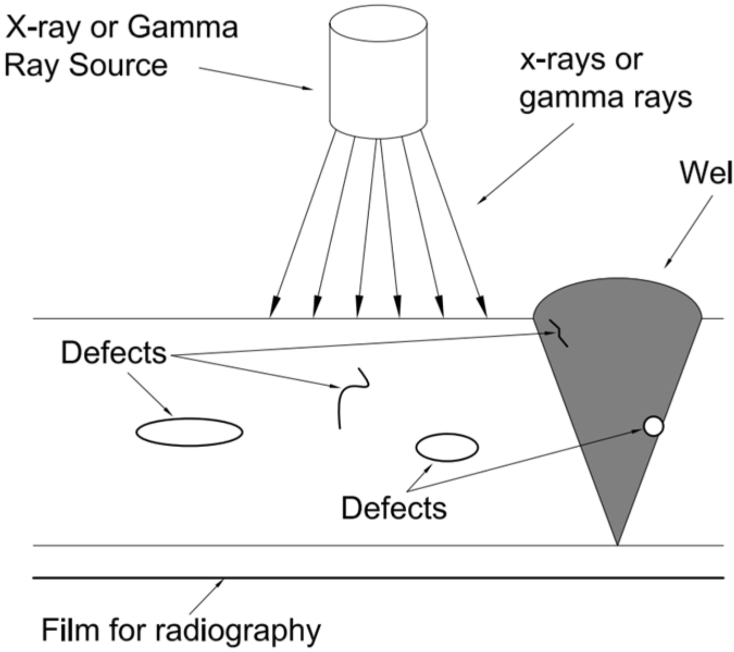

Figure 2-8: Image of Radiography test set-up.

Computed Assisted Tomography (CT) is a radiographic method that uses penetrating radiation from radioisotope or x-ray tube sources. These results produce cross-sectional images that include variations in material density. Similarly to radiography, CT sensitivity requires proper alignment of the radiation beam and the flaw or discontinuity. Therefore, there is difficulty in detecting cracks that were not located and characterized during previous inspections or using alternate techniques.

Various industry applications have employed radiographic inspection techniques, including manufacturing, food processing, shipping and RT is well known for its airport security applications. Radiography is not a primary inspection technique used by KDOT. However, it provides quality images and documentation on volumetric defects within the material.

The quality of the images produced by RT can be affected by the characteristics of the imaging plate. Improvements on the effectiveness of the imaging plate can be achieved by increasing the plate thickness. However, an increase in plate thickness would result in a decrease in image resolution (Silva et al. 2014).

2.4 Piezoelectric Materials and Inspection Applications

2.4.1 Fundamental Properties of Piezoelectric Elements

Piezoelectric materials are those materials that are capable of converting mechanical movement into electrical outputs and vice-versa. This phenomenon is commonly referred to as the piezo-effect and it is limited to specific crystalline structures. Demonstrated and explored by Pierre and Jacques Cure in 1880, piezoelectric materials have been used in NDT application within aircraft, civil, and pipe structures. Piezoelectric materials are typically lightweight, low cost, brittle materials with high sensitivity. The fundamental property of piezoelectric materials allows it to be used in various applications as an actuator or a sensor. As an actuator, the piezoelectric material is subjected to an applied voltage which results in a mechanical displacement of the material. Conversely as an actuator, a mechanical strain can be applied to the piezoelectric material which results in a voltage or electrical change in the material.

Natural and synthetic piezoelectric materials are available in various sizes and sensitivities. Natural piezoelectric materials include quartz and tourmaline and synthetic piezoelectric ceramic materials include those composed of Barium-Titanate and the most commonly used Lead-Zirconate-Titanate (PZT). PZT and other manufactured polycrystalline ceramics are available in various geometries and can be produced with specific chemical and piezoelectric characteristics (Morgan Advanced Materials 2009; Piezo Systems Inc. 2011). Piezoelectric materials and devices can be found in cigarette lighters, grill igniters, smoke detectors, fish finders, and audio transducers.

In the field of NDE, piezoelectric transducers are commonly used to inspect bridge superstructure components, including pins, rollers, and gusset plates. They are also used in the SHM of steel structures to identify and monitor crack growth. Piezoceramic transducers convert electrical energy into acoustical energy. This phenomenon is commonly used in the field of bridge inspections in the form or Ultrasonic Testing and Acoustic Emissions.

2.4.1.1 Ultrasonic Testing

Ultrasonic Testing (UT) transmits high frequency sound waves through a material to identify cracks, voids, and other discontinuities in the material. When a discontinuity is in the path of the sound wave, part of the energy will be reflected back from the flaw surface. Then the reflected wave is transformed into an electrical signal by the transducer and displayed on an oscilloscope. UT is a versatile tool that can be used when access to both sides of the specimen is available using through transmission (TT) or when access to one side is limited using pulse echo (PE).

UT is primarily used for pin, bolt, and weld inspections. UT imaging can provide length and thickness measurements of discontinuities. In addition to surface discontinuities, UT is capable of detecting subsurface discontinuities in various structural elements including pressure vessels, piping, aircraft, machinery, and bridges.

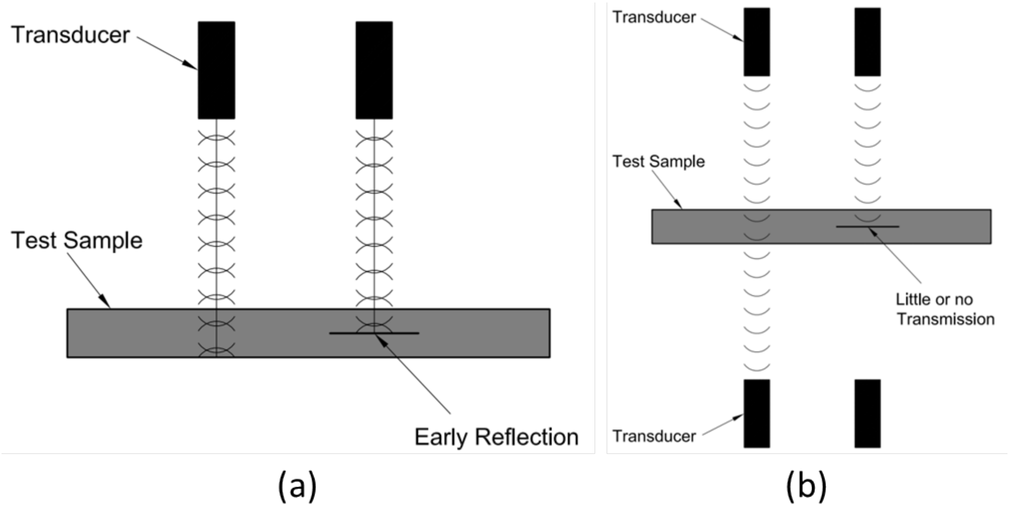

Figure 2-9: Effect of defect on wave propagation in the material using (a) Through Transmission (TT) and (b) Pulse Echo (PE) ultrasonic testing applications.

Currently Phased Array Ultrasonic Testing (PAUT) is the UT method of choice used for the detection of cracks by the FHWA's NDE facility (FHWA 2012). PAUT systems contain multiple arrays of ultrasonic transducers. The use of multiple transducers provides a cross section view of the material to help accurately identify and characterize defects.

UT is highly accurate and sensitive to surface and subsurface discontinuities. UT requires minimal surface preparation and provides immediate results. However, UT testing requires high cost equipment and extensive training in order to accurately identify discontinuities and analyze test results (Hellier 2013; Whisler 2013).

2.4.1.2 Acoustic Emissions

In the field of SHM, Acoustic Emissions (AE) is one of the commonly used tools for steel highway structures and has shown great promise due to its ability to sense or detect sudden energy releases within a material (FHWA 2012; Hellier 2013). The energy released is in the form of acoustic stress waves. The use of AE as a SHM system allows for continuous monitoring of the structure without requiring direct access to the crack. However, under continuous monitoring applications AE only estimates crack growth and should be used with other NDE methods to successfully characterize crack sizes.

2.4.1.3 Other Applications

In addition to basic UT and AE applications, piezoelectric materials are commonly used as actuators and sensors; however, the sensing ability has proven to be highly effective in strain sensing applications. Similarly to traditional foil strain gages, PZT sensors are capable of accurately measuring strain levels; however, PZT sensors tend to show higher sensitivity to low strain levels than foil strain gages (Chopra and Sirohi 2013). Research results have shown that PZT sensors are capable of generating their own usable signal in response to applied force, strain, pressure, and acceleration without the application of external energy. Piezoelectric sensors, have higher strain sensitivity than traditional passive sensors including foil strain gages, up to one million times greater, and they can be used in conditions with high noise levels (Gautschi 2002; Sirohi and Chopra 2000; Yu et al. 2011).

Piezoceramics are being used as actuators and active sensors in various inspection applications within civil and aerostructure field including the following projects:

- Ihn et al. (2004) investigated the use of piezoelectric actuators to generate diagnostic signals within an aircraft to detect fatigue crack growth in a repaired structure. The sensor was installed in a composite repair patch bonded to riveted fuselage joints and a cracked metallic plate. The results of this research indicate that the use of piezoelectric actuator/sensor within the repair patch successfully detected fatigue crack growth and the debonding of the patch.

- Lynch (2004) researched the use of active wireless sensors to emit acoustic waves under extreme loading conditions, including seismic loads, to monitor and detect damage in steel moment frames. This monitoring concept was tested using PZT actuation and sensing pads mounted to the surface of an aluminum plate. Of the two PZT pads attached to the aluminum, one was used as an actuator to excite the plate, and the other pad was used as a sensor to detect scatter in the acoustic waves traveling through the plate.
- Zhang (2006) used polymer based piezoelectric paint as a strain sensor to detect surface cracks in structures. Results indicate the successful detection in real-time monitoring of surface fatigue cracks.
- Yu et al. (2011) adapted piezoelectric wafer active sensors (PAWS) to detect AE events during SHM of steel bridges under fatigue loading scenarios. Tests were conducted on steel and aluminum compact tension specimens and results demonstrated that the PAWS measurement and crack mouth opening displacement (CMOD) correlated to the acoustic activities measured using commercially available AE software.

2.4.2 Advantages and Disadvantages

As previously outlined, piezoelectric materials are highly sensitive, comparatively low cost materials that can be used in an array of NDT applications. However, they must be properly monitored and maintained to ensure accuracy. Piezoelectric limitations include temperature, voltage, and mechanical stress effects on the polarization of the ceramic material (Gautschi 2002). Piezoelectric sensing or actuating performance decreases, as the operating temperature increases due to the depolarization of the piezoelectric material. Each piezoceramic material has a maximum temperature exposure limit, or Curie point, where all piezoelectric properties are lost. Continuous operation of a piezoceramic material decreases the maximum temperature limit. An introduction into a strong electric field with opposing polarity will also depolarize piezoceramic materials. Additionally, large mechanical stresses can effectively decrease the polarization of piezoceramic. At elevated temperature levels, the maximum safe stress level and overall performance is decreased and the aging process is accelerated. For more complex detection methods, nontrivial processing and interpretation algorithms are necessary which drives up cost, equipment size, bulk and challenges associated with field applications (CTS 2013; Hellier 2013; Morgan Advanced Materials 2009; Piezo Systems Inc. 2011).

2.5 Summary

Purvis' description of the significance on VI and the essence of fracture mechanics presented by Barsom and Rolfe (1999), identifies the importance of inspection, inspection frequency, inspection method selection, and accurate crack detection in establishing the service life of a structure. Quality inspections and proper crack characterization allow maintenance officials and bridge owners to develop or select an optimal maintenance and monitoring schedule to preserve or extend the life of bridge structure. Each method outlined in this chapter is summarized in Table 2-1.

Table 2-1: Summary of NDE techniques used in the inspection of in-service steel structures (Hellier 2013).

Method	Principles	Application	Advantages	Limitations
Visual Testing (VI)	Uses reflected or transmitted light from test object that is imaged with human eye or other light-sensing device	Many applications in many industries ranging from raw material to finished products and in-service inspection	Can be inexpensive and simple with minimal training required. Broad scope of uses and benefits	Only surface conditions can be evaluated. Effective source of illumination required. Access necessary
Penetrant (PT)	A liquid containing visible or fluorescent dye is applied to surface and enters discontinuities by capillary action	Virtually any solid nonabsorbent material having uncoated surfaces that are not contaminated	Relatively easy and materials are inexpensive. Extremely sensitive, very versatile. Minimal training.	Discontinuities open to the surface only. Surface condition must be relatively smooth and free of contaminants.
Magnetic Particle (MT)	Test part is magnetized an fine ferromagnetic particles applied to surface, aligning at discontinuity	All ferromagnetic materials, for surface and slightly subsurface discontinuities; large and small parts	Relatively easy to use. Equipment/material usually inexpensive. Highly sensitive and fast compared to PT	Only surface and few subsurface discontinuities can be detected. Ferromagnetic materials only.
Radiography (RT)	Radiographic film is exposed when radiation passes through the test object. Discontinuities affect exposure	Most materials, shapes, and structures. Examples include welds, castings, composites, etc., as manufactured or in-service	Provides a permanent record and high sensitivity. Most widely used and accepted volumetric examination.	Limited thickness based on material density. Orientation of planar discontinuities is critical. Radiation hazard.
Ultrasonic (UT)	High-frequency sound pulses from a transducer propagate through the test material, reflecting at interfaces	Most materials can be examined if sound transmission and surface finish are good and shape is not complex.	Provides precise, high-sensitivity results quickly. Thickness information, depth, and type of flaw can be obtained from one side of the component.	No permanent record (usually). Material attenuation, surface finish, and contour Requires couplant.
Eddy Current (EC)	Localized electrical fields are induced into a conductive test specimen by electromagnetic induction	Virtually all conductive materials can be examined for flaws, metallurgical conditions, thinning, and conductivity	Quick, versatile, sensitive; can be non-contacting; easily adaptable to automation and in situ examinations	Variables must be understood and controlled. Shallow depth of penetration, lift-off effects and surface condition.
Acoustic Emission (AE)	As discontinuities propagate, energy is released and travels as stress waves through material. These are detected by means of sensors	Welds, pressure vessels, rotating equipment, some composites and other structures subject to stress or loading.	Large areas can be monitored to detect deteriorating conditions. Can possibly predict failure.	Sensors must contact test surface. Multiple sensors required for flaw location. Signal interpretation required.

CHAPTER 3: PACTS GENERAL DESIGN

The initial PACTS concept design was developed based on the sensing abilities of piezoceramic material, displacement produced by crack opening movement under dynamic loads, and basic strength and material theory. This chapter provides an overview on the basic engineering principles used in the sensing material selection; the substrate geometry and material selection; and the bonding of the sensor and substrate material used in the development of the PACTS tool system. The detailed manufacturing process is outlined in Appendix B and actual dimensions of the PACTS tool tested are provided in Chapter 6.

3.1 Sensing Material Selection

The initial concept of developing a portable crack detection system required an investigation into to the availability of compact, lightweight, and low cost materials that possessed the right material properties to convert crack opening displacements into a detectable signal. Piezoelectric materials were selected for the sensor and PZT was the most readily available material that possessed the sensitivity requirements needed. PZT single layer plate sensors are capable of generating a voltage when subjected to an applied stress in the longitudinal direction.

The design of the PACTS system was developed based on the capabilities of a unimorph system. A unimorph is a cantilever system that is composed of one active sensing or actuation layer bonded to an inactive substrate layer. A deformation applied to the unimorph induces a bending moment in the longitudinal direction of the cantilever. From basic strength-of-material properties, the bending moment causes a compressive displacement in the PZT layer resulting in an electric field (Figure 3-1).

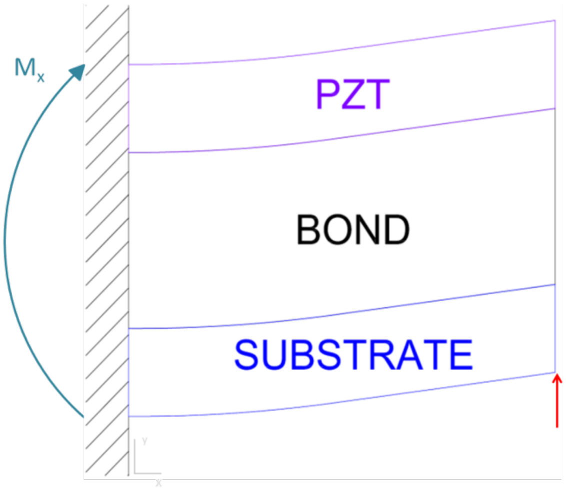

Figure 3-1: Active PZT layered unimorph subjected to a displacement resulting in a moment (M_x) applied in the longitudinal direction.

3.2 Substrate Geometry and Material Selection

Based on the PZT sensing material selection and the unimorph principles, the substrate geometry requirements included the ability to span a surface crack's opening displacement, Δx, and maintain contact with the steel surface during crack opening and closing activities.

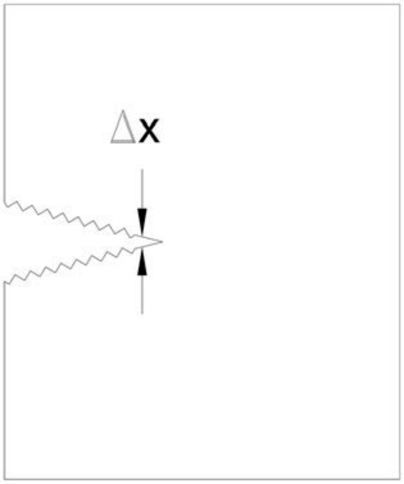

Figure 3-2: Crack opening displacement (Δx) of an edge crack in material.

In order to span the crack opening distance, an H-shaped member was selected. It was determined that weak axis bending of the H-shaped member would be utilized in order to induce a longitudinal moment in the PZT layer (Figure 3-3).

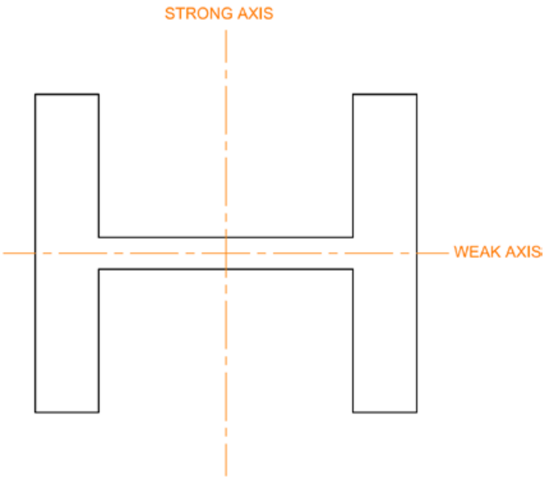

Figure 3-3: Strong and weak axis location for an H-shaped member.

The initial H-beam flange width and web depth selected were 25.4 mm [1.00 in] and 50.8 mm [2.00 in] respectively. Flange thickness was initially designed at 6.35 mm [0.25 in] and the web sections slightly smaller at 5.08 mm [0.20 in]. The overall width of the PACTS system was chosen at 12.70 mm [0.50 in]. The dimensions of the general design are illustrated in Figure 3-4.

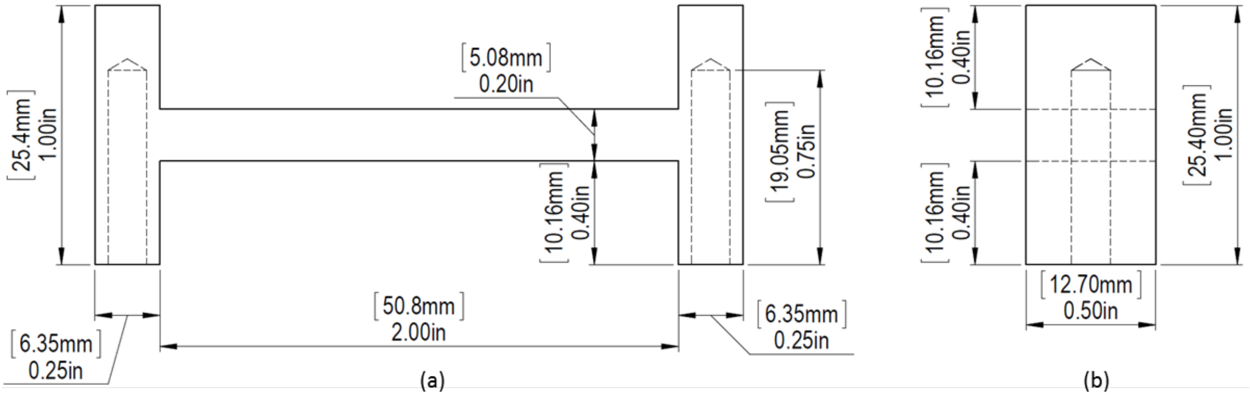

Figure 3-4: PACTS systems general design geometry including (a) profile view and (b) side view of system.

Material selection of the substrate was based on the modulus of elasticity, E, of the PZT. Similar moduli between the material layers would allow for more consistent deformations of the final composite structure. Although, PZT material stiffness varies, a conservative modulus of elasticity value of 62 GPa [9,000 ksi] was used (CTS 2013). Based on the PZT material stiffness, Aluminum 6061 T6 was chosen as the substrate material with a modulus of elasticity, E_s, properties similar to the E_p, at approximately 69 GPa [10,000 ksi] (Boresi and Schmidt 2003).

Since the PACTS system concept would be used for the inspection of in-service structures, it was important to consider the PZT-Aluminum composite's ability to grip and hold the surface under dynamic loading and penetrate unknown paint layer thicknesses. Initially, the concept of mounting carbide scribe tips through the bottom of the H-beam flanges was considered. Although this approach successfully penetrated the paint layer, it was unable to grip the surface of the steel material. Substituting sharpened steel screw shafts for the carbide tips and attaching magnets to the sharpened edge created a structurally sound substrate geometry capable of penetrating steel paint and coating thicknesses while maintaining contact with the cracked steel surface (Figure 3-5).

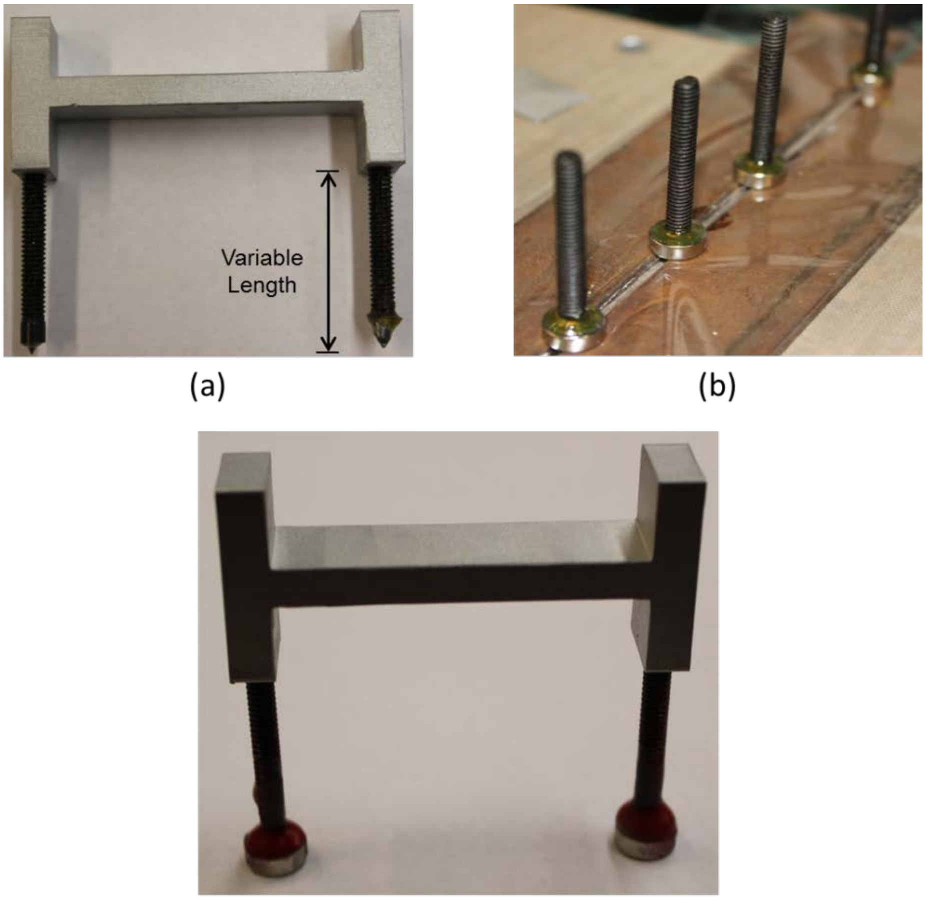

(a) (b)

(c)

Figure 3-5: Substrate geometry design progression including (a) the use of steel screws, (b) attachment of magnets, and (c) the general substrate and leg layout.

The use of the steel screws allowed for added adjustability in varying the distance from the piezoelectric sensing sheet. Since $Moment = Force \times lever\ arm\ distance,$ where the lever arm distance is a function of the screw length, then increasing the length of the screw essentially magnifies the moment produced by the applied displacement. Conversely, a decrease in leg length can decrease the moment in the sensing sheet. Therefore creating an adjustable compact PACTS system that can be used in high and low sensitivity applications.

3.3 Manufacturing

The piezoceramic and substrate layers were bonded together to produce a composite member using the flexible epoxy resin Master Bond EP21TDC. The epoxy was applied in a thin layer and cured at room temperature overnight. Once the epoxy cured, the sensing circuit was constructed. One lead was anchored mechanically and electrically to the ground of the H-frame. The second lead was soldered to the top of the PZT sensor sheet with Tix solder. The two leads were then twinned and routed to the RC charge-sensor circuit and voltmeter. The RC circuit diagram is described and illustrated in Chapter 4. Electrical tape was used to minimize the possibility of disconnecting the contacts from the PZT and the H-frame. Additional wire maintenance was performed and is illustrated in Figure 3-6.

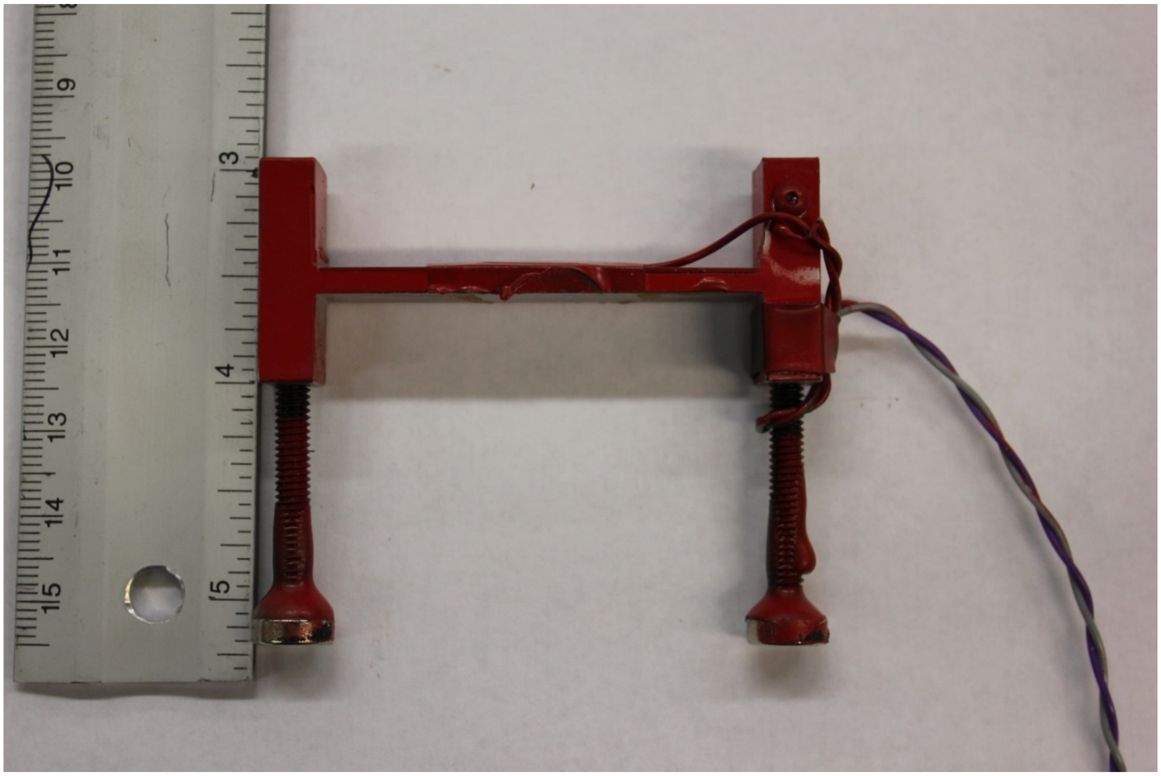

Figure 3-6: Prototype of PACTS tool.

CHAPTER 4: PACTS MODELING

The PACTS tool design is composed of piezoceramic sensing material and a metallic substrate bonded together. It is considered a composite system comprised of multiple lamina, or layers. As a composite thin layer system the mechanical characteristics and behavior can be analyzed using Classic Laminated Plate Theory (CLPT). This chapter illustrates the modeling techniques used to analyze the PACTS system including closed form solution of a sensing plate, and the PACTS tool design in addition to a finite element analysis (FEA) of the PACTS system. An introduction to CLPT for a nonhomogeneous isotropic laminate is followed by the CLPT approach used to analyze the sensing capabilities of an isotropic PACTS system. The last section in this chapter describes the finite element approach used to evaluate the sensitivity of the PACTS system.

4.1 Closed Form Solution of Sensing Plates

4.1.1 Classic Laminate Plate Theory

CLPT uses the stress and deformation principles of mechanics-of-material as a foundation to reduce three-dimensional elastic deformable body problems into two-dimensional problems. Therefore, CLPT can be used to evaluate the behavior of individual lamina, or layers, or various materials. This section will review the mechanics-of-materials properties for individual lamina expressed as the k_{th} lamina of an N-layered laminate. Then, an investigation into the stress and strain variations throughout the thickness of a laminate will be conducted. The laminate forces and moments will be related to the strains and curvature of the laminate. The derivations of isotropic behavior in this section are similar to the orthotropic solutions by Agarwal and

Jones (Agarwal and Bhagwan 2006; Jones 1975). Finally the sensing capabilities of a piezoceramic unimorph sensing plate will be determined based on CLPT derivations.

The relationship between stress and strain for linear elastic materials can be evaluated using the generalized Hooke's Law, where σ_i are the stress components on a three-dimensional cube in the x, y, and z coordinates (or 1, 2, and 3 direction), C_{ij} is the elastic stiffness matrix, and ε_j are the strain components as shown in Equation 4:1.

$$\sigma_i = C_{ij} \cdot \varepsilon_j$$ **Equation 4:1**

For an elastic material the stiffness matrix, C_{ij}, is symmetric and contains 21 independent constants, therefore resulting in the following stress-strain relationship:

$$\overrightarrow{\begin{pmatrix} \sigma_1 \\ \sigma_2 \\ \sigma_3 \\ \tau_{23} \\ \tau_{31} \\ \tau_{12} \end{pmatrix}} = \begin{pmatrix} C_{11} & C_{12} & C_{13} & C_{14} & C_{15} & C_{16} \\ C_{12} & C_{22} & C_{23} & C_{24} & C_{25} & C_{26} \\ C_{13} & C_{23} & C_{33} & C_{34} & C_{35} & C_{36} \\ C_{14} & C_{24} & C_{34} & C_{44} & C_{45} & C_{46} \\ C_{15} & C_{25} & C_{35} & C_{45} & C_{55} & C_{56} \\ C_{16} & C_{26} & C_{36} & C_{46} & C_{56} & C_{66} \end{pmatrix} \cdot \overrightarrow{\begin{pmatrix} \varepsilon_1 \\ \varepsilon_2 \\ \varepsilon_3 \\ \gamma_{23} \\ \gamma_{31} \\ \gamma_{12} \end{pmatrix}}$$ **Equation 4:2**

The sensing plate used in the PACTS tool design is comprised of three lamina including a piezoceramic sheet, a layer of bond material, and the substrate material, aluminum. Each material selected exhibits elastic and isotropic or quasi-isotropic behavior (Barrett 2013; Jones 1975). The following relationships exist between the elastic components of isotropic materials within the elastic stiffness matrix:

$$C_{11} = C_{22} = C_{33} \qquad C_{12} = C_{13} = C_{23} \qquad C_{44} = C_{55} = C_{66}$$

$$C_{66} = \frac{C_{22} - C_{23}}{2} = \frac{C_{11} - C_{12}}{2}$$ **Equation 4:3**

Therefore, the generalized Hooke's Law and the stiffness matrix becomes

$$\overrightarrow{\begin{pmatrix}\sigma_1\\ \sigma_2\\ \sigma_3\\ \tau_{23}\\ \tau_{31}\\ \tau_{12}\end{pmatrix}} = \begin{pmatrix} C_{11} & C_{12} & C_{12} & 0 & 0 & 0\\ C_{12} & C_{11} & C_{12} & 0 & 0 & 0\\ C_{12} & C_{12} & C_{11} & 0 & 0 & 0\\ 0 & 0 & 0 & \frac{C_{11}-C_{12}}{2} & 0 & 0\\ 0 & 0 & 0 & 0 & \frac{C_{11}-C_{12}}{2} & 0\\ 0 & 0 & 0 & 0 & 0 & \frac{C_{11}-C_{12}}{2}\end{pmatrix} \cdot \overrightarrow{\begin{pmatrix}\varepsilon_1\\ \varepsilon_2\\ \varepsilon_3\\ \gamma_{23}\\ \gamma_{31}\\ \gamma12\end{pmatrix}}$$ **Equation 4:4**

In terms of the compliance matrix, *S*, or the inverse of the stress-strain relationship, the strain-stress relation is as follows:

$$\varepsilon_i = S_{ij} \cdot \sigma_j$$ **Equation 4:5**

$$\overrightarrow{\begin{pmatrix}\varepsilon_1\\ \varepsilon_2\\ \varepsilon_3\\ \gamma_{23}\\ \gamma_{31}\\ \gamma_{12}\end{pmatrix}} = \begin{bmatrix} S_{11} & S_{12} & S_{12} & 0 & 0 & 0\\ S_{12} & S_{11} & S_{12} & 0 & 0 & 0\\ S_{12} & S_{12} & S_{11} & 0 & 0 & 0\\ 0 & 0 & 0 & 2\cdot(S_{11}-S_{12}) & 0 & 0\\ 0 & 0 & 0 & 0 & 2(S_{11}-S_{12}) & 0\\ 0 & 0 & 0 & 0 & 0 & 2(S_{11}-S_{12})\end{bmatrix} \cdot \overrightarrow{\begin{pmatrix}\sigma_1\\ \sigma_2\\ \sigma_3\\ \tau_{23}\\ \tau_{31}\\ \tau_{12}\end{pmatrix}}$$ **Equation 4:6**

In accordance with CLPT, the laminate will be loaded under plane-stress conditions within the 1-2 (x-y) plane of the composite. Therefore, all out of plane stresses will be zero and

$$\sigma_3 = \tau_{23} = \tau_{13} = 0$$ **Equation 4:7**

For the plane-stress state, the generalized Hooke's law reduces the stiffness matrix, *C*, and the compliance matrix, *S*, from a 6 x 6 matrix to a 3 x 3 as shown in Figure 4-1 and Figure 4-2.

$$\overrightarrow{\begin{pmatrix} \sigma_1 \\ \sigma_2 \\ \sigma_3 \\ \tau_{23} \\ \tau_{31} \\ \tau_{12} \end{pmatrix}} = \begin{pmatrix} C_{11} & C_{12} & C_{12} & 0 & 0 & 0 \\ C_{12} & C_{11} & C_{12} & 0 & 0 & 0 \\ C_{12} & C_{12} & C_{11} & 0 & 0 & 0 \\ 0 & 0 & 0 & C_{44} & 0 & 0 \\ 0 & 0 & 0 & 0 & C_{55} & 0 \\ 0 & 0 & 0 & 0 & 0 & C_{66} \end{pmatrix} \cdot \overrightarrow{\begin{pmatrix} \varepsilon_1 \\ \varepsilon_2 \\ \varepsilon_3 \\ \gamma_{23} \\ \gamma_{31} \\ \gamma_{12} \end{pmatrix}}$$

Figure 4-1: Reduction of stiffness matrix, *C*, for an isotropic material under plane-stress conditions.

$$\overrightarrow{\begin{pmatrix} \varepsilon_1 \\ \varepsilon_2 \\ \varepsilon_3 \\ \gamma_{23} \\ \gamma_{31} \\ \gamma_{12} \end{pmatrix}} = \begin{pmatrix} S_{11} & S_{12} & S_{12} & 0 & 0 & 0 \\ S_{12} & S_{11} & S_{13} & 0 & 0 & 0 \\ S_{12} & S_{12} & S_{11} & 0 & 0 & 0 \\ 0 & 0 & 0 & S_{44} & 0 & 0 \\ 0 & 0 & 0 & 0 & S_{55} & 0 \\ 0 & 0 & 0 & 0 & 0 & S_{66} \end{pmatrix} \cdot \overrightarrow{\begin{pmatrix} \sigma_1 \\ \sigma_2 \\ \sigma_3 \\ \tau_{23} \\ \tau_{31} \\ \tau_{12} \end{pmatrix}}$$

Figure 4-2: Reduction of compliance matrix, S, for an isotropic material under plane-stress conditions.

The strain-stress relations for an isotropic material under plane stress conditions using the reduced compliance matrix, *S*, is as follows:

$$\overrightarrow{\begin{pmatrix} \varepsilon_1 \\ \varepsilon_2 \\ \gamma_{12} \end{pmatrix}} = \begin{pmatrix} S_{11} & S_{12} & 0 \\ S_{12} & S_{11} & 0 \\ 0 & 0 & S_{66} \end{pmatrix} \cdot \overrightarrow{\begin{pmatrix} \sigma_1 \\ \sigma_2 \\ \tau_{12} \end{pmatrix}} \qquad \textbf{Equation 4:8}$$

The compliance matrix, *S*, can be described in terms of three engineering constants including the modulus of elasticity, E_i, shear modulus or rigidity, G_i, and Poisson's ratio, ν_{ij}, where

$$S_{11} = \frac{1}{E} \qquad S_{12} = \frac{-\nu}{E} \qquad S_{66} = \frac{1}{G}$$

Equation 4:9

The stress-strain relations for an isotropic material under plane stress conditions and using a reduced stiffness matrix, *Q*, is as follows:

$$\overrightarrow{\begin{pmatrix} \sigma_1 \\ \sigma_2 \\ \tau_{12} \end{pmatrix}} = \begin{pmatrix} Q_{11} & Q_{12} & 0 \\ Q_{12} & Q_{11} & 0 \\ 0 & 0 & Q_{66} \end{pmatrix} \cdot \overrightarrow{\begin{pmatrix} \varepsilon_1 \\ \varepsilon_2 \\ \gamma_{12} \end{pmatrix}}$$

Equation 4:10

where,

$$Q_{11} = \frac{S_{22}}{S_{11} \cdot S_{22} - S_{12}^2} = \frac{E}{1 - \nu^2}$$

$$Q_{12} = \frac{-S_{12}}{S_{11} \cdot S_{22} - S_{12}^2} = \frac{\nu \cdot E}{1 - \nu^2}$$

Equation 4:11

$$Q_{66} = \frac{1}{S_{66}} = G$$

4.1.1.1 Laminate Strain and Stress Variation

The resultant force and moment can be determined using classic laminated plate theory by integrating the stress-strain relations for each layer of the laminate thickness subjected to strain variations. In accordance with CLPT theory, it is assumed that the unimorph piezoceramic laminate acts as a single layer material with no slippage across the lamina boundaries. Therefore the variation in stresses across the thickness of the laminate can be evaluated. Using CLPT, the mid-plane strain $(\varepsilon_1^0, \varepsilon_2^0, \gamma_{12}^0)$, plate curvature $(\kappa_1, \kappa_2, \kappa_{12})$, and the distance from mid-plane of the laminate, z, can be used to determine strain at any point in a laminate using Equation 4:12.

$$\overrightarrow{\begin{pmatrix} \varepsilon_1 \\ \varepsilon_2 \\ \gamma_{12} \end{pmatrix}} = \overrightarrow{\begin{pmatrix} \varepsilon_1^{\;0} \\ \varepsilon_2^{\;0} \\ \gamma_{12}^{\;0} \end{pmatrix}} + z\cdot \overrightarrow{\begin{pmatrix} \kappa_1 \\ \kappa_2 \\ \kappa_{12} \end{pmatrix}}$$

Equation 4:12

Substitution of the through thickness strain variations (Equation 4:12) into Equation 4:10 yields the stresses in a specified layer in terms of the laminate middle-surface strains and curvatures as

$$\overrightarrow{\begin{pmatrix} \sigma_1 \\ \sigma_2 \\ \tau_{12} \end{pmatrix}} = \begin{pmatrix} Q_{11} & Q_{12} & 0 \\ Q_{12} & Q_{22} & 0 \\ 0 & 0 & Q_{66} \end{pmatrix}_k \cdot \overrightarrow{\left[\begin{pmatrix} \varepsilon_1^{\;0} \\ \varepsilon_2^{\;0} \\ \gamma_{12}^{\;0} \end{pmatrix} + z \begin{pmatrix} \kappa_1 \\ \kappa_2 \\ \kappa_{12} \end{pmatrix}\right]}$$

Equation 4:13

4.1.1.2 Laminate Forces and Moments

Resultant in-plane forces and moments (Figure 4-3) of a basic laminate geometry of an N-Layered Laminate (Figure 4-4) can be determined using the stress and strain variations presented in the section 4.1.1.1. Resultant forces N_{ij}, are per unit width of the laminate cross section. Similarly, the resultant moments, M_{ij}, are per unit width of the laminate.

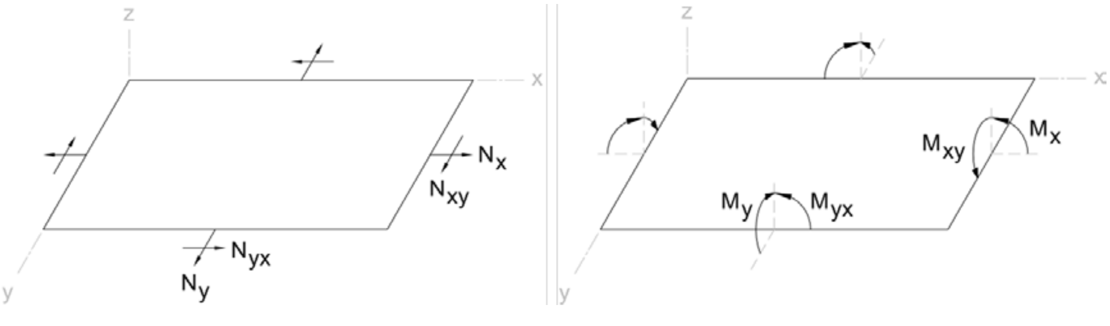

Figure 4-3: In-Plane Forces, N, and Moments, M, on a flat surface.

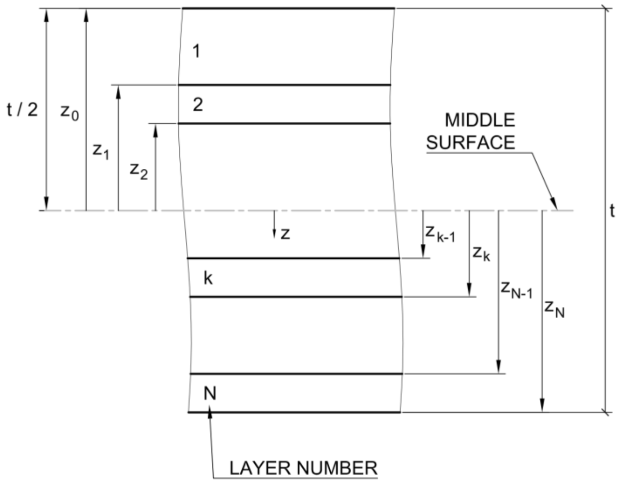

Figure 4-4: Geometry of N-Layered Laminate (Jones 1975).

Since stresses within the laminate vary from lamina to lamina, the resultant forces and moments acting on the laminate are determined by integration of the corresponding stress through the laminate thickness. Equation 4:14 displays the resultant force in units of force per unit length for the kth lamina of the general N-layered laminate (Figure 4-4).

$$\overrightarrow{\begin{pmatrix} N_{11} \\ N_{22} \\ N_{12} \end{pmatrix}} = \int_{\frac{-t}{2}}^{\frac{t}{2}} \overrightarrow{\begin{pmatrix} \sigma_1 \\ \sigma_2 \\ \tau_{12} \end{pmatrix}} \, dz = \sum_{k=1}^{N} \int_{z_{k-1}}^{z_k} \overrightarrow{\begin{pmatrix} \sigma_1 \\ \sigma_2 \\ \tau_{12} \end{pmatrix}_k} \, dz \qquad \textbf{Equation 4:14}$$

Rearranging Equation 4:14 and substituting in Equation 4:13, the laminate forces become

$$\overrightarrow{\begin{pmatrix} N_{11} \\ N_{22} \\ N_{12} \end{pmatrix}} = \sum_{k=1}^{N} \begin{pmatrix} Q_{11} & Q_{12} & 0 \\ Q_{12} & Q_{22} & 0 \\ 0 & 0 & Q_{66} \end{pmatrix}_k \cdot \left[\int_{z_{k-1}}^{z_k} \overrightarrow{\begin{pmatrix} {\varepsilon_1}^0 \\ {\varepsilon_2}^0 \\ {\gamma_{12}}^0 \end{pmatrix}} \, dz + \int_{z_{k-1}}^{z_k} \overrightarrow{\begin{pmatrix} \kappa_1 \\ \kappa_2 \\ \kappa_{12} \end{pmatrix}} \cdot z \, dz \right] \qquad \textbf{Equation 4:15}$$

Equation 4:16 displays the resultant moment in units of moment per length. Moment is calculated by integrating the through thickness of the corresponding stress times the moment arm with respect to the mid-plane of the laminate.

$$\overrightarrow{\begin{pmatrix} M_{11} \\ M_{22} \\ M_{12} \end{pmatrix}} = \int_{\frac{-t}{2}}^{\frac{t}{2}} \overrightarrow{\begin{pmatrix} \sigma_1 \\ \sigma_2 \\ \tau_{12} \end{pmatrix}} \cdot z \, dz = \sum_{k=1}^{N} \int_{z_{k-1}}^{z_k} \overrightarrow{\begin{pmatrix} \sigma_1 \\ \sigma_2 \\ \tau_{12} \end{pmatrix}_k} \cdot z \, dz$$

Equation 4:16

Rearranging Equation 4:16 and substituting in Equation 4:13, the laminate moments becomes

$$\overrightarrow{\begin{pmatrix} M_{11} \\ M_{22} \\ M_{12} \end{pmatrix}} = \sum_{k=1}^{N} \begin{pmatrix} Q_{11} & Q_{12} & 0 \\ Q_{12} & Q_{22} & 0 \\ 0 & 0 & Q_{66} \end{pmatrix}_k \cdot \left[\int_{z_{k-1}}^{z_k} \overrightarrow{\begin{pmatrix} \varepsilon_1^{\,0} \\ \varepsilon_2^{\,0} \\ \gamma_{12}^{\,0} \end{pmatrix}} \cdot z \, dz + \int_{z_{k-1}}^{z_k} \overrightarrow{\begin{pmatrix} \kappa_1 \\ \kappa_2 \\ \kappa_{12} \end{pmatrix}} \cdot z^2 \, dz \right]$$

Equation 4:17

Since $\varepsilon_1^0, \varepsilon_2^0, \gamma_{12}^0$, and plate curvature are functions of the mid-plane and not of the plate thickness, z, equations of force and moment per unit length can be rewritten in a simplified form as

$$\overrightarrow{\begin{pmatrix} N_{11} \\ N_{22} \\ N_{12} \end{pmatrix}} = \begin{pmatrix} A_{11} & A_{12} & A_{16} \\ A_{12} & A_{22} & A_{26} \\ A_{16} & A_{26} & A_{66} \end{pmatrix} \cdot \overrightarrow{\begin{pmatrix} \varepsilon_1^{\,0} \\ \varepsilon_2^{\,0} \\ \gamma_{12}^{\,0} \end{pmatrix}} + \begin{pmatrix} B_{11} & B_{12} & B_{16} \\ B_{12} & B_{22} & B_{26} \\ B_{16} & B_{26} & B_{66} \end{pmatrix} \cdot \overrightarrow{\begin{pmatrix} \kappa_1 \\ \kappa_2 \\ \kappa_{12} \end{pmatrix}}$$

Equation 4:18

and

$$\overrightarrow{\begin{pmatrix} M_{11} \\ M_{22} \\ M_{12} \end{pmatrix}} = \begin{pmatrix} B_{11} & B_{12} & B_{16} \\ B_{12} & B_{22} & B_{26} \\ B_{16} & B_{26} & B_{66} \end{pmatrix} \cdot \overrightarrow{\begin{pmatrix} \varepsilon_1{}^0 \\ \varepsilon_2{}^0 \\ \gamma_{12}{}^0 \end{pmatrix}} + \begin{pmatrix} D_{11} & D_{12} & D_{16} \\ D_{12} & D_{22} & D_{26} \\ D_{16} & D_{26} & D_{66} \end{pmatrix} \cdot \overrightarrow{\begin{pmatrix} \kappa_1 \\ \kappa_2 \\ \kappa_{12} \end{pmatrix}}$$

Equation 4:19

where,

$$A_{ij} = \sum_{k=1}^{N} \left[\left(\overline{Q_{ij}} \right)_k \left(z_k - z_{k-1} \right) \right]$$

$$B_{ij} = \frac{1}{2} \left[\sum_{k=1}^{N} \left[\left(\overline{Q_{ij}} \right)_k \left[z_k{}^2 - \left(z_{k-1} \right)^2 \right] \right] \right]$$

$$D_{ij} = \frac{1}{3} \left[\sum_{k=1}^{N} \left[\left(\overline{Q_{ij}} \right)_k \left[z_k{}^3 - \left(z_{k-1} \right)^3 \right] \right] \right]$$

Equation 4:20

The constitutive equation for the thin laminated plate includes Matrix A, the extensional stiffness matrix which relates the resultant force per unit length to the mid-plane strains. Matrix B is the coupling stiffness matrix that represents coupling behavior between bending and the extension of the laminate. Matrix D is the bending stiffness matrix that relates the resultant moment per length to the mid-plane plate curvatures of the laminate. The compact notation of the total plate equation is presented in Equation 4:21.

$$\overrightarrow{\begin{pmatrix} N \\ M \end{pmatrix}} = \begin{pmatrix} A & B \\ B & D \end{pmatrix}_L \cdot \overrightarrow{\begin{pmatrix} \varepsilon^0 \\ \kappa \end{pmatrix}}$$

Equation 4:21

4.1.1.3 Sensing Plate Systems

The unimorph laminate composed of piezoelectric material bonded to a structural substrate subjected to bending is illustrated in Figure 4-5. The resulting strain in the unimorph due to bending results in a charge change within the piezoceramic layer. The charge generated in the piezoceramic layer is proportional to the strain (and strain times rate of change) within the PZT layer.

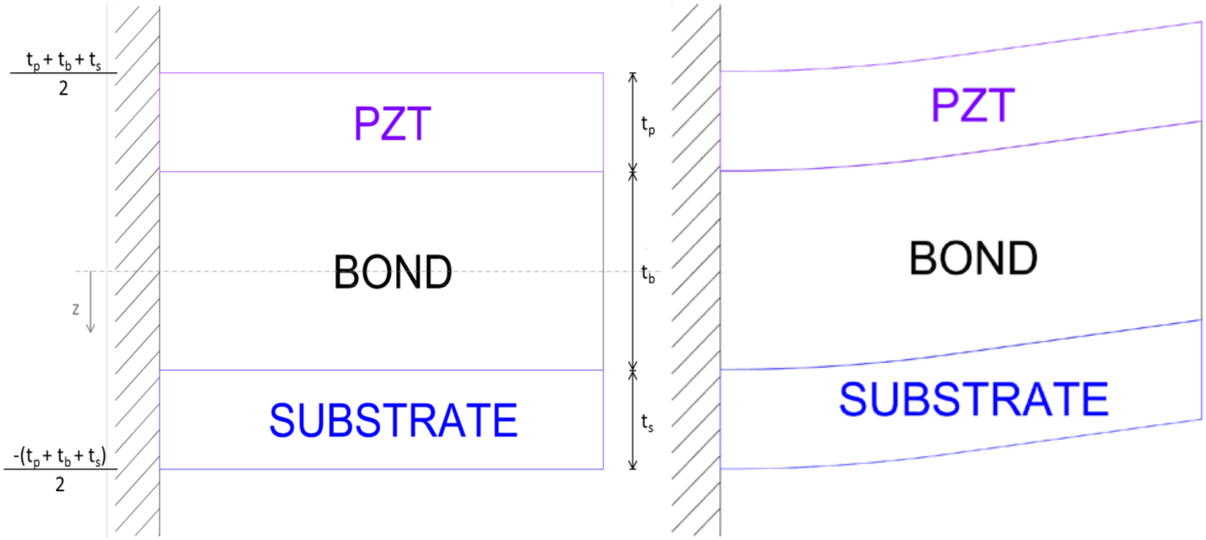

Figure 4-5: Piezoelectric unimorph sensor.

Due to the bending action of the unimorph illustrated in Figure 4-5, the torsionally induced shear and twist are negligible therefore reducing the total plate equation (Equation 4:21) from a 6 x 6 to a 4 x 4 matrix as follows:

$$\begin{pmatrix} A_{11} & A_{12} & B_{11} & B_{12} \\ A_{12} & A_{22} & B_{12} & B_{22} \\ B_{11} & B_{12} & D_{11} & D_{12} \\ B_{12} & B_{22} & D_{12} & D_{22} \end{pmatrix}_L \cdot \overrightarrow{\begin{pmatrix} \varepsilon_{11} \\ \varepsilon_{22} \\ \kappa_{11} \\ \kappa_{22} \end{pmatrix}} = \overrightarrow{\begin{pmatrix} N_{11} \\ N_{22} \\ M_{11} \\ M_{22} \end{pmatrix}}$$

Equation 4:22

Where the laminate ABBD matrix is the summation of the ABBD matrix for each lamina’s ABBD

$$\begin{pmatrix} A & B \\ B & D \end{pmatrix}_L = \begin{pmatrix} A & B \\ B & D \end{pmatrix}_p + \begin{pmatrix} A & B \\ B & D \end{pmatrix}_b + \begin{pmatrix} A & B \\ B & D \end{pmatrix}_s$$

4.2 Closed Form Solution of the PACTS Tool

As described in Chapter 3, the PACTS tool is composed of a piezoceramic layer bonded to the web of an H-shaped aluminum beam. The analysis of the PACTS tool was conducted based on the CLPT and sensor analysis that was derived in Chapter 4. In addition to the engineering constants including the modulus of elasticity, E_i, shear modulus or rigidity, G_i, and Poisson's ratio, ν_{ij}, used in CLPT, additional geometric variables were investigated in analyzing the sensitivity of the PACTS tool (Figure 4-6). The sensing capabilities of the PACTS system were analyzed by investigating the strain within the PZT layer, where the voltage sensed, $V_{sensing}$, resulting from the strain and displacement of the composite is proportional to the strain in the longitudinal direction of the piezoelectric layer, ε_{11}, and the thickness of the piezoceramic layer, t_p. Thus:

$$V_{sensing} \propto \varepsilon_p \times t_p$$ **Equation 4:23**

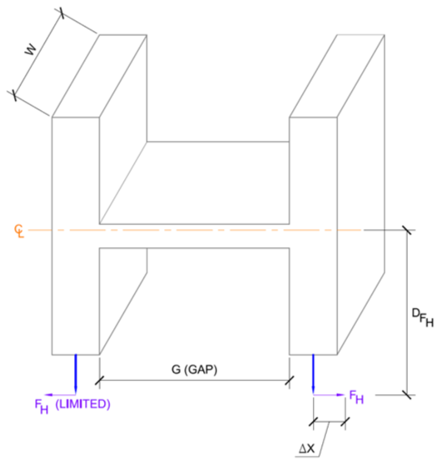

where,

D_{FH} – Distance from the tool center line to the contact surface

F_H – The frictional force at the contact surface, limited by magnet strength

G – Length of the web of the PACTS tool

W – The width of the PACTS tool

ΔX – Distance the "leg" is displaced during testing

Figure 4-6: PACTS tool diagram and variables used in CLPT analysis

The laminate force and moment based on CLPT is similar to those outlined in Equation 4:22; however, due to the shape of the PACTS tool and the large constraint at the tool flanges, the beam or piezoceramic layer only bends in the longitudinal direction, x. This bending action along the x-direction allows for the approximation that the force and moment in the y-direction equal zero ($N_{22} = 0 \; and \; M_{22} = 0$). These boundary conditions reduce the stress-strain relationship in Equation 4:22 to a 2 x 2 stiffness matrix as follows:

$$\begin{pmatrix} A_{11} & B_{11} \\ B_{11} & D_{11} \end{pmatrix}_L \cdot \overrightarrow{\begin{pmatrix} \varepsilon_{11} \\ k_{11} \end{pmatrix}} = \overrightarrow{\begin{pmatrix} N_{11} \\ M_{11} \end{pmatrix}}$$

Equation 4:24

Based on the geometry of the PACTS tool, the normal force per unit length, *N₁₁*, can be represented as a function of the horizontal force, *F_H*, induced by the crack mouth opening of the material per unit width, *W*, of the tool. Similarly, the moment per unit length, *M₁₁*, can be represented as the normal force per unit length multiplied by the moment arm. The moment arm of the PACTS tool is the distance from the center line of the tool to the contact surface of the material being detected or D_{FH}. Therefore the force and moment can be represented as follows:

$$\overrightarrow{\begin{pmatrix} N_{11} \\ M_{11} \end{pmatrix}} = \overrightarrow{\begin{pmatrix} \dfrac{F_H}{W} \\ \dfrac{F_H \cdot D_{FH}}{W} \end{pmatrix}}$$

Equation 4:25

Substitution of Equation 4:25 into Equation 4:24, yields

$$\begin{pmatrix} A_{11} & B_{11} \\ B_{11} & D_{11} \end{pmatrix}_L \cdot \overrightarrow{\begin{pmatrix} \varepsilon_{11} \\ k_{11} \end{pmatrix}} = \begin{pmatrix} \dfrac{F_H}{W} \\ \dfrac{F_H \cdot D_{FH}}{W} \end{pmatrix}$$

Equation 4:26

Solving Equation 4:26 for the strain, ε_{11}, curvature, κ_{11}, yields

$$\overrightarrow{\begin{pmatrix} \varepsilon_{11} \\ k_{11} \end{pmatrix}} = \frac{1}{A_{11} \cdot D_{11} - B_{11}^{2}} \cdot \begin{pmatrix} D_{11} & -B_{11} \\ -B_{11} & A11 \end{pmatrix} \cdot \overrightarrow{\begin{pmatrix} \dfrac{F_H}{W} \\ \dfrac{F_H \cdot D_{FH}}{W} \end{pmatrix}}$$ **Equation 4:27**

$$\overrightarrow{\varepsilon_{11}} = \frac{\left(D_{11} - B_{11} \cdot D_{FH}\right) \cdot \left(\dfrac{F_H}{W}\right)}{A_{11} \cdot D_{11} - B_{11}^{2}}$$ **Equation 4:28**

$$\overrightarrow{k_{11}} = \frac{\left(A_{11} \cdot D_{FH} - B_{11}\right) \cdot \left(\dfrac{F_H}{W}\right)}{A_{11} \cdot D_{11} - B_{11}^{2}}$$ **Equation 4:29**

The ABBD laminate and lamina matrices are functions of the piezoceramic thickness, t_p, the bond thickness, t_b, and the substrate (Aluminum) thickness, t_s. Using CLPT to evaluate through the thickness of the laminate illustrated in Figure 4-7, the laminate matrices A_{11}, B_{11}, and D_{11} can be calculated using the summation of the PZT, bond, and substrate lamina matrices.

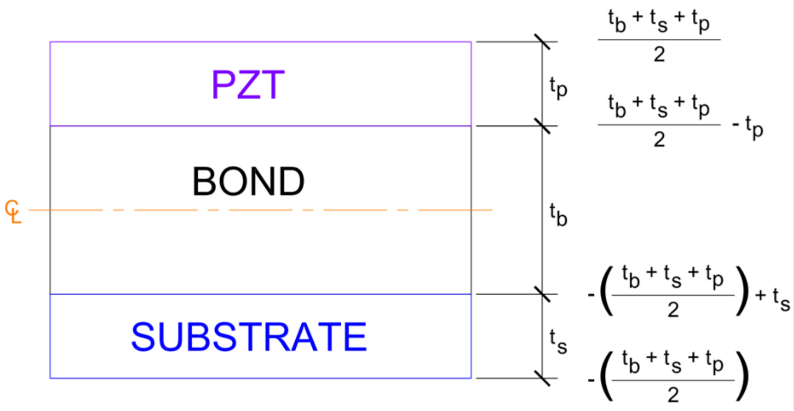

where,

t_b – bond layer thickness

t_p – piezoceramic layer thickness

t_s – substrate (Aluminum) layer thickness

Figure 4-7: Laminate geometry with evaluation thicknesses of piezoceramic, bond, and substrate layers.

$$\begin{pmatrix} A & B \\ B & D \end{pmatrix}_L = \begin{pmatrix} A & B \\ B & D \end{pmatrix}_p + \begin{pmatrix} A & B \\ B & D \end{pmatrix}_b + \begin{pmatrix} A & B \\ B & D \end{pmatrix}_s$$ **Equation 4:30**

$$A_{11} = A_{11p} + A_{11b} + A_{11s}$$

$$\Longrightarrow \quad A_{11p} = E_p \cdot \int_{\frac{t_b+t_s-t_p}{2}}^{\frac{t_b+t_s+t_p}{2}} 1 \, dz \quad \Big| \quad A_{11b} = E_b \cdot \int_{-\frac{t_b+t_s+t_p}{2}+t_s}^{\frac{t_b+t_s-t_p}{2}} 1 \, dz \quad \Big| \quad A_{11s} = E_s \cdot \int_{-\frac{t_b+t_s+t_p}{2}}^{-\frac{t_b+t_s+t_p}{2}+t_s} 1 \, dz$$

$$B_{11} = B_{11p} + B_{11b} + B_{11s}$$

$$\Longrightarrow \quad B_{11p} = E_p \cdot \int_{\frac{t_b+t_s-t_p}{2}}^{\frac{t_b+t_s+t_p}{2}} z \, dz \quad \Big| \quad B_{11b} = E_b \cdot \int_{-\frac{t_b+t_s+t_p}{2}+t_s}^{\frac{t_b+t_s-t_p}{2}} z \, dz \quad \Big| \quad B_{11s} = E_s \cdot \int_{-\frac{t_b+t_s+t_p}{2}}^{-\frac{t_b+t_s+t_p}{2}+t_s} z \, dz$$

$$D_{11} = D_{11p} + D_{11b} + D_{11s}$$

$$\Longrightarrow \quad D_{11p} = E_p \cdot \int_{\frac{t_b+t_s-t_p}{2}}^{\frac{t_b+t_s+t_p}{2}} z^2 \, dz \quad \Big| \quad D_{11b} = E_b \cdot \int_{-\frac{t_b+t_s+t_p}{2}+t_s}^{\frac{t_b+t_s-t_p}{2}} z^2 \, dz \quad \Big| \quad D_{11s} = E_s \cdot \int_{-\frac{t_b+t_s+t_p}{2}}^{-\frac{t_b+t_s+t_p}{2}+t_s} z^2 \, dz$$

where,

E_p = PZT Modulus Elasticity

E_b = Bond Material Modulus of Elasticity

E_s = Substrate (Aluminum) Modulus of Elasticity

Solving Equation 4:27 for the strain in the PZT layer, ε_p, yields

$$\varepsilon_p = \varepsilon_{11} \pm \left(\frac{t_b + t_s}{2}\right) \kappa_{11} \qquad \textbf{Equation 4:31}$$

The sensitivity of the PACTS tool as a function of the PZT thickness and longitudinal strain can be found by substituting Equation 4:31 into the sensitivity equation (Equation 4:23).

$$V_{piezo} \propto \left[\varepsilon_{11} \pm \left(\frac{t_b + t_s}{2} \right) \text{ƙ}_{11} \right] \cdot g_{31} t_p$$ **Equation 4:32**

$$V_{sensed} \propto f \cdot R \left[\varepsilon_{11} \pm \left(\frac{t_b + t_s}{2} \right) \text{ƙ}_{11} \right] \cdot \frac{g_{31} t_p}{C_{q-store}}$$ **Equation 4:33**

Where

g_{31} – the strain developed per applied charge density, where the stress is applied in the X-direction (axis 1) and the electrodes are applied perpendicular to the Z-axis (axis 3)

$C_{q\text{-}store}$ – the stored charge in the capacitor within the circuit (including total circuit capacitance)

R – Resistance

f – Frequency of excitation

4.2.1 Generalized Solution

So as to give the reader a fundamental feel for the most important driving parameters and relationships, the PACTS system can be greatly simplified:

Since the bond layer stiffness is significantly less than the PZT and substrate, the PACTS system sensitivity is governed by the PZT and substrate layers. Therefore sensitivity equations can be determined using a two layer laminate (Figure 4-8).

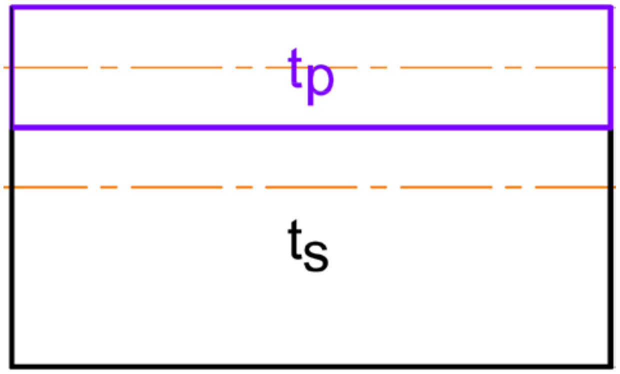

Figure 4-8: Two layer laminate of the driving parameters of the PACTS tool.

Remembering Hooke's Law where the resultant forces, where

$$F = k\cdot\Delta x$$ **Equation 4:34**

or

$$\overrightarrow{\begin{pmatrix} N \\ M \end{pmatrix}} = \begin{pmatrix} A & B \\ B & D \end{pmatrix}\cdot\overrightarrow{\begin{pmatrix} \varepsilon^{0} \\ \kappa \end{pmatrix}}$$ **Equation 4:35**

Considering shear and twist terms trend towards zero and expanding Equation 4:35 yields the following:

$$\overrightarrow{\begin{pmatrix} N_{11} \\ N_{22} \\ M_{11} \\ M_{22} \end{pmatrix}} = \begin{pmatrix} A_{11} & A_{12} & B_{11} & B_{12} \\ A_{12} & A_{22} & B_{12} & B_{22} \\ B_{11} & B_{12} & D_{11} & D_{12} \\ B_{12} & B_{22} & D_{12} & D_{22} \end{pmatrix}\cdot\overrightarrow{\begin{pmatrix} \varepsilon_{11}^{0} \\ \varepsilon_{22}^{0} \\ k_{11} \\ k_{22} \end{pmatrix}}$$ **Equation 4:36**

Assuming isotropic behavior of the laminate, then

$$A_{11} \equiv A_{22} \qquad B_{11} \equiv B_{22} \qquad D_{11} \equiv D_{22}$$

and

$$\overrightarrow{\begin{pmatrix} N_{11} \\ N_{22} \\ M_{11} \\ M_{22} \end{pmatrix}} = \begin{pmatrix} A_{11} & A_{12} & B_{11} & B_{12} \\ A_{12} & A_{11} & B_{12} & B_{11} \\ B_{11} & B_{12} & D_{11} & D_{12} \\ B_{12} & B_{11} & D_{12} & D_{11} \end{pmatrix} \cdot \overrightarrow{\begin{pmatrix} {\varepsilon_{11}}^{0} \\ {\varepsilon_{22}}^{0} \\ k_{11} \\ k_{22} \end{pmatrix}}$$

Equation 4:37

Assuming the mid-plane strain in the PZT, ε_{piezo}, is dominated by moments, then

$$\varepsilon_{11}^{0} \cong \varepsilon_{22}^{0} \cong 0$$

Assuming the H-frame generates enough lateral stiffness where

$$\varepsilon_{22}^{0} \cong 0$$

then Equation 4:37 reduces to a scalar, where

$$\overrightarrow{\left(M_{11}\right)} = \left(D_{11}\right) \cdot \overrightarrow{\left(\kappa_{11}\right)}$$

Equation 4:38

$$M_{11} = D_{11} \cdot \kappa_{11}$$

Solving for curvature, $ƙ_{11}$

Equation 4:39

$$\kappa_{11} = \frac{M_{11}}{D_{11}}$$

From Equation 4:25, the moment per unit width of the PACTS tool, M_{11} can be substituted into Equation 4:39, then curvature, κ_{11}, can be expressed in terms of F_H, D_{FH}, and W as follows:

$$\kappa_{11} = \frac{F_H \cdot D_{FH}}{W \cdot D_{11}}$$

Equation 4:40

As previously stated, the mid-plane strain of the laminate is approximately zero therefore, translating the curvature, $ƙ_{11}$, solution into the mid-plane strain in the PZT,

ε_{piezo}, can be done using small angle theory and evaluating the thickness illustrated in Figure 4-9.

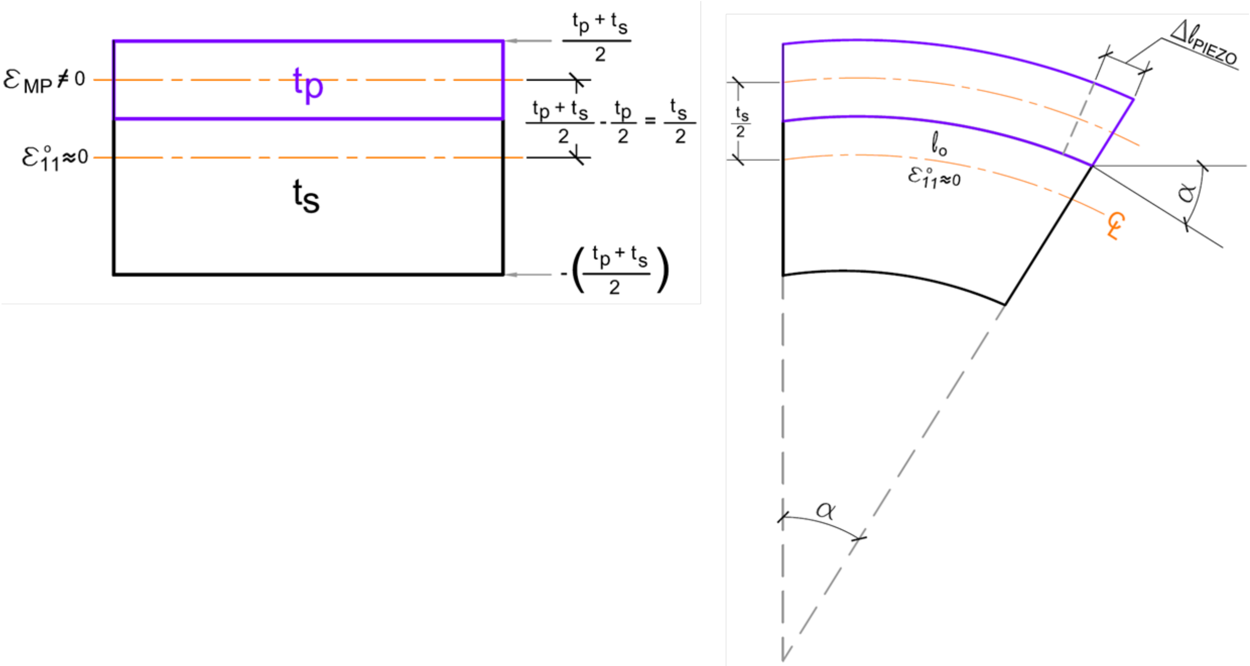

Figure 4-9: PZT and substrate dominated laminate.

Where,

$$\alpha = \kappa\left(\frac{\text{degrees}}{\text{in}}\right)\cdot l_o(\text{in}) \qquad \textbf{Equation 4:41}$$

And

$$\varepsilon_{piezo} = \frac{t_s/2}{l_o}\cdot\alpha \qquad \textbf{Equation 4:42}$$

Substitution of Equation 4:41 into Equation 4:42, assuming that the stiffness of the piezoceramic is roughly equal to that of the substrate, the following expression holds true:

$$\varepsilon_{piezo} \sim \frac{t_s}{2}\cdot \kappa_{11} \qquad \textbf{Equation 4:43}$$

If

$$V_{piezo} \propto \varepsilon_{piezo} \cdot g_{31} \cdot t_p \qquad \textbf{Equation 4:44}$$

Then substituting Equation 4:43 into Equation 4:44 yields

$$V_{piezo} \propto \frac{t_s}{2} \cdot \kappa_{11} \cdot g_{31} \cdot t_p \qquad \textbf{Equation 4:45}$$

The resulting voltage in the PZT layer can be expressed in terms of the PACTS geometry, by substituting the curvature, κ_{11}, expression (Equation 4:40) into Equation 4:45. Therefore,

$$V_{piezo} \propto \frac{t_s \cdot t_p}{2} \cdot g_{31} \cdot \left[\frac{F_H \cdot D_{FH}}{D_{11} \cdot W}\right] \qquad \textbf{Equation 4:46}$$

The circuit designed in order to document the sensed voltage of the PACTS systems is illustrated in Figure 4-10. The circuit is directly connected to the PZT layer of the PACTS tool, and includes a resistor and capacitor.

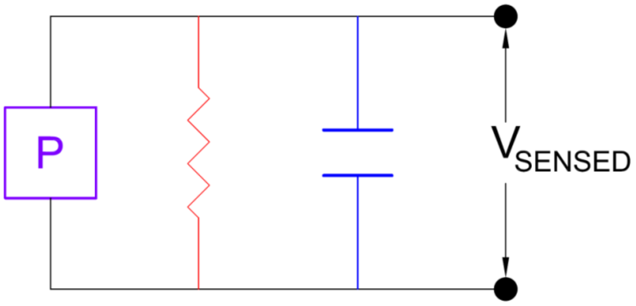

Figure 4-10: PACTS tool test RC charging circuit diagram.

Therefore the voltage read from the multimeter, or V_{sensed}, can be evaluated using, the voltage in the PZT, V_{piezo}, the frequency, f, and time as shown in Equation 4:47.

$$V_{sensed} \propto \frac{t_s \cdot t_p \cdot g_{31} \cdot \left[\frac{F_H \cdot D_{FH}}{D_{11} \cdot W}\right] \cdot f * time}{C_{q-stored}}$$ **Equation 4:47**

Initially, as time, t, increases the voltage sensed increases linearly. However, eventually, the voltage level will reach a point where the shunting resistor allows enough current to leak through it and the voltage sensed trends towards an asymptotic value as shown in Figure 4-11. This research limited its application to the linear range, therefore, non-linear sensing is outside of the scope of this dissertation.

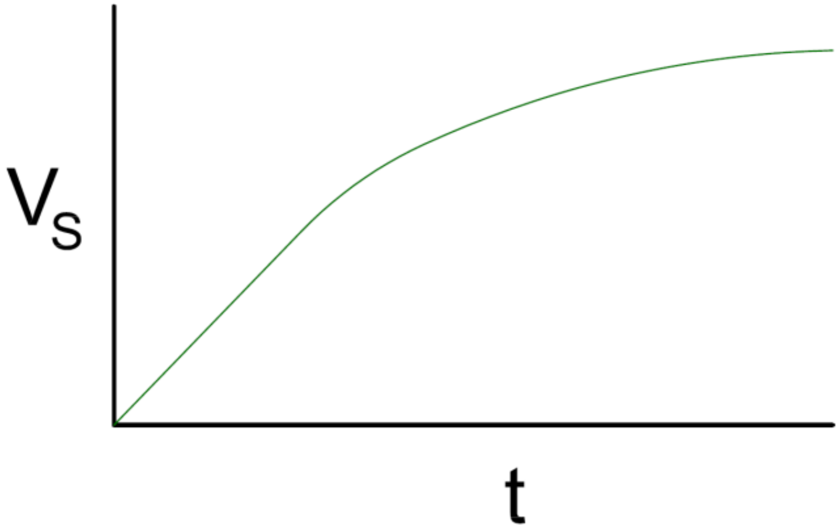

Figure 4-11: General relationship of sensed Voltage, V_s and time, t of RC charging circuit.

4.3 Finite Element Analysis

A detailed analytical investigation was conducted on the basic H-shape design of the PACTS system using finite element (FE) modeling software ABAQUS 6.12-3. The two-dimension linear elastic model was composed of three main parts: H-beam, bond layer, and PZT layer. Due to the doubly symmetric nature of H-section members, only half of the sensor shape (Figure 4-12) was modeled therefore simplifying the size of the finite element model and reducing analysis time requirements of the program. The modeled parts were connected using surface-to-surface tie constraints and each part of the model had independent material properties. The Young's moduli were taken as 69 GPa [10,000 ksi], 62 GPa [9,000 ksi], and 1.97 GPa [286 ksi] for aluminum substrate, PZT, and bond material, respectively. The material properties used for the FE model and Closed Form Solution are located in Appendix A.

Figure 4-12: FE model of PACTS tool layout with applied unit force

The model was developed to determine the maximum longitudinal strain, ε_{11}, in the mid-plane of the PZT layer. In accordance with the sensing capabilities of the PZT materials, the voltage sensed by a piezoceramic sensor is proportional to the mid-plane strain of the PZT layer times the PZT layer thickness, t_p. In order to generalize the model, a unit force was applied to the flange (Figure 4-12) of the H-beam causing the composite web to bend and subject the PZT to compressive forces (Figure 4-13).

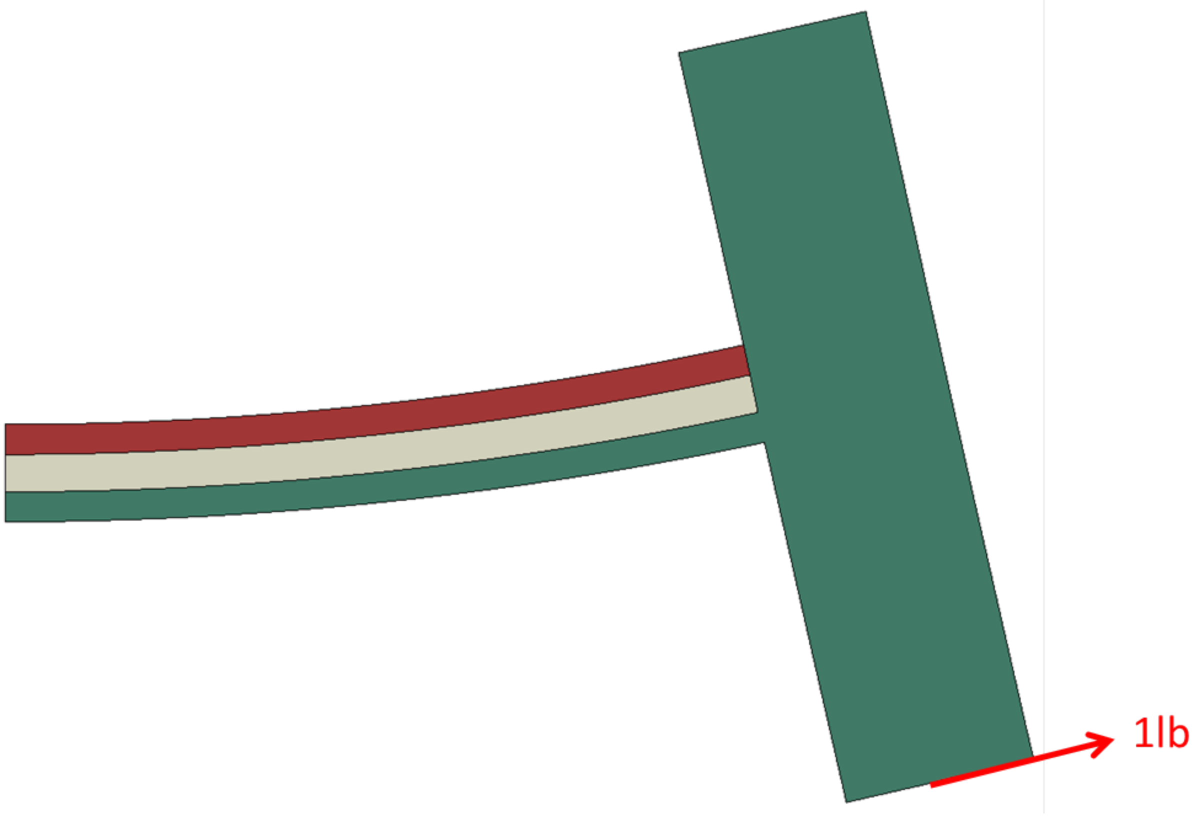

Figure 4-13: Deformed shape of PACTS FE model.

Four-node bilinear plane stress quadrilateral elements (CPS4R) and a constant 0.0254 mm [0.001 in] mesh size were used on each part of the model (Figure 4-14). The mesh size was chosen so that valid comparisons could be made when optimizing the lamina thicknesses of the PACTS tool between 0.0254 and 5.08 mm [0.001 and 0.2 in].

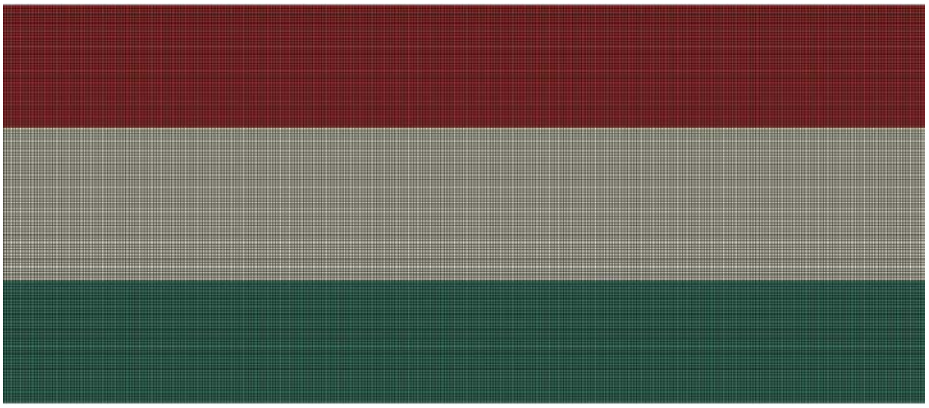

Figure 4-14: Mesh size 0.0254 mm [0.001 in] in each layer of the FE model.

Since the model is symmetric along the X-axis, a symmetry boundary condition was used. The XSYMM boundary condition of the two-dimension model restrains displacement in the X-direction and rotation about the Y and Z-axis (Figure 4-15).

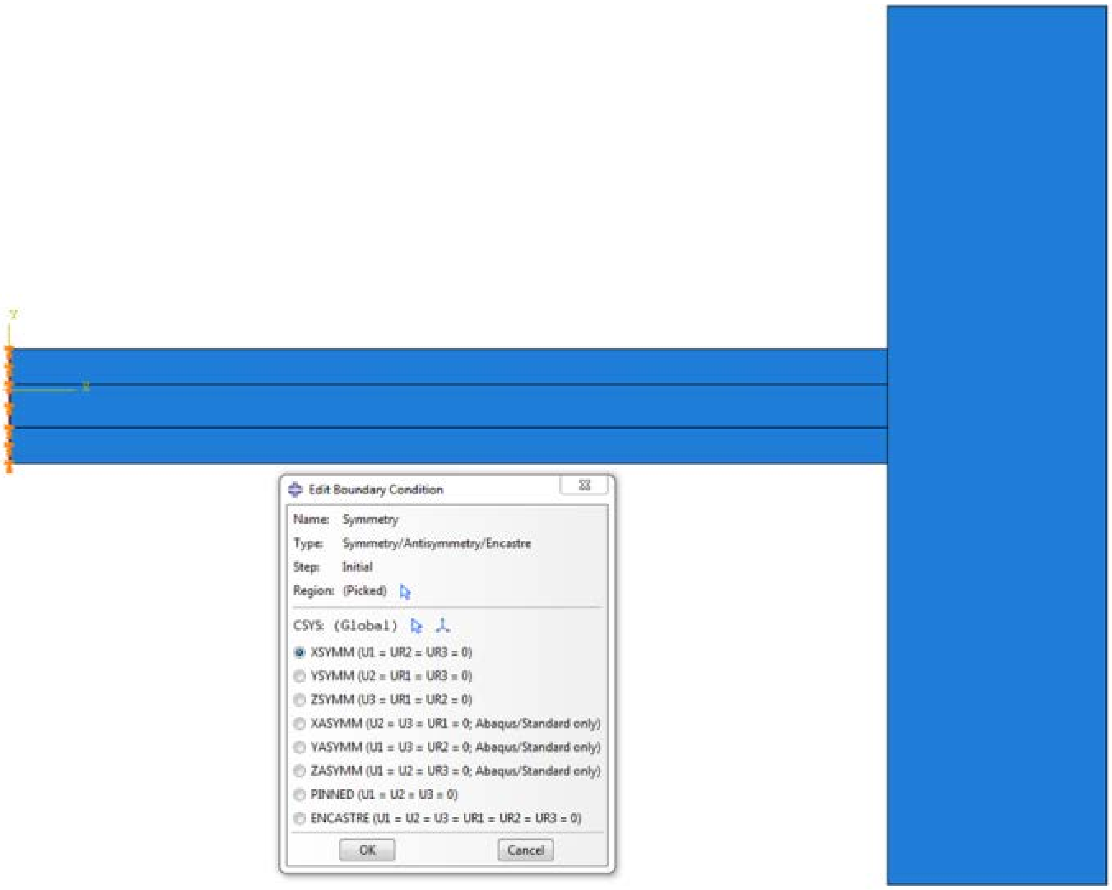

Name: Symmetry
Type: Symmetry/Antisymmetry/Encastre
Step: Initial
Region: (Picked)
CSYS: (Global)
● XSYMM (U1 = UR2 = UR3 = 0)
○ YSYMM (U2 = UR1 = UR3 = 0)
○ ZSYMM (U3 = UR1 = UR2 = 0)
○ XASYMM (U2 = U3 = UR1 = 0; Abaqus/Standard only)
○ YASYMM (U1 = U3 = UR2 = 0; Abaqus/Standard only)
○ ZASYMM (U1 = U2 = UR3 = 0; Abaqus/Standard only)
○ PINNED (U1 = U2 = U3 = 0)
○ ENCASTRE (U1 = U2 = U3 = UR1 = UR2 = UR3 = 0)

Figure 4-15: Symmetric boundary condition used in the Abaqus FE model of the PACTS geometry.

4.4 Summary

The results of the FE and CLPT theory indicated that the sensitivity of the PACTS tool was dependent on the geometry of the substrate, PZT, and bond layer of the system. The methods used in the modeling of the PACTS system were instrumental in determining the optimum design geometry for the prototype used in the experimental analysis of the tool sensitivity. The design of the PACTS was specifically oriented such that the PZT layer remained in compression when subjected to an applied load or displacement. Based on the FE analysis results, the initial design assumption was validated and the PACTS tool will operate below the ultimate compressive stress of the PZT.

CHAPTER 5: PACTS OPTIMIZATION

This chapter investigates the effects of the laminate material property on the sensitivity of the PACTS tool in order to optimize the sensing capabilities of the sensing tool. This analysis was done using the FE software and CLPT mentioned in Chapter 4. The resulting sensitivity or charge generated, by the PZT was plotted against the thickness of substrate.

5.1 Finite Element Results

Using the FE linear elastic model of the aluminum substrate, bond, and PZT layers described Chapter 3, each layer thickness was varied and the longitudinal mid-plane PZT layer strain values were analyzed. Based on the model geometry, loading, and boundary conditions chosen, the optimization process required a parametric study that varied material thickness ranges for each layer of the laminate. PZT thicknesses (t_p) ranges investigated were from 0.254 mm [0.010 in] to 2.54 mm [0.100 in]; bond thicknesses (t_b) between 0.0254 mm [0.001 in] and 1.016 mm [0.040 in]; and the aluminum substrate thicknesses (t_s) were between 1.016 mm [0.040 in] to 5.08 mm [0.200 in]. The specific thicknesses evaluated for each layer are presented in Table 5-1. The substrate thickness study was conducted on additional thickness sizes due to the adjustability of the H-shaped web that was initially fabricated to 5.08 mm [0.200 in]. Modifications to the standard shape could be made using a mill scale allowing more adjustability to the design. Bond thickness range was larger due to the application and shrinkage variations that can occur during the manufacturing and curing process. A total of 175 finite element models were created for this parametric study. From these models, the effects of varying the substrate web, bond layer, and PZT thicknesses were analyzed and an optimal shape was selected to use in the Proof of Concept testing.

Table 5-1: Laminate layer thicknesses used in the FE models generated for the optimization study.

PZT Thickness, t_p, mm [in]	Bond Thickness, t_b mm [in]	Substrate Thickness, t_s mm [in]
0.254 [0.010]	0.0254 [0.001]	1.016 [0.040]
0.508 [0.020]	1.27 [0.050]	1.27 [0.050]
1.016 [0.040]	2.54 [0.100]	1.905 [0.075]
2.032 [0.080]	5.08 [0.200]	2.54 [0.100]
2.54 [0.100]	6.35 [0.250]	3.175 [0.125]
-	-	3.81 [0.150]
-	-	5.08 [0.200]

From Chapter 4, it was determined that the voltage sensed in the PZT layer was proportional to the change in strain in the mid-plane of the PZT times the PZT layer. Therefore, the results presented in this section include the normalized charge generated in the mid-plane of the PZT plotted against the thickness of the substrate web. Since the laminate beam is in bending, it is assumed that the PZT is subjected to compression loading; therefore, the resulting voltage sensed is negative. In all cases, the magnitude of the charge generated and resulting maximum voltage sensed were used in the comparison of the sensing capabilities of the PACTS tool. The strain data was selected along the mid-plane path of the PZT layer in each model analyzed as illustrated in Figure 5-1.

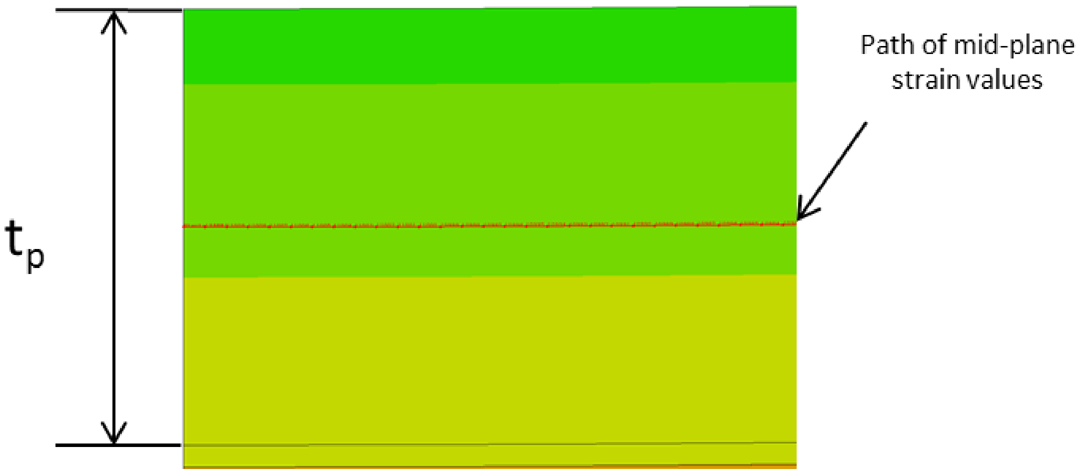

Figure 5-1: Path of FE model mid-plane strain values used from a PZT layer with a thickness of 0.508 mm [0.020 in].

5.1.1 Variation in Substrate Thickness

In analyzing the effects of each layer of the PACTS tool, it was important to investigate the impact of modifying the substrate web thickness from the general design. Figure 5-2 shows the individual effects of substrate layer thickness variation on the voltage sensed from the FE model. The PZT layer and bond layer thicknesses were held constant and are 0.508 mm [0.020 in] and 0.0254 mm [0.001 in] respectively. Model results indicated that the voltage sensitivity increased with increasing substrate web thickness as the substrate web thickness increased from 1.016 mm [0.040 in] to 5.08 mm [0.200 in]. These results were consistent for all models where PZT and bond thicknesses were held constant. The results for all model combinations conducted can be found in Appendix C.

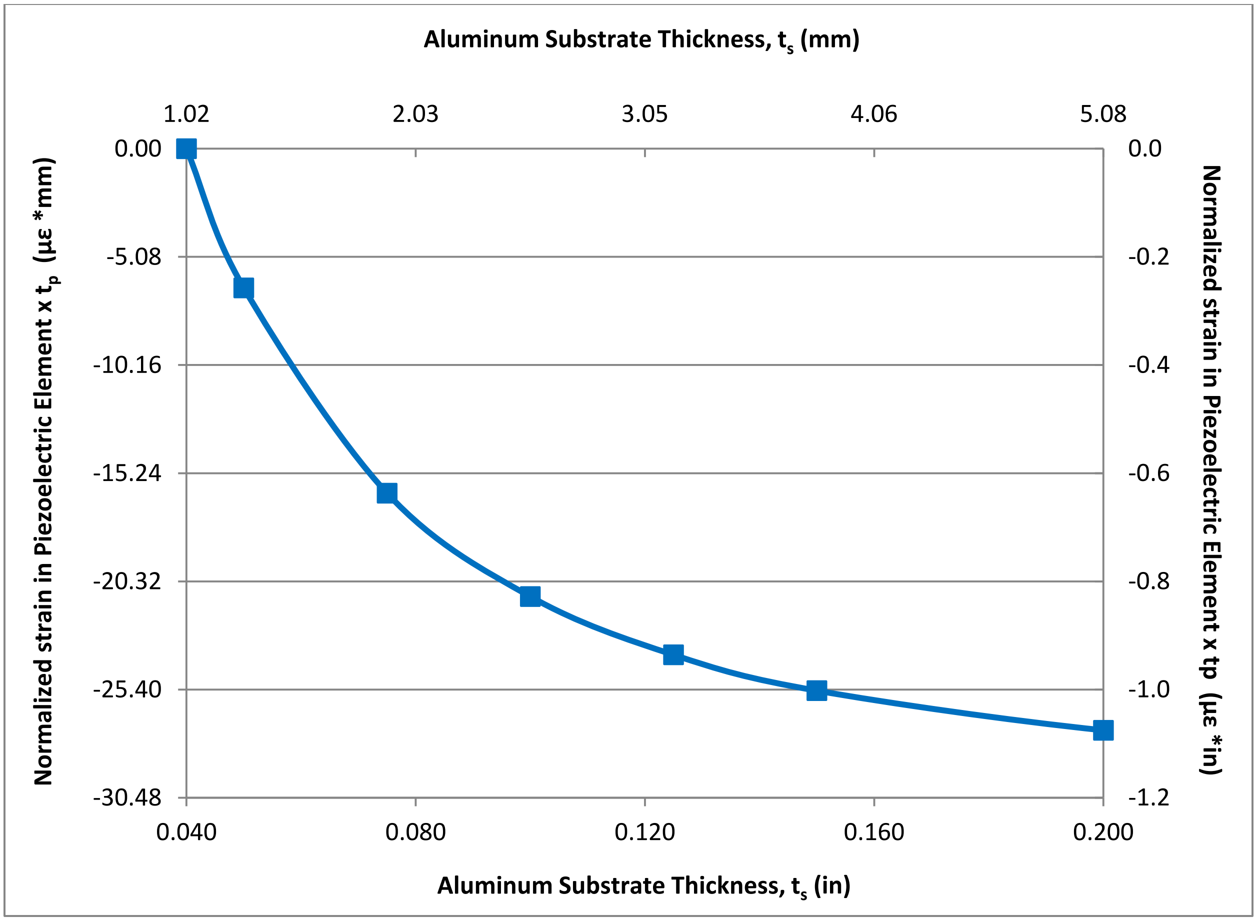

Figure 5-2: FE model results of PACTS voltage sensitivity as a function of the aluminum substrate thickness for a 0.508 mm [0.020 in] thick PZT layer and a 0.0254 mm [0.001 in] thick bond layer.

5.1.2 Variations in Bond Thickness

Bond thickness was found to be inversely related to the sensitivity of the PACTS tool. Figure 5-3 illustrates the sensitivity for a 0.508 mm [0.020 in] PZT layer thickness, where the bond thickness varied from 0.0254 mm [0.001 in] to 6.35 mm [0.25 in]. Results indicate that the sensitivity decreases with increasing bond layer thickness. As the thickness of the bond layer increases, it appears that the effects of shear lag significantly retard the sensing capabilities of the laminate. As the bond thickness increases, more and more energy is imparted to shear deformations in the bond, which means that less and less energy is imparted to the piezoelectric sensing material. Therefore, the bond layer thickness should be minimized to increase sensitivity of the system. Similar results were observed for all combinations of layer thickness and can be found in Appendix C.

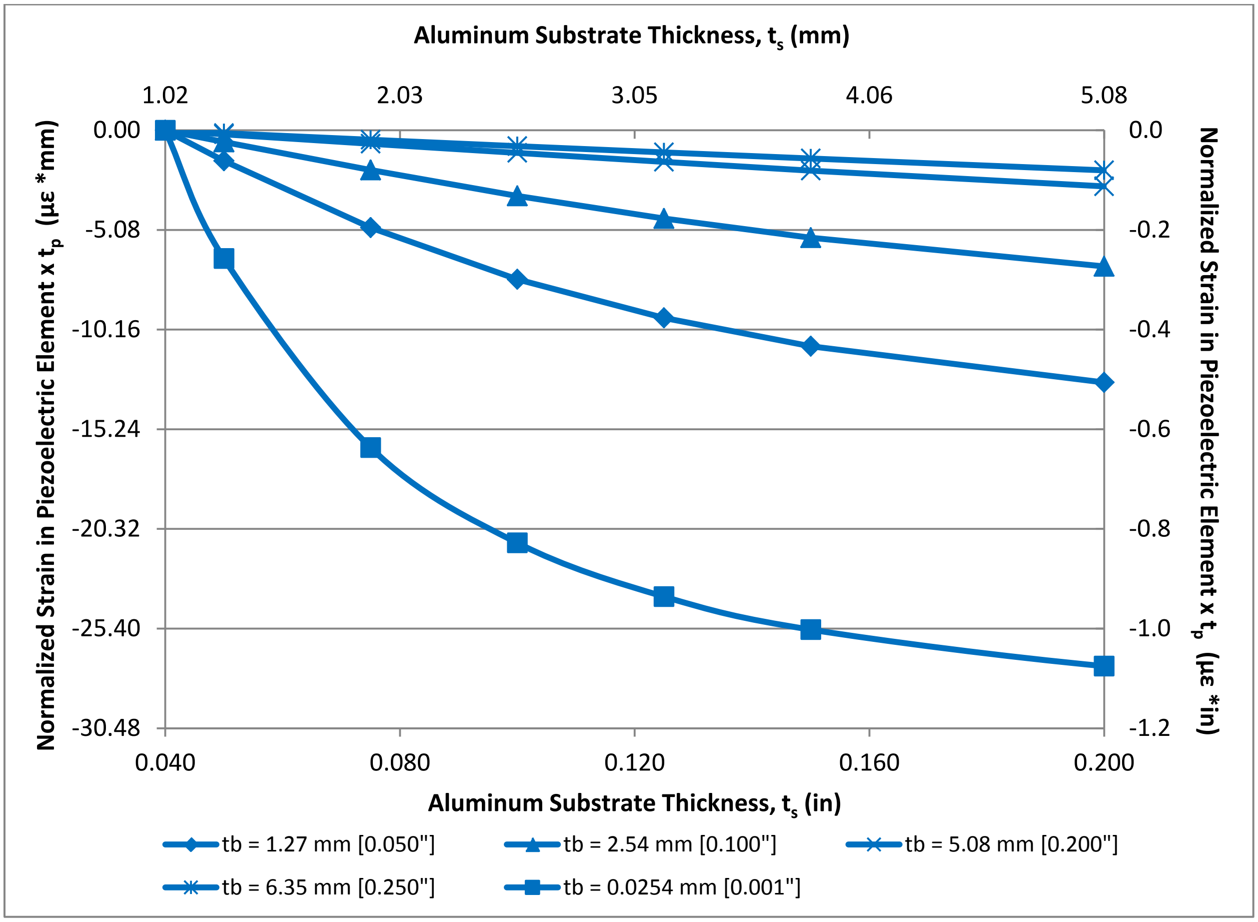

Figure 5-3: FE model results of PACTS voltage sensitivity for a 0.508 mm [0.020 in] PZT layer thickness as a function of the aluminum thickness and bond thicknesses ranging from 0.0254 mm [0.001 in] ≤ t_b ≥ 6.35 mm [0.25 in].

5.1.3 Variations in Piezoceramic Thickness

The effects of PZT layer thickness on the tool's voltage sensitivity were analyzed by varying the t_p thickness values from 0.254 mm [0.010 in] to 2.54 mm [0.100 in]. Based on the bond thickness analysis results, a constant thin 0.0254 mm [0.001 in] thickness was used and the sensitivity results using varying substrate and PZT thicknesses is located in Figure 5-4. Initially, the analytical model results indicated that for smaller substrate thicknesses between 1.016 mm [0.040 in] and 1.905 mm [0.075 in], the voltage sensitivity of the PACTS tool decreased with increasing PZT thickness. However, at larger substrate thicknesses the 0.508 mm [0.020 in] thick PZT geometry resulted in larger sensitivity results that increased with increasing aluminum substrate thicknesses. From the figure and the model results, it was determined that for a thin substrate thickness, in combination with thin bond thickness and large PZT thickness, the neutral axis of the composite member shifts upward. Therefore, the mid-plane strain in the PZT is under tensile loading conditions which resulted in positive sensitivity values at t_s = 1.27 mm [0.050 in], t_b = 0.0254 mm [0.001 in], and t_p = 2.54 mm [0.100 in]. However, as the substrate web thicknesses increase the PZT remains in compression; therefore, the PZT sheets operate below the ultimate compressive strength of the material.

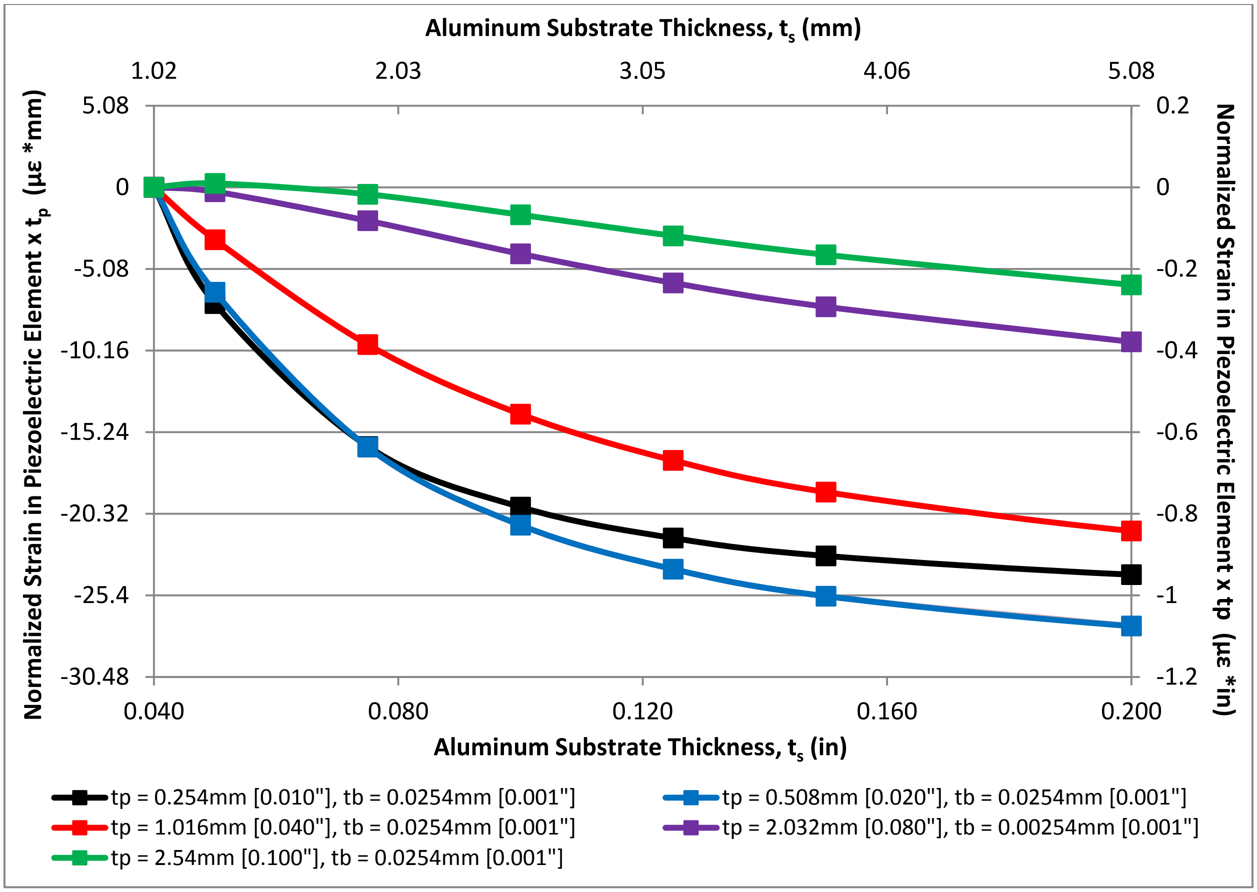

Figure 5-4: FE model results of PACTS voltage sensitivity as a function of PZT layer thicknesses and aluminum substrate thickness using a constant 0.0254 mm [0.001 in] bond layer thickness.

5.1.4 Summary of Results

The results for all 175 models were analzyed and compiled for comparison and are presented in Figure 5-5. The results illustrate that generally smaller PZT thickness in conjunction with a thin bond layer thickness will provide the most highly senstive results for all substrate web thicknesses. However, at a substrate web thickness of approximately 1.905 mm [0.075 in], the 0.508 mm [0.020 in] thick PZT layer begins to out perform the thinner 0.254 mm [0.010 in] thickness.

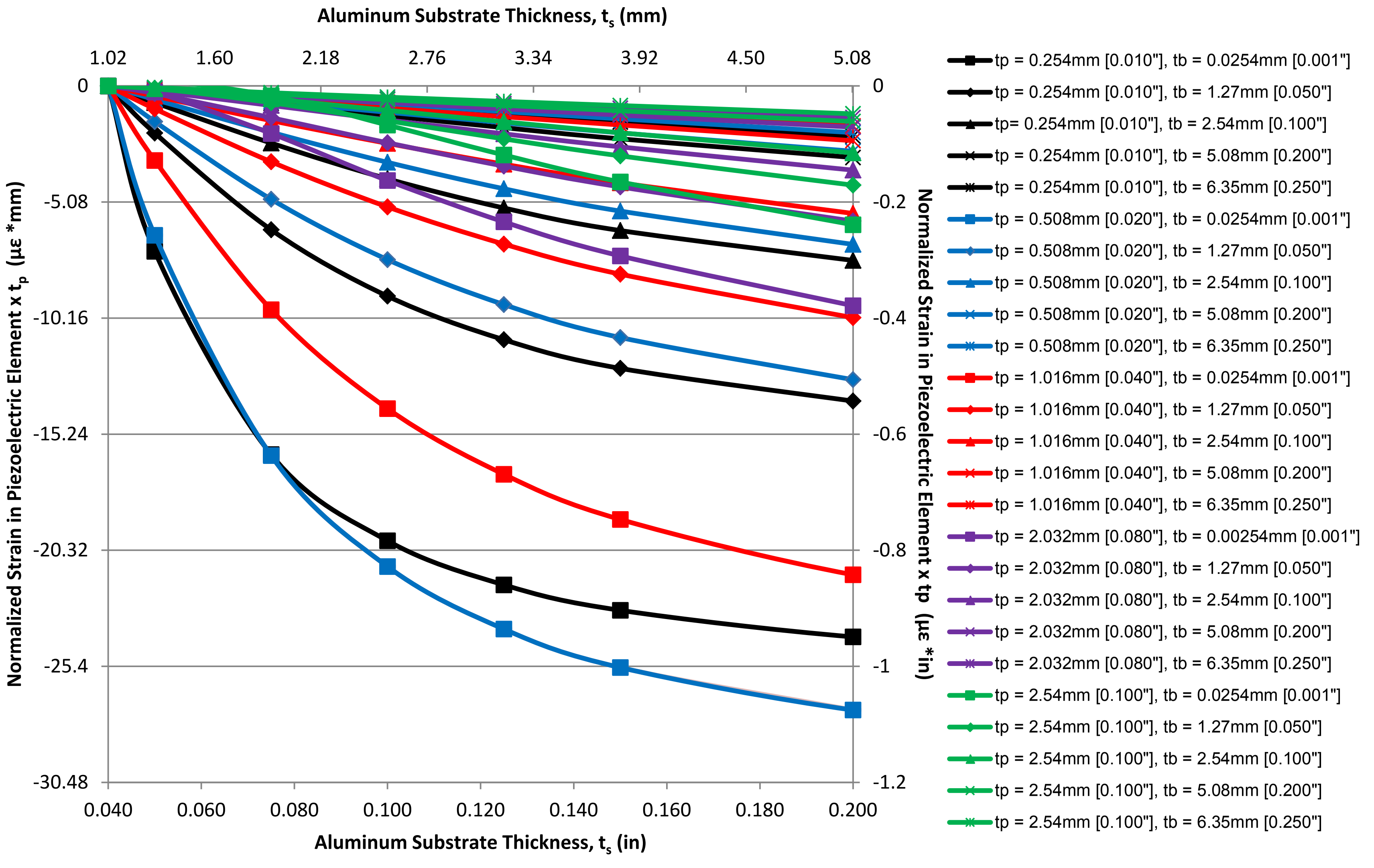

Figure 5-5: Parametric analysis of voltage sensitivity of the PACTS tool geometry as a function of PZT, bond material, and aluminum substrate layer thicknesses.

Based on the results of the parametric study, the PACTS tool geometry (Figure 5-6) with a substrate thickness of 1.905 mm [0.075 in] and a PZT sheet of 0.508 mm [0.020 in] were selected and manufactured to conduct experimental testing on an artificial crack. It was determined that the bond material thickness should be limited to production ability and the manufacturer’s instruction. After manufacturing the optimized geometry and adding the leg system, the resulting PACTS tool used in the the proof of concept testing weighed 20 g [0.044 lbs.]

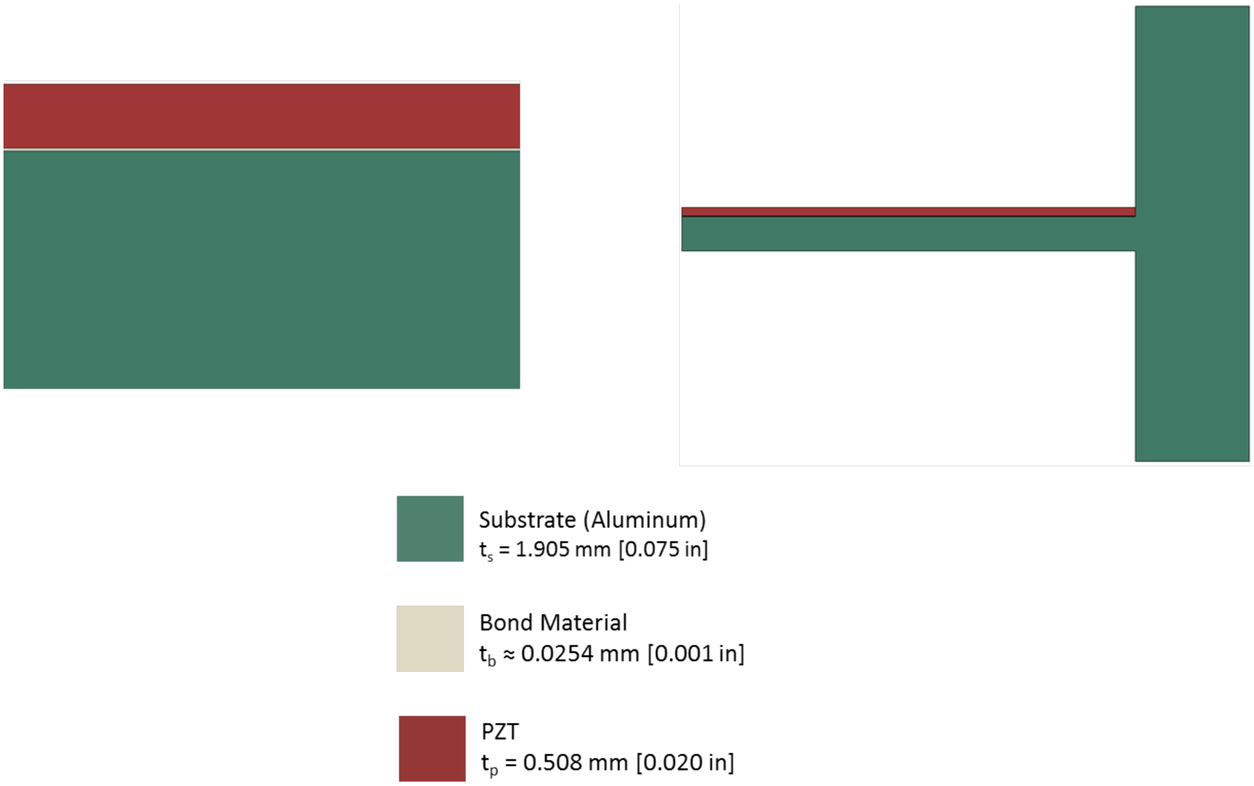

Figure 5-6: Optimized PACTS tool geometry selected for the proof of concept testing.

CHAPTER 6: PACTS PROOF OF CONCEPT

The primary objective of this chapter is to demonstrate the feasibility of the proposed piezoelectric sensor concept. This was carried out using the PACTS tool under laboratory conditions and analyzing the energy harvested by the sensor on an artificial crack and an acrylic compact tension specimen subjected to dynamic loading. This chapter identifies the test methods used and verifies the initial assumptions and hypothesis of this research. The results of the FE modeling and experimental test methods used for the PACTS tool with the optimal geometry determined in Chapter 5 are presented in this section.

6.1 Finite Element Analysis Results

FE results for the optimal PZT and substrate layer thickness of 0.508 mm [0.020 in] and 1.905 mm [0.075 in] respectively validate the assumption that the PZT layer would be subjected to compressive strains, due to the deformation of the PACTS geometry when loaded. The FE results are shown in Figure 6-1. The deformation scale for the figure is 400 and the strain data shown in the legend were selected to emphasize the compressive longitudinal strain values of the tool geometry.

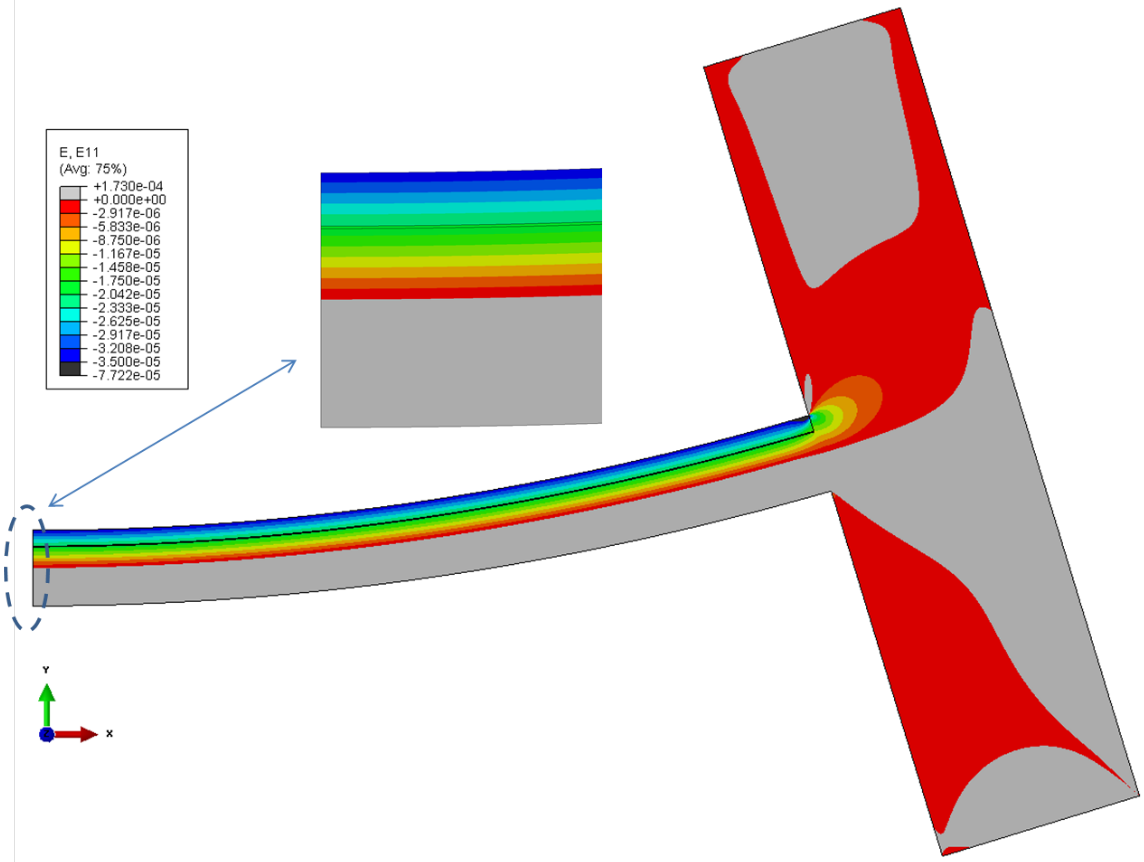

Figure 6-1: FE longitudinal mid-plane strain results for the selected PACTS tool geometry, where t_p = 0.508 mm [0.020 in], t_b = 0.0254 mm [0.001 in], and t_s = 1.905 mm [0.075 in], verifying that the PZT layer is in compression under testing conditions for the selected geometry.

6.2 Artificial Crack System Experiment

An Artificial Crack System (ACS) was fabricated in order to investigate the sensitivity of the PACTS tool and its ability to detect an active crack. The ACS provided a crack length of 300 mm [11.8 in] that was used to analyze the effectiveness of the PACTS tool. The artificial crack was composed of two steel plates including a main post and a swing arm. The two steel plates rotate about a hinge point that functioned similarly to a crack tip. A specified displacement can be applied to the apparatus that allows the swing arm surface to separate from the main post. This separation from the main post results in an edge crack under fracture Mode I opening that could be spanned by the PACTS tool. Fabrication drawings for the ACS are located in Appendix D.

6.2.1 Test Set-Up and Equipment

The experimental crack length of the ACS was 300 mm [11.8 in] and the applied displacement was 0.38 mm [0.015 in] at a distance of 340 mm [13.4 in] from the artificial crack tip. The applied displacement was measured and recorded using a Starrett displacement gage. Displacement was applied to the artificial crack at a frequency of 1Hz and maintained using an Electronome Metronome. The PACTS tool was applied to the specimen so that it spanned the crack opening. Data were collected at 10 mm [0.39 in] increments along the length of the artificial crack. At each increment, the displacement was applied dynamically for 60 seconds and the voltage readings from the multimeter were recorded. The experimental test set-up and the equipment used are illustrated in Figure 6-2.

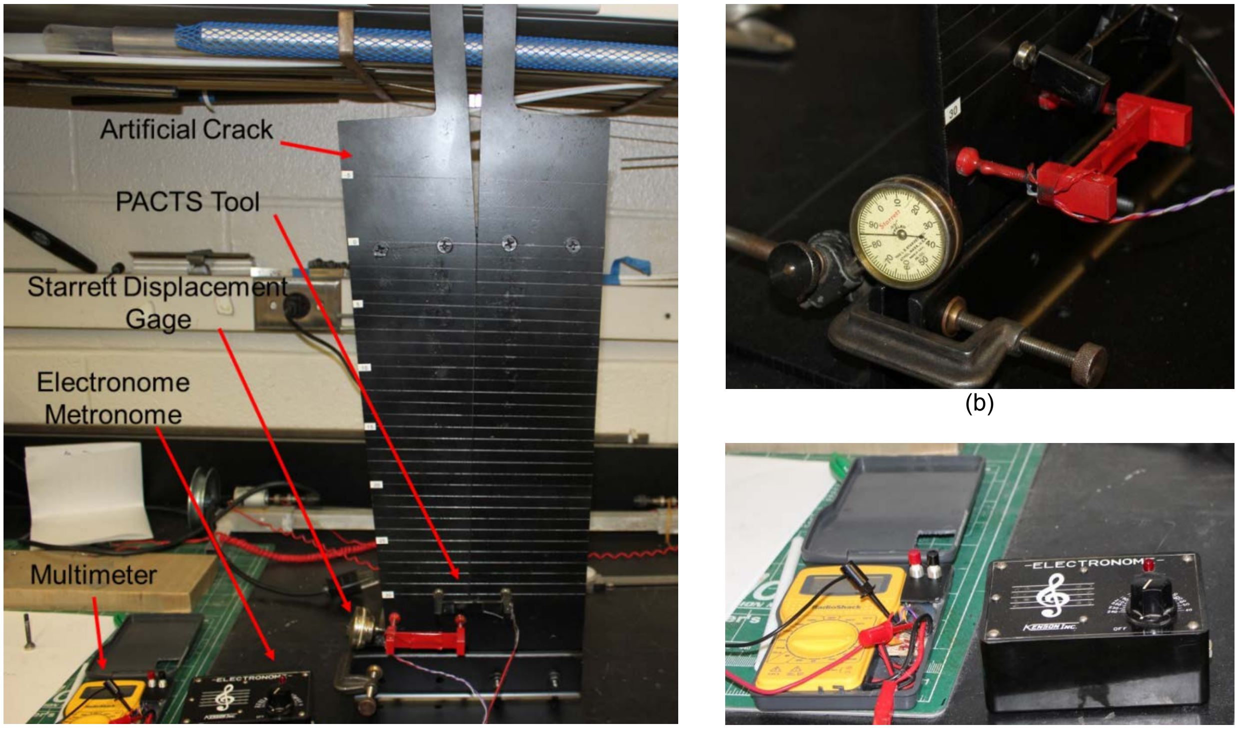

(a) (b) (c)

Figure 6-2: Artificial Crack Test-Set illustrating the (a) labeled artificial crack specimen and testing equipment; close up images of the (b) displacement gage, PACTS tools; and the (c) multimeter and metronome used.

6.2.2 Test Results

The results of the ACS test indicate that the sensor is actively detecting the presence of an active crack. Voltage reading values increased with increasing distance away from the artificial crack tip. These results correlate to geometric fracture principles where crack opening displacement increases linearly as the distance from the crack tip increases. However, at a distance less than 50 mm [2.0 in] from the artificial crack tip the results indicate non-linear behavior. The results presented are similar to issues identifying crack tips in real structures where areas near the crack tip typically include regions of plastic deformation outside of the linear elastic analysis region under consideration within this research. The non-linearity of ACS results could be due to fabrication and design of the hinge point. However based on the linear region of the data, the crack tip could be extrapolated using the slope of the linear region to the location of the artificial.

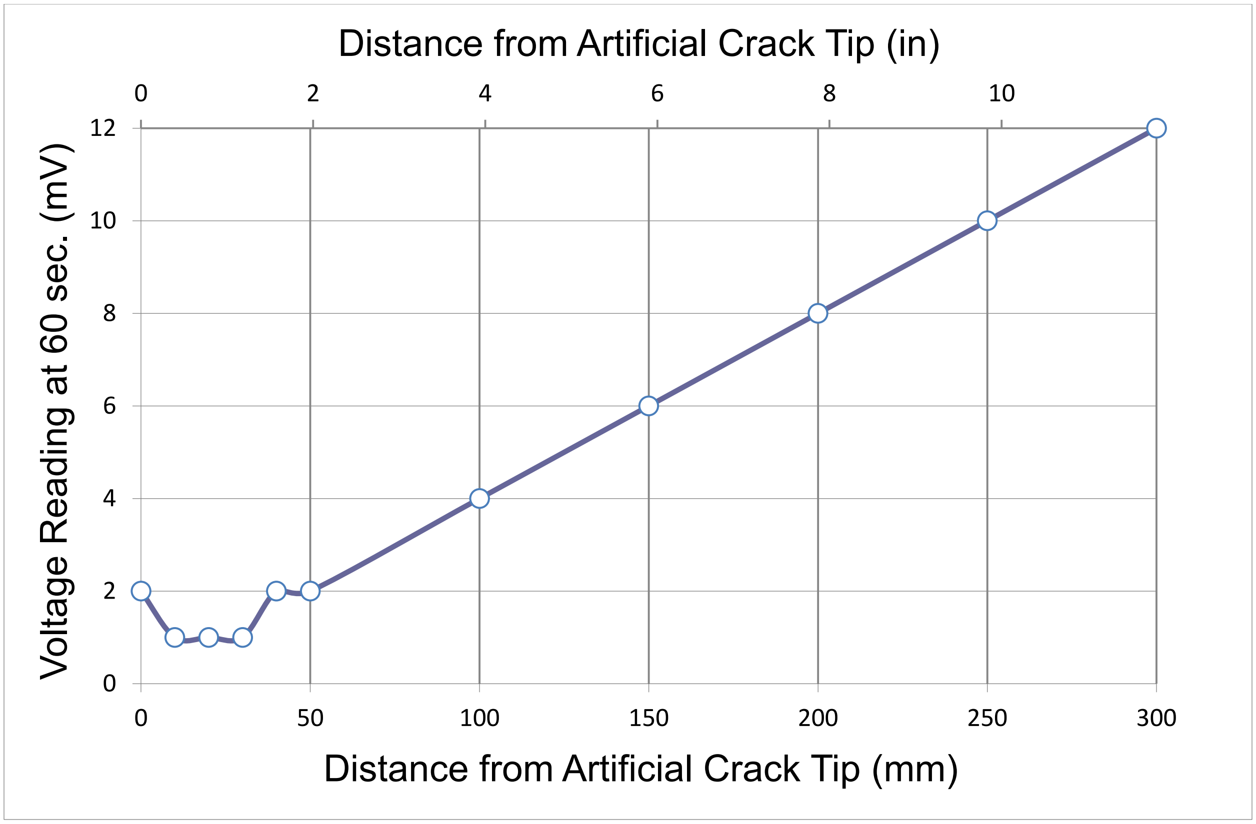

Figure 6-3: Voltage reading at 60 seconds using a 1000 μF capacitor and 50kΩ of resistance in the PZT sensing circuit when a 0.381mm [0.0150 in] displacement (measured at 340 mm [13.4 in] from the artificial crack tip) is applied at a frequency of 1Hz.

6.2.3 Summary

The PACTS tool successfully detected the presence of an active crack. The sensitivity capabilities of the PACTS tool accurately detected the presence of crack opening displacement along the length of the artificial crack up to 0.056 mm [0.0022 in]. At a location of 50 mm [2.0 in] from the artificial crack tip, a change in slope within linear trend of PACTS voltage sensitivity was observed. Using only the crack opening linear trend (COLT) data, the crack tip position could be effectively determined. The results also suggest that the location of the crack tip could be determined based on the slope change of the PACTS voltage data.

6.3 Crack Tip Identification and Location

After successfully using the PACTS system to identify active crack opening displacements on the steel ACS, the tool was used to evaluate the ability to identify the crack tip in an acrylic specimen. Therefore, a 38.1 mm [1.5 in] thick acrylic sheet was cut to the Compact Tension (CT) specimen requirements as per ASTM E399 (2012). The dimensions and straight through notch crack size of the acrylic CT specimen is illustrated in Figure 6-4 and the material characteristics of the acrylic specimen are described in Appendix A.

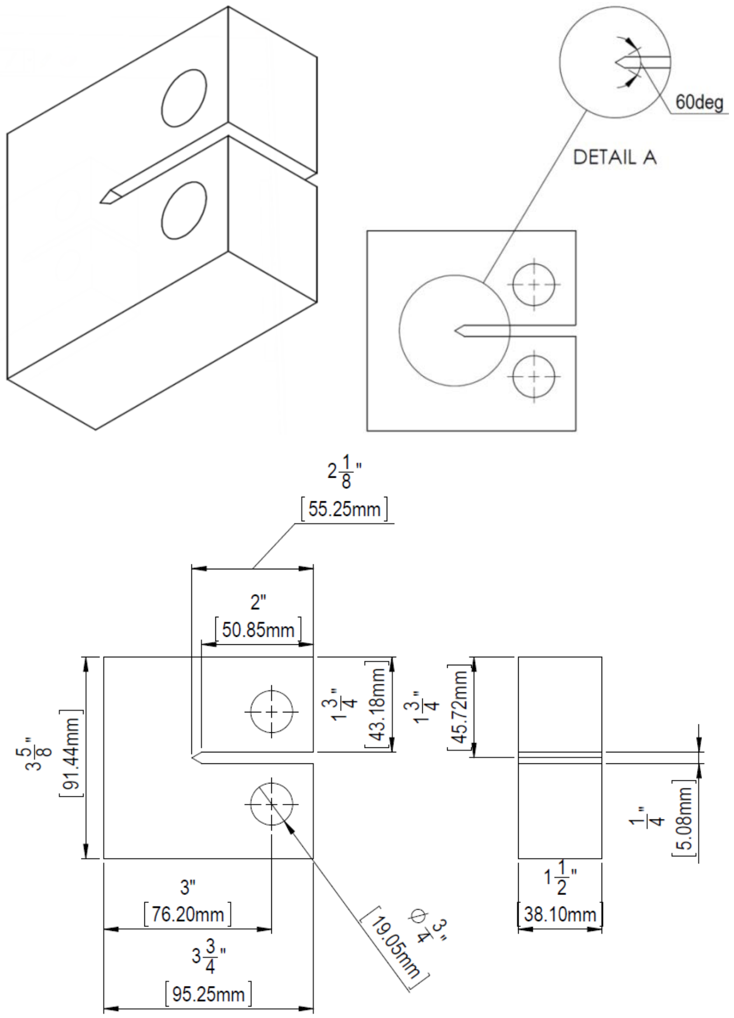

Figure 6-4: Acrylic compact tension specimen geometry used for the crack tip identification testing.

6.3.1 Test Set-Up and Equipment

The CT specimen was marked in 1 cm [0.39 in] increments from the crack tip, up to 20 mm [0.79 in] ahead of the crack tip and 50 mm [1.97 in] behind the crack tip as illustrated in Figure 6-5 (a). A 1.5 m [5 ft] long aluminum beam was attached to the surface of the CT specimen with a load attached to the cantilever end as shown in Figure 6-5 (b). The CT specimen was dynamically loaded at 2.2 Hz. The PACTS tool was placed across the crack at 10 mm [0.39 in] increments along the CT specimen while it was loaded dynamically for 60 seconds at each increment, similarly to the ACS test.

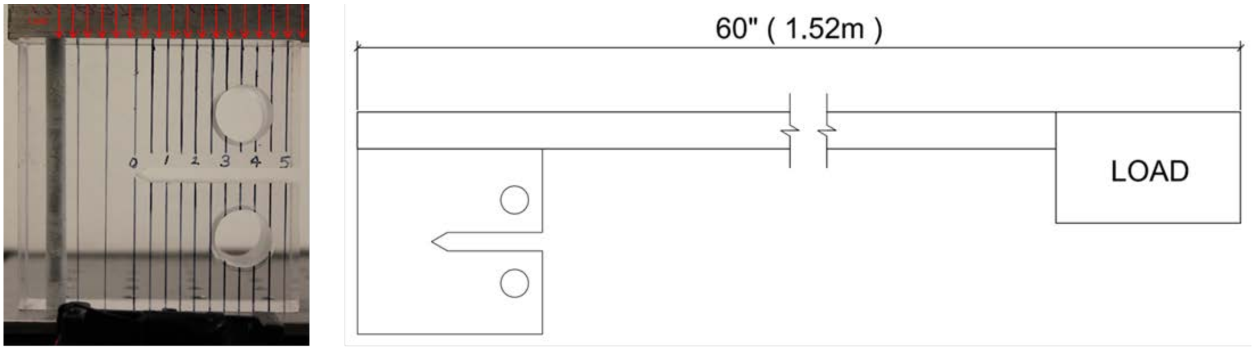

(a) (b)

Figure 6-5: (a) Acrylic test specimen used in the in the (b) crack tip boundary identification experiment.

6.3.2 Results

PACTS tool testing was conducted up to 20 mm [0.79 in] ahead of the crack tip and 50 mm [1.97 in] behind the crack tip. The voltage readings from the PACTS tool after 60 seconds of cycling are shown in Figure 6-6. As theorized and shown using the ACS test set-up, the voltage sensed results increase with increasing distance from the crack tip. The voltage sensed continued to decrease ahead of the crack tip as it approached an area of zero displacement within the material. Results also indicate a region of non-linear response near the crack tip of the specimen. These results confirm the test data acquired using the ACS test setup.

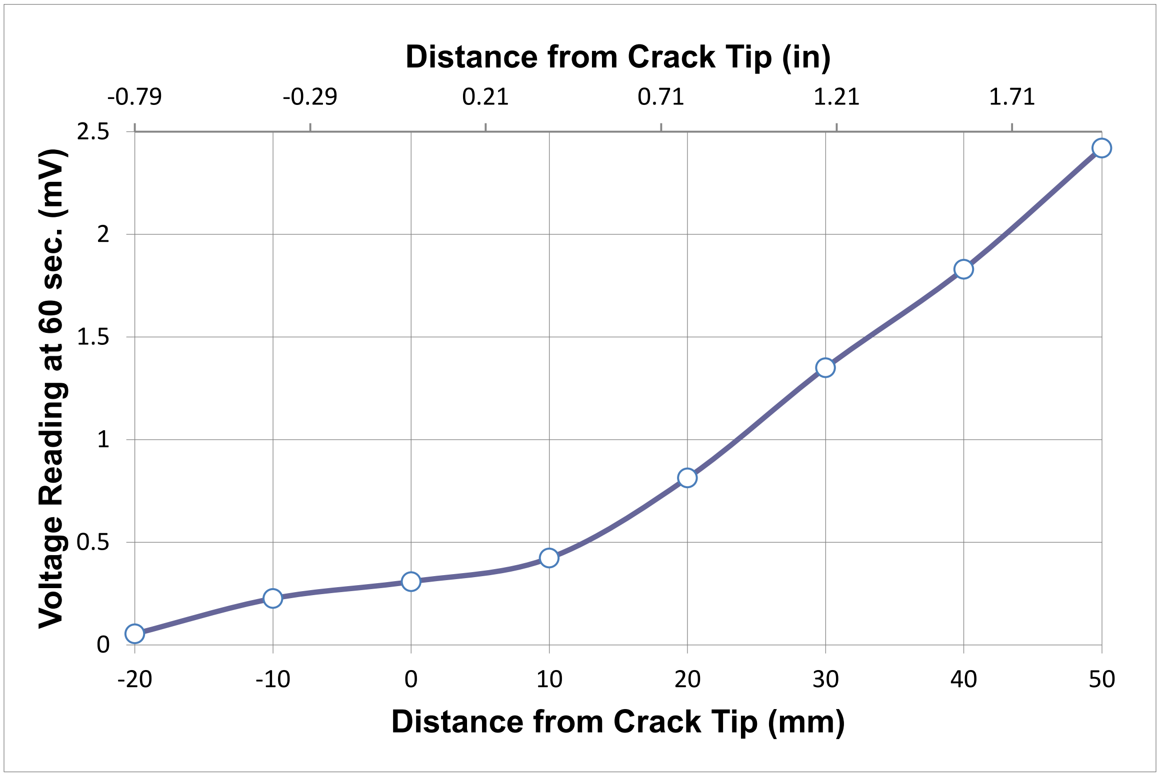

Figure 6-6: Voltage readings taken at 10 mm [0.39 in] increments along the test specimen over 60 seconds at a frequency of 2.2 Hz

Based on the test results, a linear relationship exists between the voltage reading and the distance behind and ahead of the crack tip (Figure 6-7). Similarly to the ACS results, non-linear sensing is evident near the crack tip region. Using a COLT analysis, the crack tip position could be located within 2.72 mm [0.107 in]. However, it is hypothesized that the location of the crack tip can be estimated using the change in slope from the linear region of the test data. In order to determine the location of the crack tip of the specimen, additional analytical calculations were required.

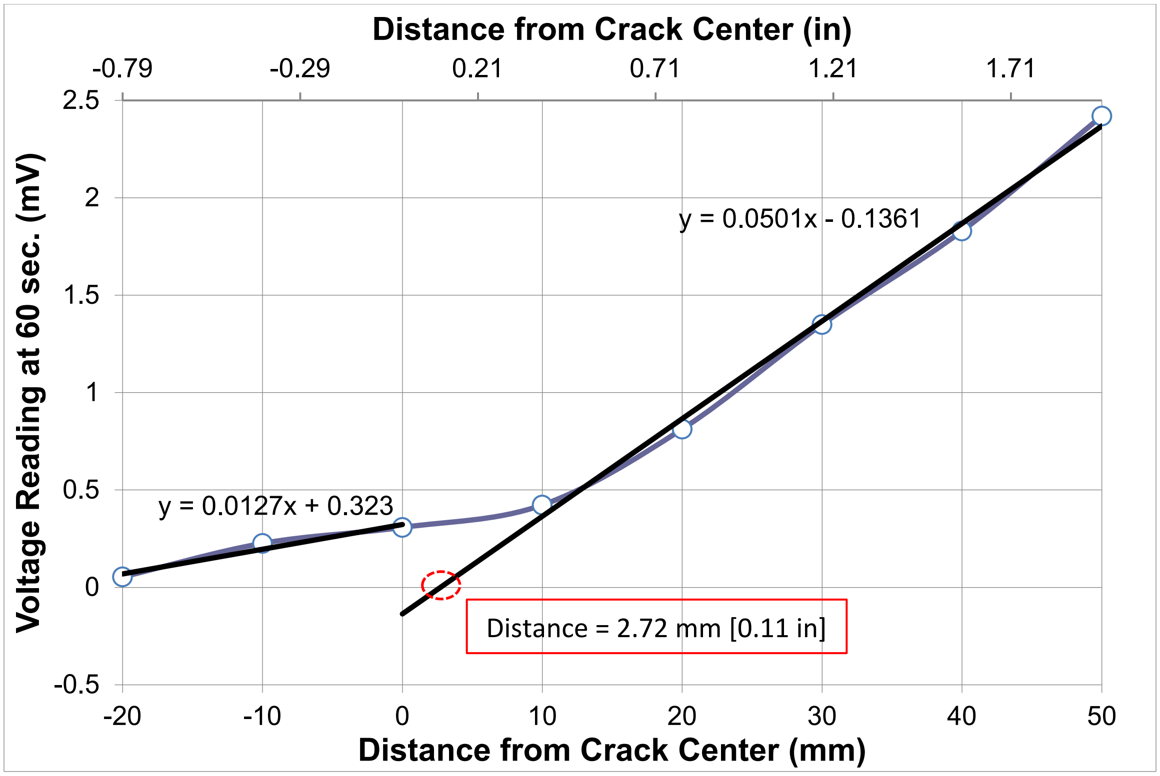

Figure 6-7: Voltage reading taken over 60 seconds at frequency of 2.2 Hz with trend lines added to the linear regions behind and ahead of the crack tip.

6.3.3 Crack tip location determination

To identify the crack tip location based on the change in slope of the linear data, it was important to identify a line tangent to the non-linear region, between 0 mm [0 in] and 20 mm [0.79 in], that also includes the location of the crack tip at (0, 0). From the test data and the equation of the non-linear region, it was determined that a line through (0, 0) that is tangent to the non-linear portion at 14.8 mm [0.58 in] and 0.583 mV had a slope of 0.0339 as shown in Figure 6-8.

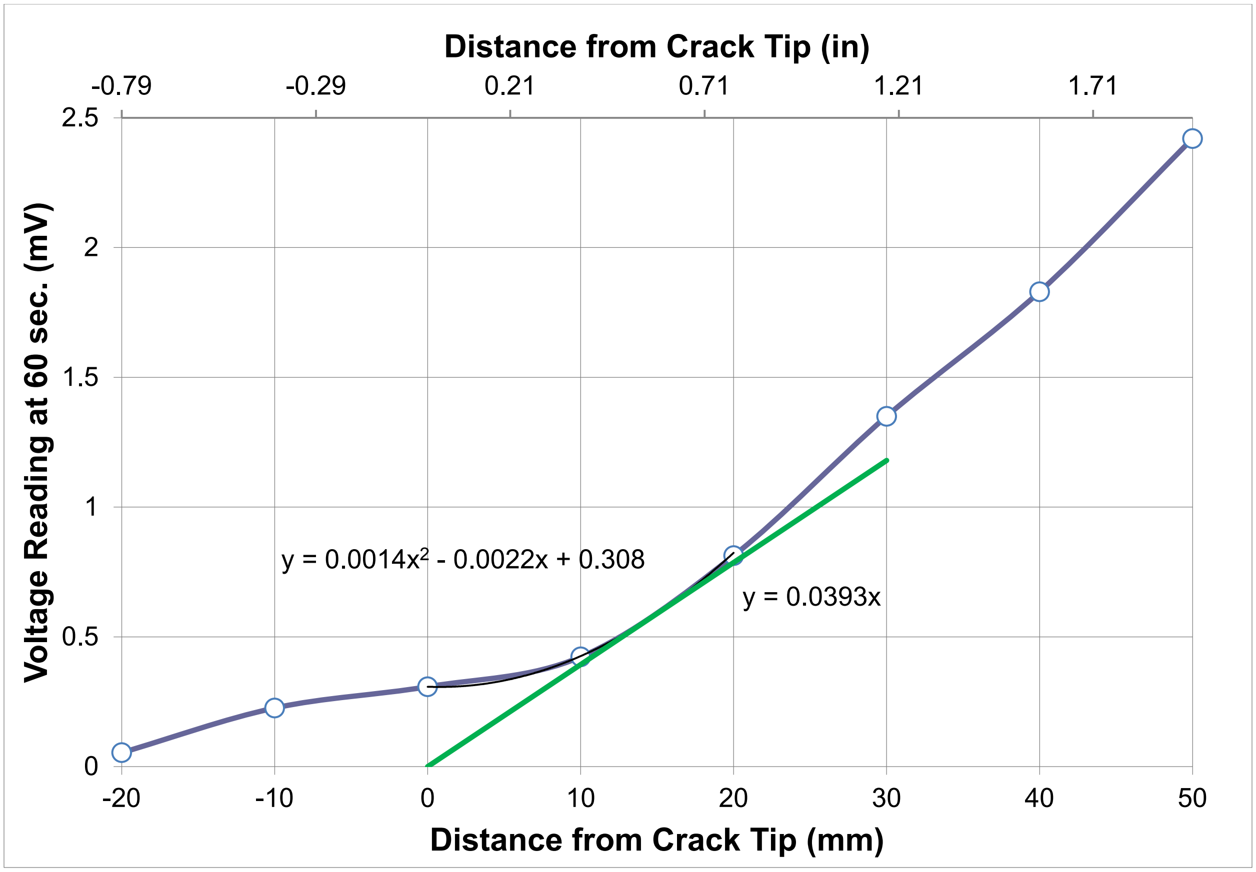

Figure 6-8: Voltage reading along the length of the cracked specimen taken over 60 seconds at frequency of 2.2 Hz with a line tangent to the non-linear portion that includes the location of the crack center.

A comparison of the slope of the linear region of the experimental results and the constructed tangent line from the non-linear region to the crack tip boundary is illustrated in Figure 6-9. Based on the results, it appears that the tangent line from the non-linear region to the crack tip has a smaller slope of 0.0393 in comparison to linear portion of the data (0.0508). Using the change in slope between the linear and non-linear regions of the results, the crack tip boundary within the acrylic specimen can be determined. As the slope of the linear portion approaches the non-linear region and intersects the tangent line, the slope of the data (0.0508) is reduced by 21.6% to 0.039. At this 21.6% slope reduction from the linear region of the data, a line can be drawn from the constructed tangent line to the crack tip boundary of the acrylic test specimen.

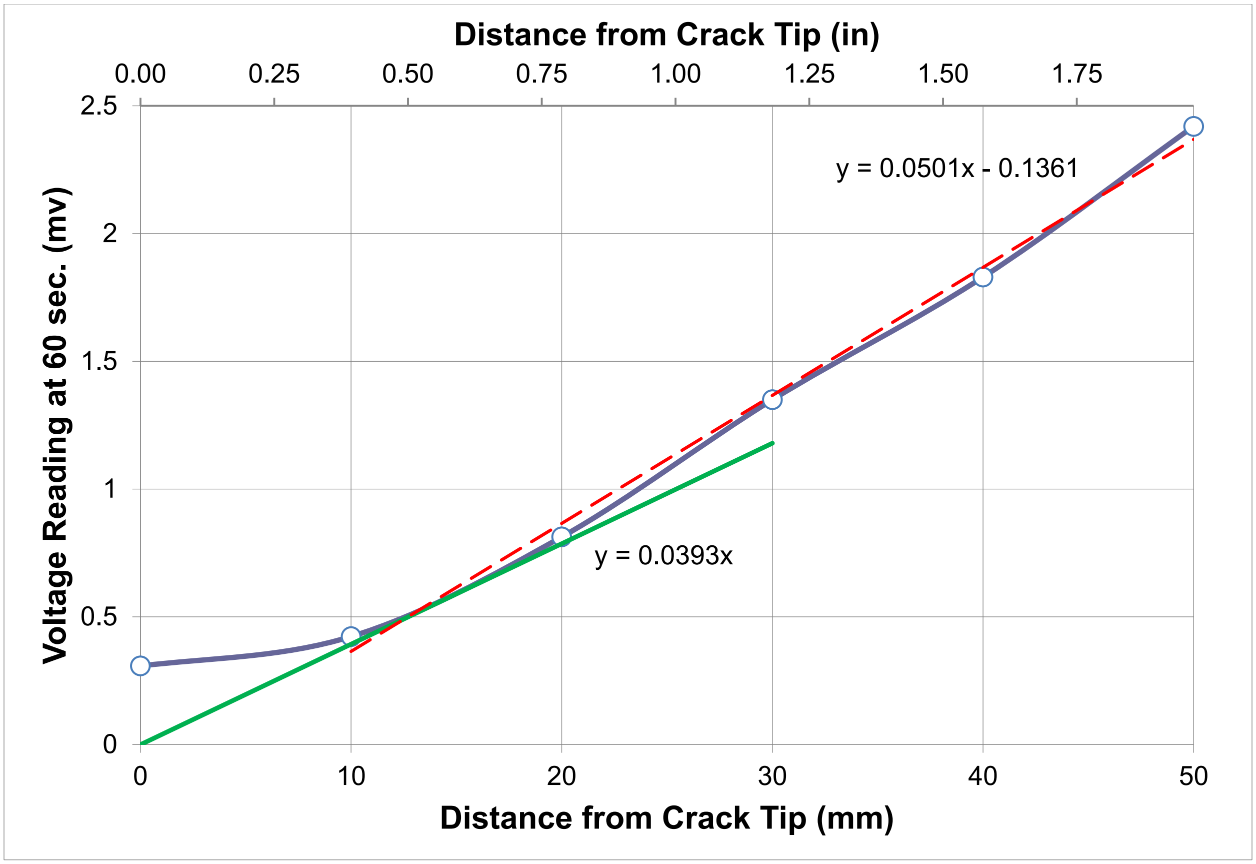

Figure 6-9: Slopes of the linear region and the constructed tangent line used to identify the crack front boundary of the acrylic specimen.

6.3.4 Summary

The results of the dynamically loaded acrylic specimen testing confirmed the results of the ACS test, where the PACTS tool's sensing abilities were determined to be effective in the identification of active cracks. Additionally, the test conducted on the acrylic specimen illustrated the ability of the PACTS tool sensing data to be used in the identification and location of the crack tip boundary within a material specimen. For the acrylic test specimen, when a 21.6% slope reduction is identified the crack tip boundary could be extrapolated using the linear and non-linear portion of the data curve. However using only the linear portion of the curve, the crack tip boundary location can be estimated within < 3mm [< 1/8 in].

CHAPTER 7: SUMMARY AND CONCLUSION

7.1 Summary of Findings

The results of this research study successfully demonstrate the sensing ability of the Piezoelectric Active Crack Tip Sensor (PACTS) tool in identifying active cracks and the location of the crack tip boundary within a material. The results show a clear relationship between the voltage sensing of the PACTS tool and the opening displacement of a cracked surface at distances behind the crack tip boundary of a dynamically loaded material. Active cracks with 0.056 mm [0.0022 in] opening displacements were detected using an artificial crack system. Using a COLT analysis technique, the new tool could be used immediately to determine planar crack tips to within 3mm [0.12 in] accuracy without the use of a correction or modification factor on a standard 38.1 mm [1.50 in] thick acrylic crack specimen. It was determined that if a 21.6% reduction in sensor slope with spatial length is detected, then the resulting crack tip location could be determined to within 0.254 mm or 1/100th of an inch. Based on the data, it was determined that the crack tip boundary location can be accurately identified and documented in a material for future inspection, monitoring, or maintenance.

7.2 Conclusion

The sensitivity of the PACTS tool can effectively be used in the inspection and monitoring of crack growth within bridges and other structures under dynamic loads. The PACTS tool can be used to physically sweep across an active crack and identify the location of the crack tip. Typically multiple cracks appear in a given structure including those that branch off from an existing crack as shown in Figure 7-1, resulting in multiple crack tips. However, the sensitivity of the PACTS system can potentially be used to identify the most active crack tip that is effectively dominating crack growth within the material. This new technology can be used and potentially replace the application of strain gages on a material. Since during active crack growth, the use of standard strain gages become ineffective once the crack grows at the location of the gage. The PACTS tool is capable of spanning the crack and detecting the opening displacements of the existing crack under loaded conditions. The development of the PACTS provides a lightweight and effective crack inspection tool that can be used to accurately identify and characterize active cracks within metallic structures under dynamic loading.

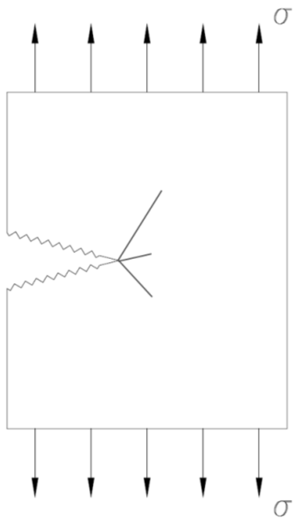

Figure 7-1: Edge crack with multiple cracks fronts.

The results of the research can be used by inspectors and managers to successfully determine repair and maintenance needs for the aging bridge infrastructure. The sensitivity of the PACTS tool successfully identified active cracks with opening displacements below those measured using alternative SHM methods (Yu et al. 2011). Future analysis and testing of the PACTS tool should be conducted to determine its application limits and constraints.

7.3 Recommendations for Future Work

The findings outlined in this dissertation demonstrate the potential for the PZT sensing PACTS tool in the field of crack detection and characterizations. However, additional investigations into the applications and sensitivity adjustments should be conducted prior to marketing this sensor technology. Additional investigation can include but are not limited to the following:

- Statistical analysis to determine which geometric parameter provides the maximum effect on the effectiveness of the PACTS tool.
- Identification of opening displacement limitations on the PACTS tool.
- Using the crack tip identification technique on 3-dimensional cracked structures with complex structural geometries and crack paths.
- Experimental testing of machine flawed specimens to determine ability to detect subsurface discontinuities in a material.
- A comparison of crack detection ability with various other inspection techniques and SHM systems.
- Experimental testing of pre-cracked steel structures under dynamic loading including correlations between crack opening displacements and the sensing capabilities of the PACTS system.
- Experimental testing on fatigue cracks in steel structures under dynamic loading.
- Field testing of in-service bridge structures with existing cracks.

REFERENCES

AASHTO (2008). *Manual for Bridge Evaluation*, American Association of State Highway and Transportation Officials (AASHTO), Washington, DC.

Agarwal, B. D., and Bhagwan, D. A. (2006). *Analysis and Performance of Fiber Composites*, Hoboken, N.J. : John Wiley, Hoboken, N.J.

ASCE (2013). "2013 Report Card for America's Infrastructure."

ASME (2010). "Rules for In Service Inspection for Nuclear Power Plant Components." *ASME Boiler and Pressure Vessel Code*, ASME, New York.

ASTM (2012). "ASTM Standard E399-12e3." *Standard Test Method for Linear-Elastic Plan-Strain Fracture Toughness, KIC of Metallic Materials*, ASTM International, West Conshohocken, PA.

Barrett, R. M. (2013). "Introduction to Adaptive Aerostructures." University of Kansas.

Barsom, J. M., and Rolfe, S. T. (1999). *Fracture and Fatigue Control in Structures : Applications of Fracture Mechanics*, ASTM, West Conshohocken, PA.

Boresi, A. P., and Schmidt, R. J. (2003). *Advanced Mechanics of Materials*, John Wiley & Sons, New York.

Chopra, I., and Sirohi, J. (2013). *Smart Structures Theory*, Cambridge, England : Cambridge University Press.

CTS (2013). "PZT5A AND 5H Product Data Sheets." <http://www.ctscorp.com/>. (7/7/2014, 2014).

FHWA (2001). "Reliability of Visual Inspection for Highway Bridges, Volume I: Final Report." F. H. Administration, ed.McLean, VA.

FHWA (2011). "FHWA Brige Programs Structure Type by Year Built." <www.fhwa.dot.gov/bridge/structyr.cfm>.

FHWA (2012). "Feasibility of Nondestructive Crack Detection and Monitoring for Steel Bridges." F. H. Administration, ed.

Fuchs, H. O., and Stephens, R. I. (1980). *Metal Fatigue in Engineering*, Wiley, New York.

Gautschi, G. (2002). *Piezoelectric Sensorics: Force, Strain, Pressure, Acceleration and Acoustic Emission Sensors, Materials and Amplifiers*, Springer - Verlag Berlin Heidelberg, Berlin.

Hellier, C. (2013). *Handbook of Nondestructive Evaluation*, McGraw-Hill, New York.

HSE (2006). "Probability of Detection (PoD) Curves: Derivations, applications and limitations." Health and Safety Executive, London.

Ihn, J. B., Chang, F. K., Ihn, J. B., and Chang, F. K. (2004). "Detection and Monitoring of Hidden Fatigue Crack Growth Using a Built-In Piezoelectric Sensor/Actuator Network: I. Diagnostics." *Smart Mater. Struct.*, 13(3), 609-620.

Jalinoos, F. (2009). "NDE Showcase for Bridge Inspectors." FHWA, ed.

Jones, R. M. (1975). *Mechanics of Composite Materials*, Washington, Scripta Book Co., Washington.

Lynch, J. P. (2004). "Detection of Structural Cracks Using Piezoelectric Active Sensors." *17th ASCE Engineering Mechanics Conference*, ASCE, University of Delaware, Newark, DE.

Morgan Advanced Materials (2009). <http://www.morganelectroceramics.com/>. (6/10/2014, 2014).

NDEC, N. E. C. (2010). "NDEC News." FHWA, ed.

Piezo Systems Inc. (2011). <http://piezo.com/>. (4/12/2013, 2013).

Purvis, R. L. (1988). "Inspection of Fracture Critical Bridge Members." *Transportation Research Record*(1184).

Rolfe, S. T. (1993). "Fitness for Service - Common Sense Enginering." *Proc., The Art and Science of Structural Engineering : proceedings of the symposium honoring William J. Hall*, Prentice Hall, xxxiii, 238 p.

Sanford, R. J. (2003). *Principles of Fracture Mechanics*, Prentice Hall, Upper Saddle River, NJ.

Silva, A. S. S., Oliveira, D. F., Machado, A. S., Nascimento, J. R., and Lopes, R. T. (2014). "An Evaluation of Imaging Plate Characteristics that Determine Image Quality in Computed Radiography." *Mater Eval*, American Society of Nondestructive Testing, Columbus, Ohio.

Sirohi, J., and Chopra, I. (2000). "Fundamental understanding of piezoelectric strain sensors." *J. Intell. Mater. Syst. Struct.*, 11(4), 246-257.

Wells, A. A. (1981). "The Meaning of Fitness-for-Purpose and Concept of Defect Tolerance." *International Conference*, The Welding Institute, London.

Whisler, D. (2013). "KU Research - Bridge Inspection Questions." A. M. Elmore, ed., Kansas Department of Transportation (KDOT).

Yu, L., Momeni, S., Godinez, V., and Giurgiutiu, V. "Adaptation of PWAS Transducers to Acoustic Emission Sensors." *Proc., Nondestructive Characterization for Composite Materials, Aerospace Engineering, Civil Infrastructure, and Homeland Security*, SPIE.

Zhang, Y. F. (2006). "In Situ Fatigue Crack Detection Using Piezoelectric Paint Sensor." *J Intel Mat Syst Str*, 17(10), 843-852.

APPENDIXES

APPENDIX A: MATERIAL PROPERTIES

A.1 Metric Units

Aluminum Alloy (from Boresi Text)

6061 T6

$\sigma_{ysAL} = 275.79 \cdot \mathrm{MPa}$ $\quad E_{AL} = 68.948 \cdot \mathrm{GPa}$ $\quad \rho_{AL} = 2.691 \times 10^{3} \cdot \frac{\mathrm{kg}}{\mathrm{m}^{3}}$

$\sigma_{ultAL} = 310.264 \cdot \mathrm{MPa}$ $\quad \nu_{AL} = 0.33$ $\quad \alpha_{AL} = 2.358 \times 10^{-5} \cdot \frac{1}{\Delta °\mathrm{C}}$ $\quad \%\mathrm{Elong}_{rup} = 12 \cdot \%$

Plexiglass (Grainger Material Info)

$\sigma_{ts} = 7.239 \times 10^{4} \cdot \mathrm{kPa}$ Tensile Strength

From Plexiglass Acrylic Plastic Sheets from Laird Plastics

$\sigma_{ts\_rup} = 7.239 \times 10^{4} \cdot \mathrm{kPa}$

$E_{PG} = 3.103 \cdot \mathrm{GPa}$

$\nu := 0.35$

Steel

$E_{s} = 199.948 \cdot \mathrm{GPa}$

ASTM A36

$\rho = 7.849 \times 10^{3} \cdot \frac{\mathrm{kg}}{\mathrm{m}^{3}}$ $\quad \sigma_{ys} = 248.211 \cdot \mathrm{MPa}$ $\quad \sigma_{ult} = 399.896 \cdot \mathrm{MPa}$

$\nu = 0.29$ $\quad \%\mathrm{Elong}_{rup} = 30 \cdot \%$ $\quad \alpha = 1.17 \times 10^{-5} \cdot \frac{1}{\Delta °\mathrm{C}}$

PZT

$E_{PZT} = 62.1 \cdot \mathrm{GPa}$

Bond Material

$E_{Bond} = 1.971 \cdot \mathrm{GPa}$

A.2 English Units

Aluminum Alloy (from Boresi Text)

6061 T6

$\sigma_{ysAL} := 40 \times 10^{3} psi$ $E_{AL} := 10.0 \times 10^{6} psi$ $\rho_{AL} := 168 \frac{lb}{ft^{3}} = 0.097 \cdot \frac{lb}{in^{3}}$

$\sigma_{ultAL} := 45 \times 10^{3} psi$ $\nu_{AL} := 0.33$ $\alpha_{AL} := 13.1 \times 10^{-6} \cdot \frac{1}{\Delta °F}$ $\%Elong_{rup} := 12\%$

Plexiglass (Grainger Material Info)

$\sigma_{ts} := 10500 \cdot psi$ Tensile Strength

From Plexiglass Acrylic Plastic Sheets from Laird Plastics

$\sigma_{ts\_rup} := 10500 psi$

$E_{PG} := 450000 psi$

$\nu := 0.35$

Steel

$E_{s} := 29 \times 10^{6} \cdot psi$

ASTM A36

$\rho := 490 \frac{lb}{ft^{3}} = 0.284 \cdot \frac{lb}{in^{3}}$ $\sigma_{ys} := 36 \times 10^{3} \cdot psi$ $\sigma_{ult} := 58 \times 10^{3} \cdot psi$

$\nu := 0.29$ $\%Elong_{rup} := 30\%$ $\alpha := 6.5 \times 10^{-6} \cdot \frac{1}{\Delta °F}$

PZT

$E_{PZT} := 0.9 \cdot E_{AL} = 9.007 \times 10^{6} psi$

Bond Material

$E_{Bond} := \frac{1}{35} \cdot E_{AL} = 2.859 \times 10^{5} psi$

APPENDIX B: GENERAL DESIGN AND MANUFACTURING PROCESS

B.1 General Design of Fabricated Aluminum Substrate H-Beam

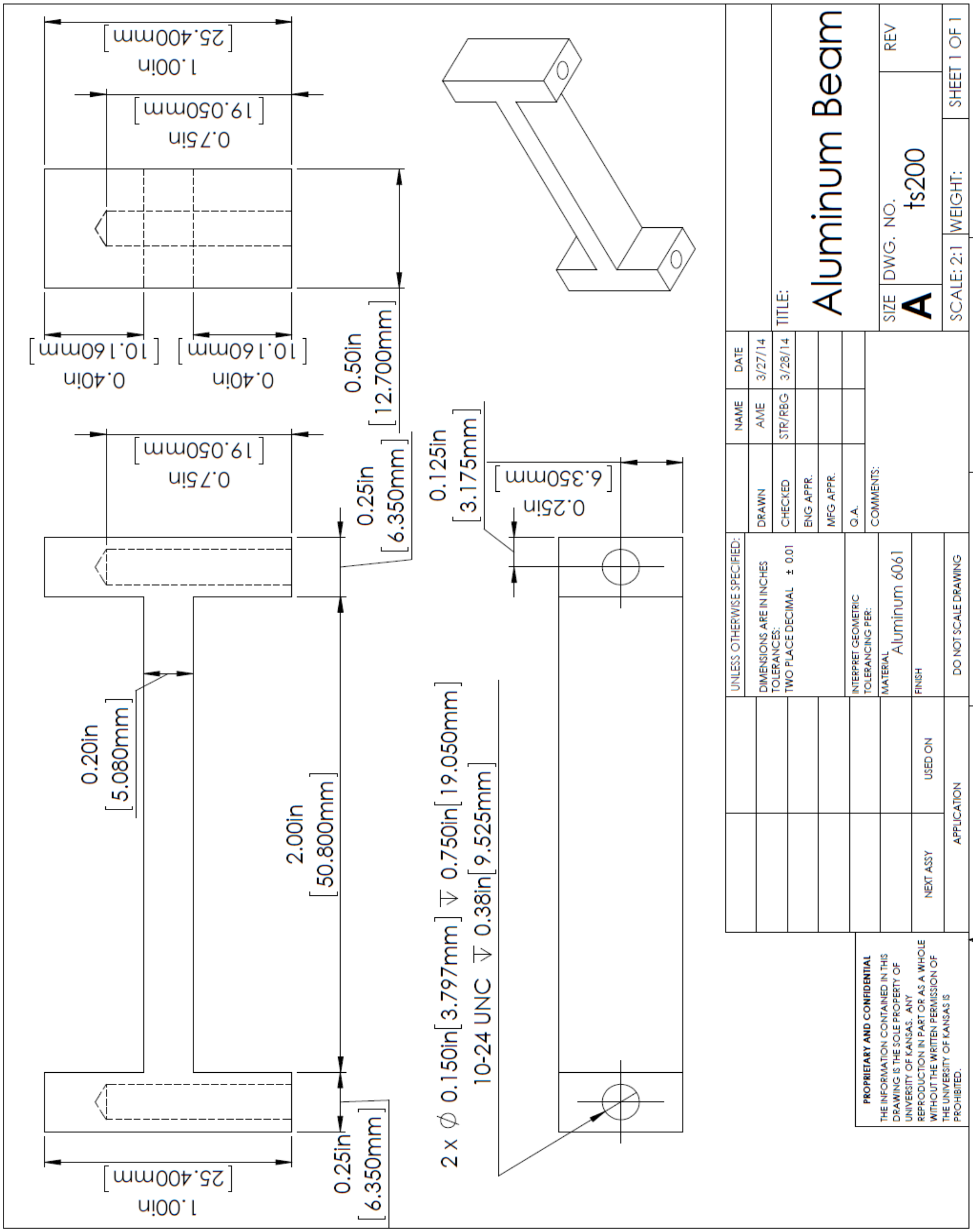

B.2 Manufacturing Procedure

Tools and Equipment

Piezoceramic Sheet of Desired Thickness
Aluminum Substrate (General H-frame geometry)
M4 x 0.7 (8-32) Steel Screws
Rotary Diamond Saw
Sand Paper (320-600 grit)
Conducting Epoxy (EP21TDC/N)
De-waxing and Cleaning Agents
Neodymium Magnet with 1 Countersunk Hole
Tix Solder
Soldering Iron
Variable Speed Lathe
Milling Machine

Fabrication Procedures

1. Substrate Preparation

   i. Mill the substrate H-beam web to the desired thickness.

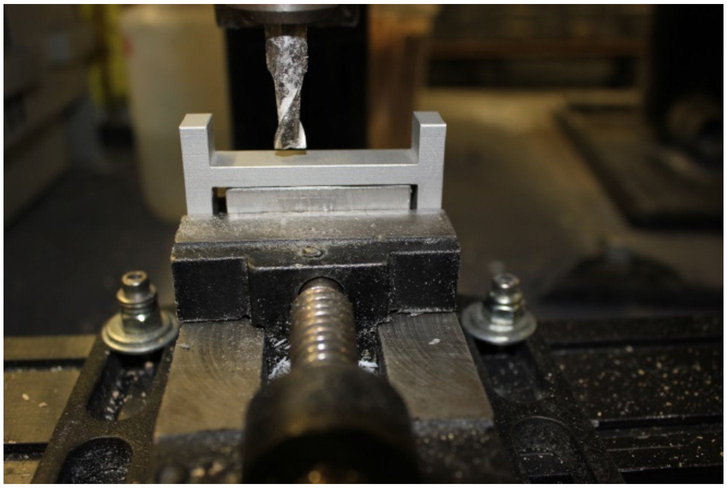

Figure B-1: General H-beam geometry in milling machine.

ii. Clean aluminum substrate with propanol and wet-sand to remove oxide layers.

2. Piezoelectric Element Preparation

   i. Mark the element to extend beyond the required substrate width.

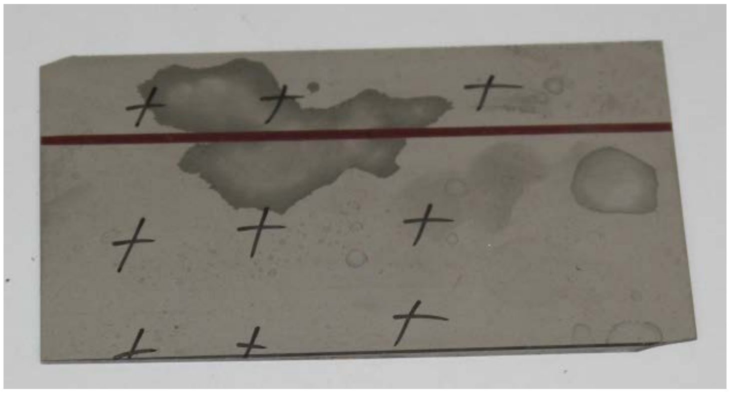

Figure B-2: Piezoceramic sheet

   ii. Cut the element using the rotary diamond saw under wet conditions to capture and remove potential dust and airborne lead hazards.

Figure B-3: Diamond saw used to cut the piezoceramic sheets.

iii. Wet sand the piezoceramic sheet using 320-600 grit sand paper to remove sputtered nickel facing.

Figure B-4: Piezoceramic sheet and 340 grit sand paper.

iv. Clean the element and remove all debris from both surfaces.

v. Determine and mark the poling direction of the PZT.

3. Resin Preparation

i. Select the resin to be used or EP21TDC/N.

ii. Mix the resin in proper proportions according to the manufacturers recommendations.

iii. Smear the mixed epoxy along the substrate web. Make sure the layer is very thin.

4. Substrate Mounting

    i. Mount the dry piezoceramic sheet to the epoxy coated side of the substrate web. Gently work the excess resin to the edges of the web.
    ii. Insert the unimorph into a vice, cover the piezoelectric mounted section, and apply a small weight to the surface in order to hold bonded parts in contact.
    iii. Let cure in accordance to the epoxy instructions.
    iv. Once cured, sand piezoelectric edge surfaces till smooth and flush with substrate web width.

5. Leg assembly

    i. Remove steel screw head and grind shaft tip using the variable speed lathe to fit magnet countersunk dimensions.

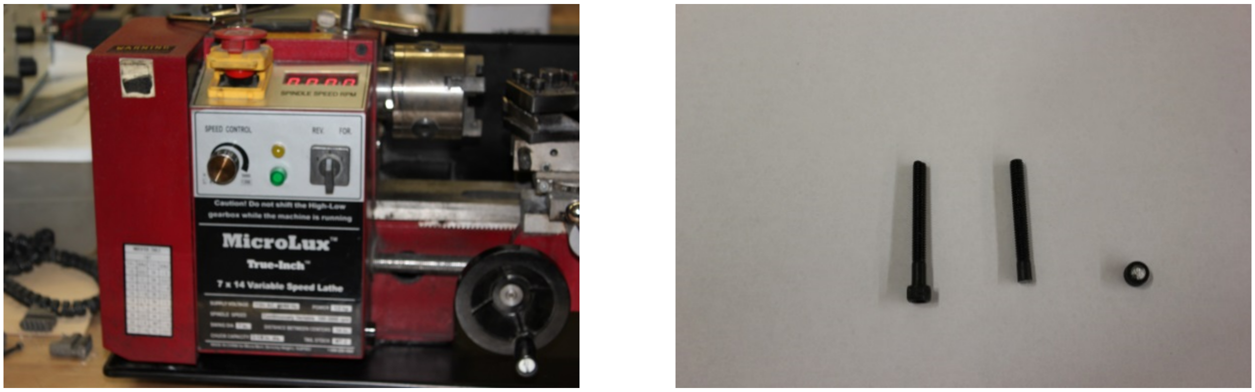

(a) (b)

Figure B-5: (a) Variable speed lathe used to remove the (b) steel screw head and sharpen the shaft tip.

ii. Clean the steel screw and mount to magnet using Hysol 9412.

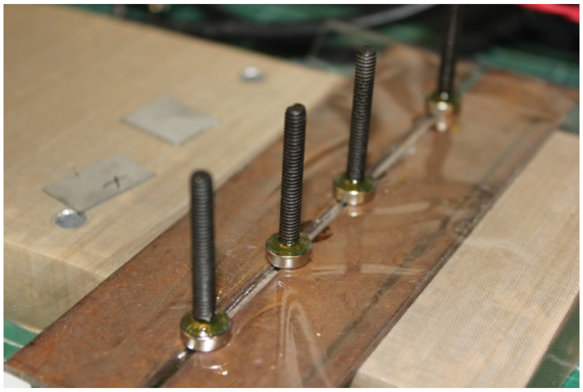

Figure B-6: Cleaned steel screw mounted to countersunk magnet.

iii. Let cure in accordance to manufacturers recommendations.

Figure B-7: PACTS tool leg assembly with sharpened steel screw and countersunk magnet.

6. PACTS tool assembly

   i. Anchor one lead mechanically and electrically to the ground of the H-frame.

   ii. Solder the second lead to the top of the piezoceramic sensor sheet using Tix solder.

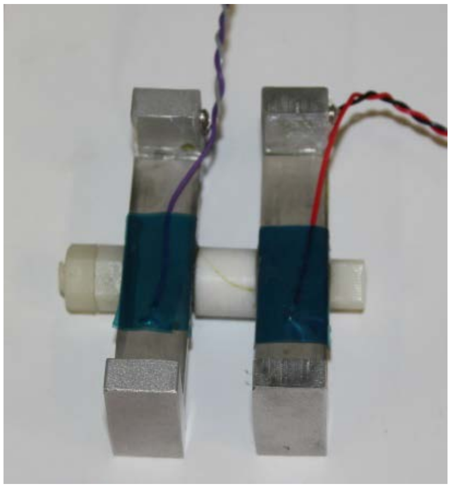

Figure B-8: Two PACTS tool composite members with leads grounded to the substrate frame and soldered to top of the piezoceramic sensor sheet.

iii. Route the two leads to the RC charge-sensor circuit and voltmeter.

7. PACTS tool Assembly

i. Insert steel legs into drilled and tapped substrate flange holes.

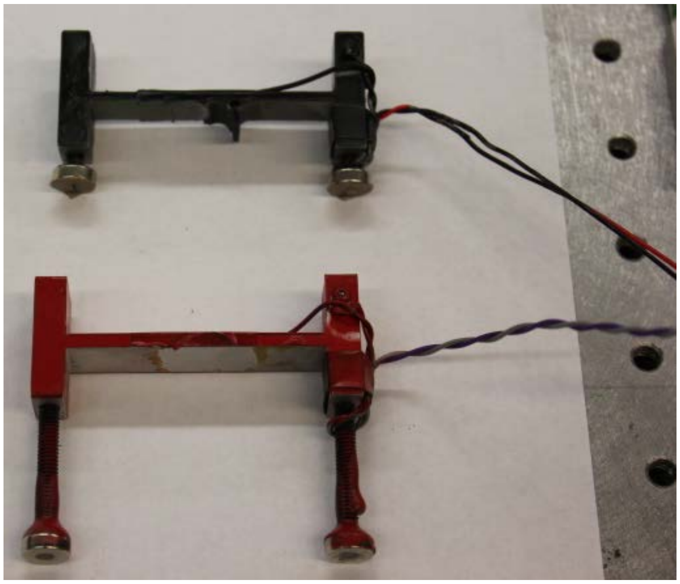

Figure B-9: Fabricated PACTS tools.

APPENDIX C: ABAQUS OPTIMIZATION

C.1 Results of Bond Thickness Variation on the PACTS Sensing Ability

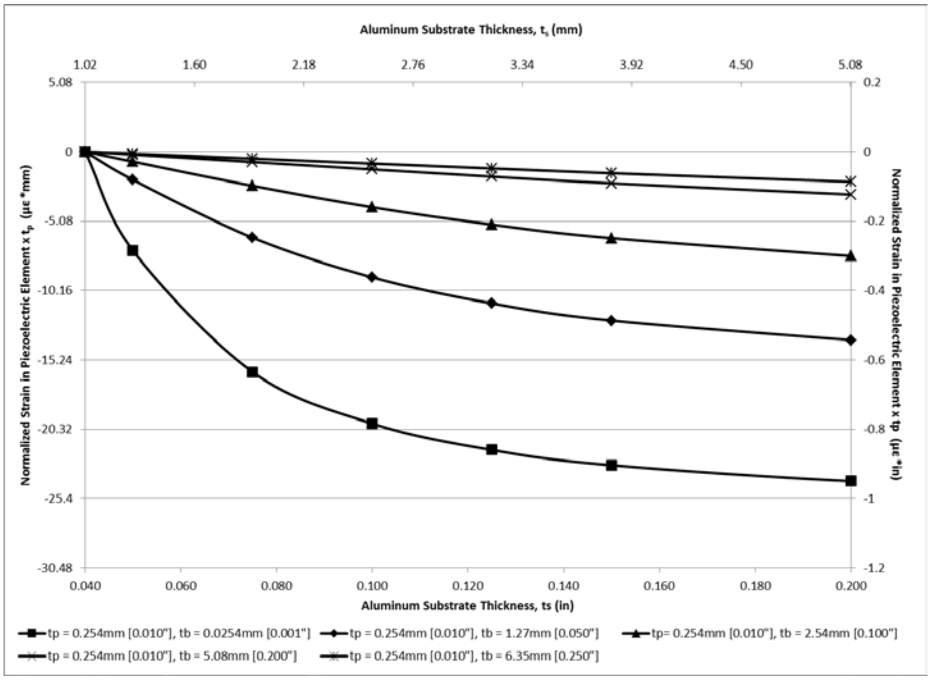

Figure C-1: FE model results of PACTS voltage sensitivity for a 0.254 mm [0.010 in] PZT layer thickness as a function of the aluminum thickness and bond thicknesses ranging from 0.0254 mm [0.001 in] ≤ t_b ≥ 6.350 mm [0.250 in].

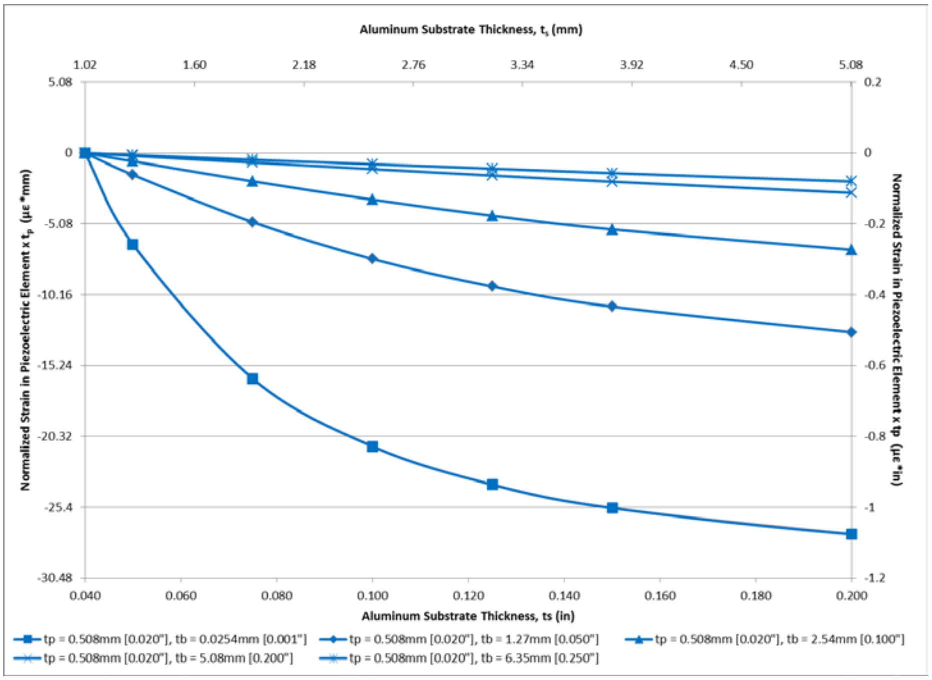

Figure C-2: FE model results of PACTS voltage sensitivity for a 0.508 mm [0.020 in] PZT layer thickness as a function of the aluminum thickness and bond thicknesses ranging from 0.0254 mm [0.001 in] ≤ t_b ≥ 6.35 mm [0.250 in].

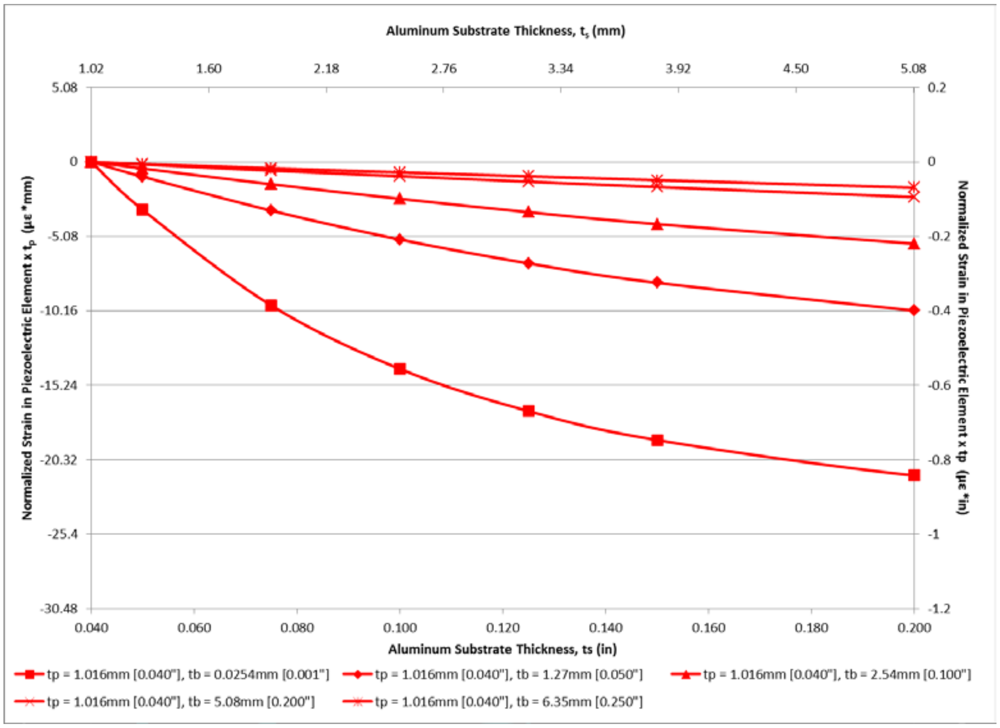

Figure C-3: FE model results of PACTS voltage sensitivity for a 1.016 mm [0.040 in] PZT layer thickness as a function of the aluminum thickness and bond thicknesses ranging from 0.0254 mm [0.001 in] ≤ t_b ≥ 6.35 mm [0.250 in].

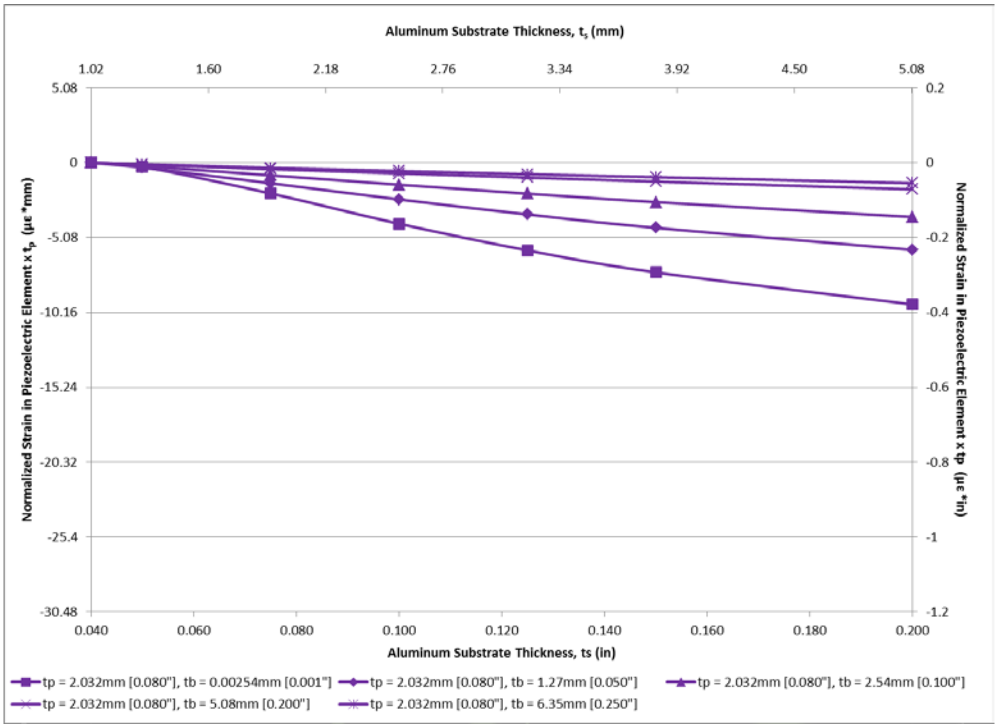

Figure C-4: FE model results of PACTS voltage sensitivity for a 2.032 mm [0.080 in] PZT layer thickness as a function of the aluminum thickness and bond thicknesses ranging from 0.0254 mm [0.001 in] ≤ t_b ≥ 6.35 mm [0.250 in].

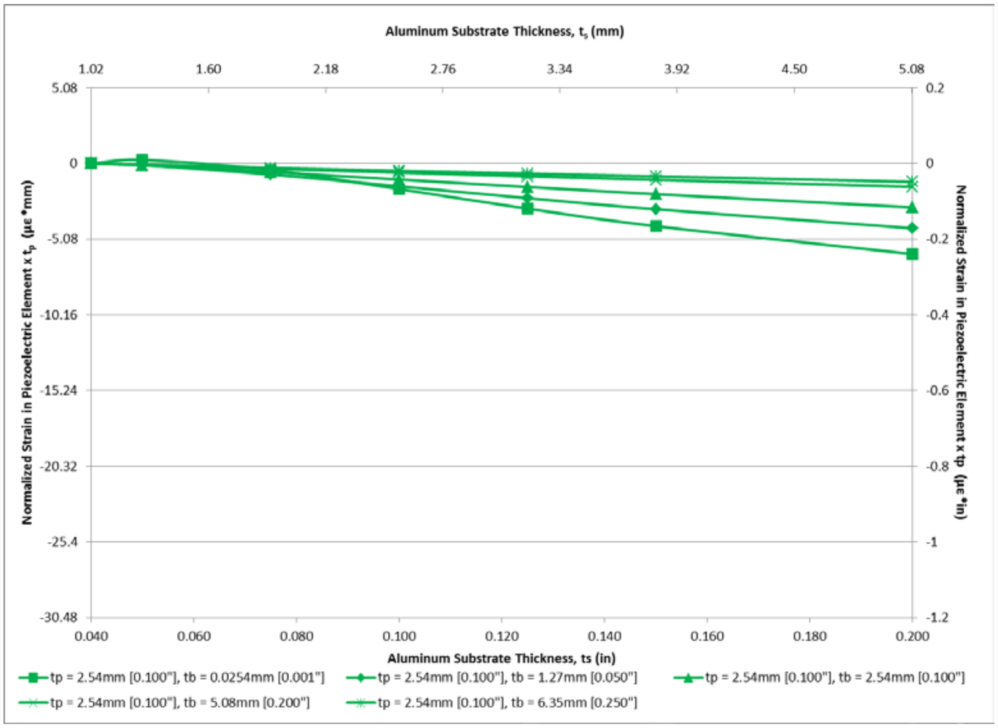

Figure C-5: FE model results of PACTS voltage sensitivity for a 2.540 mm [0.100 in] PZT layer thickness as a function of the aluminum thickness and bond thicknesses ranging from 0.0254 mm [0.001 in] ≤ t_b ≥ 6.35 mm [0.250 in].

C.2 Results of PZT Thickness Variation on the PACTS Sensing Ability

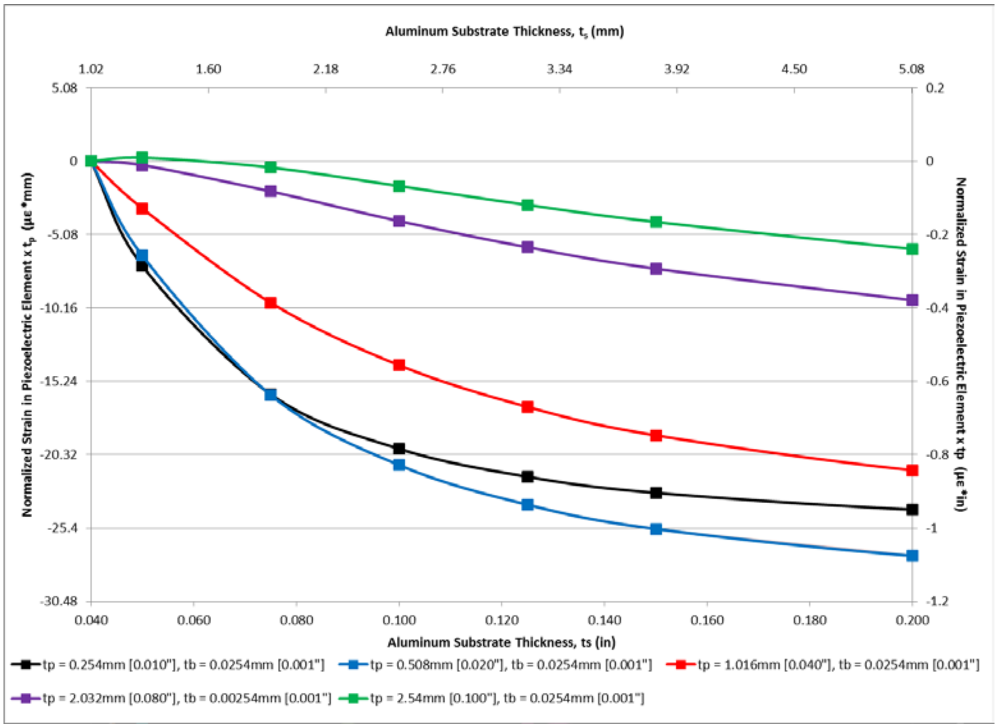

Figure C-6: FE model results of PACTS voltage sensitivity as a function of PZT layer thicknesses and aluminum substrate thickness using a constant 0.0254 mm [0.001 in] bond layer thickness.

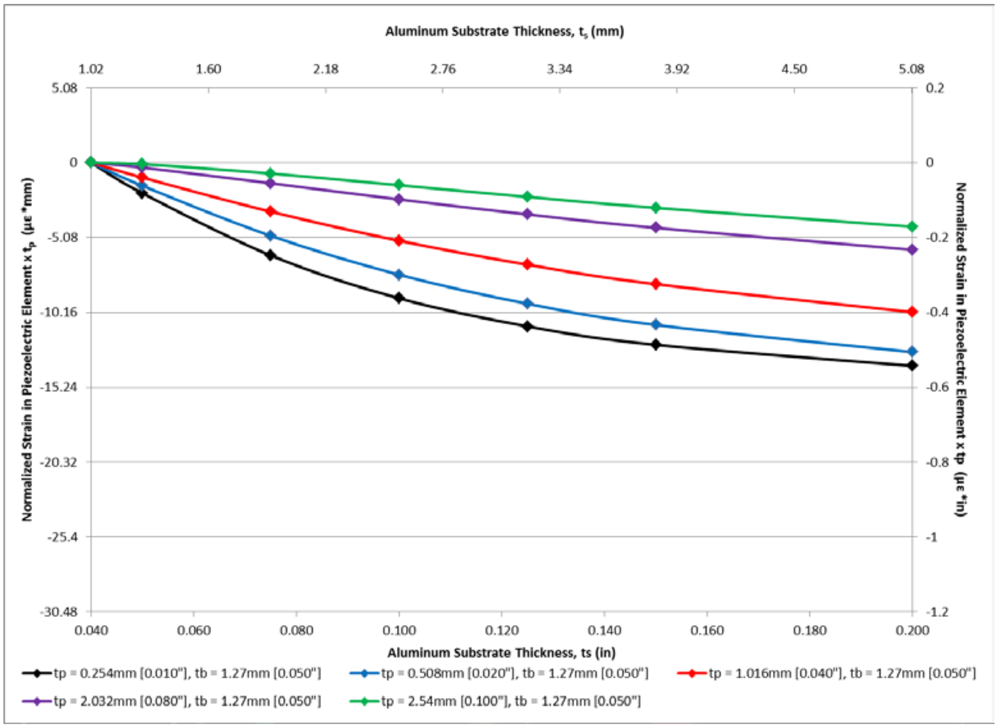

Figure C-7: FE model results of PACTS voltage sensitivity as a function of PZT layer thicknesses and aluminum substrate thickness using a constant 1.270 mm [0.050 in] bond layer thickness.

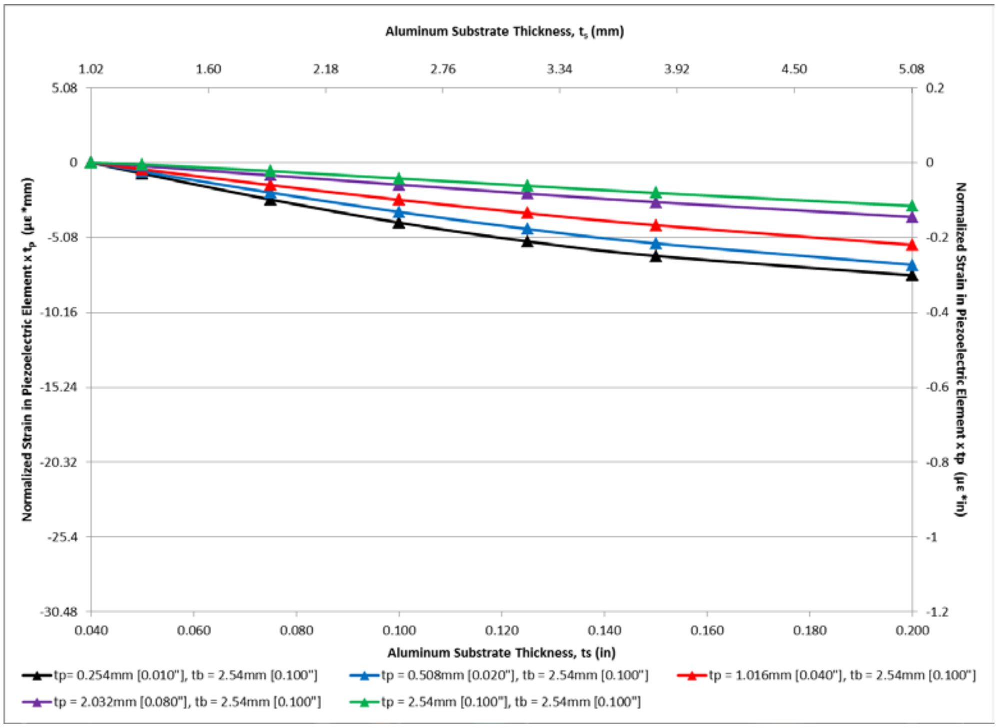

Figure C-8: FE model results of PACTS voltage sensitivity as a function of PZT layer thicknesses and aluminum substrate thickness using a constant 2.540 mm [0.100 in] bond layer thickness.

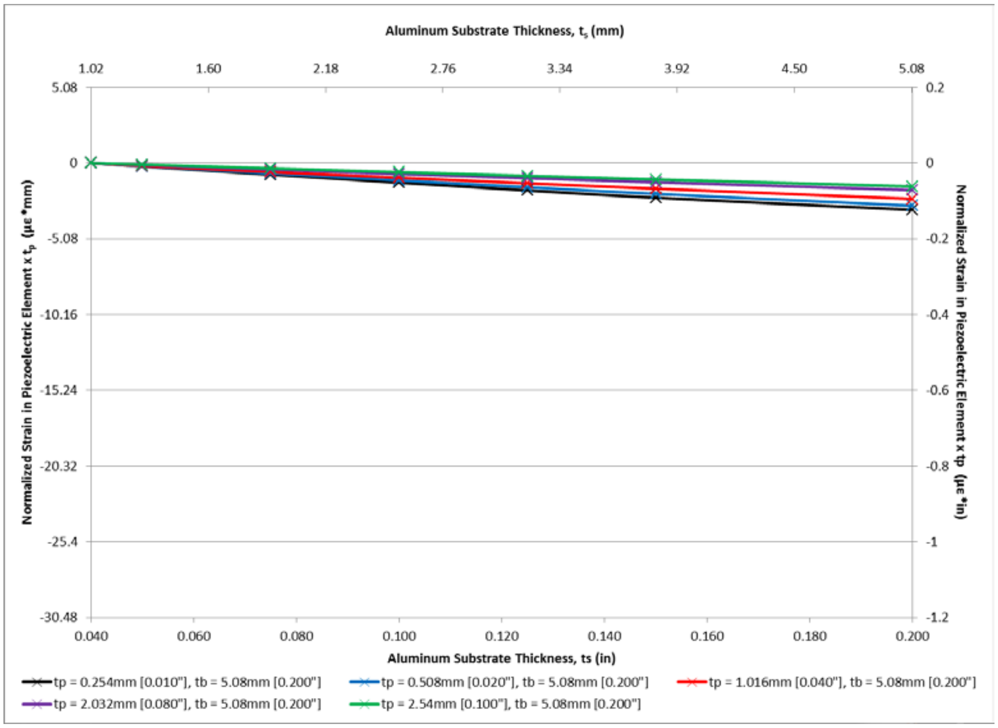

Figure C-9: FE model results of PACTS voltage sensitivity as a function of PZT layer thicknesses and aluminum substrate thickness using a constant 5.080 mm [0.200 in] bond layer thickness.

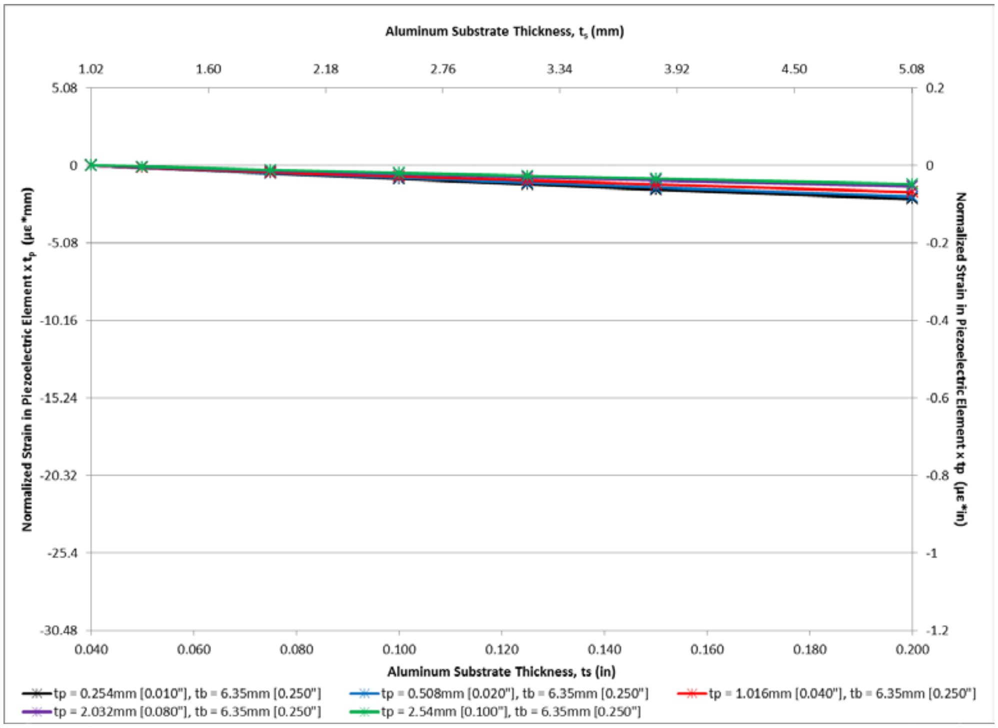

Figure C-10: FE model results of PACTS voltage sensitivity as a function of PZT layer thicknesses and aluminum substrate thickness using a constant 6.350 mm [0.250 in] bond layer thickness.

C.3 Finite Element Model Data and Calculated Sensing Voltage

Table C-1: FE model PACTS tool PZT layer mid-plane strain results and voltage sensitivity calculations as a function of substrate and bond thicknesses using a constant 0.254 mm [0.010 in] PZT layer thickness.

Model	t_s		t_b		με	ε x t_p	
	in	mm	in	mm	normalized	με*in	με*mm
ts40_tb1_tp10	0.040	1.016	0.001	0.0254	0.0	0	0
ts50_tb1_tp10	0.050	1.270	0.001	0.0254	-28.5	-0.285	-7.239
ts75_tb1_tp10	0.075	1.905	0.001	0.0254	-63.5	-0.635	-16.132
ts100_tb1_tp10	0.100	2.540	0.001	0.0254	-78.4	-0.784	-19.905
ts125_tb1_tp10	0.125	3.175	0.001	0.0254	-86.0	-0.860	-21.835
ts150_tb1_tp10	0.150	3.810	0.001	0.0254	-90.3	-0.903	-22.948
ts200_tb1_tp10	0.200	5.080	0.001	0.0254	-94.9	-0.949	-24.112
ts40_tb50_tp10	0.040	1.016	0.05	1.27	0.0	0	0
ts50_tb50_tp10	0.050	1.270	0.05	1.27	-8.1	-0.081	-2.063
ts75_tb50_tp10	0.075	1.905	0.05	1.27	-24.8	-0.248	-6.296
ts100_tb50_tp10	0.100	2.540	0.05	1.27	-36.2	-0.362	-9.200
ts125_tb50_tp10	0.125	3.175	0.05	1.27	-43.7	-0.437	-11.106
ts150_tb50_tp10	0.150	3.810	0.05	1.27	-48.7	-0.487	-12.361
ts200_tb50_tp10	0.200	5.080	0.050	1.27	-54.3	-0.543	-13.791
ts40_tb100_tp10	0.040	1.016	0.100	2.54	0.0	0	0
ts50_tb100_tp10	0.050	1.270	0.100	2.54	-2.9	-0.029	-0.732
ts75_tb100_tp10	0.075	1.905	0.100	2.54	-9.8	-0.098	-2.501
ts100_tb100_tp10	0.100	2.540	0.100	2.54	-16.0	-0.160	-4.067
ts125_tb100_tp10	0.125	3.175	0.100	2.54	-21.0	-0.210	-5.342
ts150_tb100_tp10	0.150	3.810	0.100	2.54	-24.9	-0.249	-6.328
ts200_tb100_tp10	0.200	5.080	0.100	2.54	-30.1	-0.301	-7.636
ts40_tb200_tp10	0.040	1.016	0.200	5.08	0.0	0	0
ts50_tb200_tp10	0.050	1.270	0.200	5.08	-0.9	-0.009	-0.222
ts75_tb200_tp10	0.075	1.905	0.200	5.08	-3.0	-0.030	-0.761
ts100_tb200_tp10	0.100	2.540	0.200	5.08	-5.1	-0.051	-1.301
ts125_tb200_tp10	0.125	3.175	0.200	5.08	-7.2	-0.072	-1.826
ts150_tb200_tp10	0.150	3.810	0.200	5.08	-9.1	-0.091	-2.315
ts200_tb200_tp10	0.200	5.080	0.200	5.08	-12.3	-0.123	-3.132
ts40_tb250_tp10	0.040	1.016	0.250	6.35	0.0	0	0
ts50_tb250_tp10	0.050	1.270	0.250	6.35	-0.6	-0.006	-0.155
ts75_tb250_tp10	0.075	1.905	0.250	6.35	-2.0	-0.020	-0.516
ts100_tb250_tp10	0.100	2.540	0.250	6.35	-3.4	-0.034	-0.874
ts125_tb250_tp10	0.125	3.175	0.250	6.35	-4.8	-0.048	-1.232
ts150_tb250_tp10	0.150	3.810	0.250	6.35	-6.2	-0.062	-1.579
ts200_tb250_tp10	0.200	5.080	0.250	6.35	-8.7	-0.087	-2.204

Table C-2: FE model PACTS tool PZT layer mid-plane strain results and voltage sensitivity calculations as a function of substrate and bond thicknesses using a constant 0.508 mm [0.020 in] PZT layer thickness.

Model	t_s		t_b		με	ε x t_p	
	in	mm	in	mm	normalized	με*in	με*mm
ts40_tb1_tp20	0.040	1.016	0.001	0.025	0	0	0
ts50_tb1_tp20	0.050	1.270	0.001	0.025	-12.87	-0.257	-6.536
ts75_tb1_tp20	0.075	1.905	0.001	0.025	-31.85	-0.637	-16.178
ts100_tb1_tp20	0.100	2.540	0.001	0.025	-41.40	-0.828	-21.033
ts125_tb1_tp20	0.125	3.175	0.001	0.025	-46.79	-0.936	-23.770
ts150_tb1_tp20	0.150	3.810	0.001	0.025	-50.10	-1.002	-25.452
ts200_tb1_tp20	0.200	5.080	0.001	0.025	-53.77	-1.075	-27.314
ts40_tb50_tp20	0.040	1.016	0.05	1.270	0	0	0
ts50_tb50_tp20	0.050	1.270	0.05	1.270	-3.07	-0.061	-1.560
ts75_tb50_tp20	0.075	1.905	0.05	1.270	-9.77	-0.195	-4.961
ts100_tb50_tp20	0.100	2.540	0.05	1.270	-14.97	-0.299	-7.602
ts125_tb50_tp20	0.125	3.175	0.05	1.270	-18.83	-0.377	-9.568
ts150_tb50_tp20	0.150	3.810	0.05	1.270	-21.67	-0.433	-11.010
ts200_tb50_tp20	0.200	5.080	0.050	1.270	-25.31	-0.506	-12.855
ts40_tb100_tp20	0.040	1.016	0.100	2.540	0	0	0
ts50_tb100_tp20	0.050	1.270	0.100	2.540	-1.18	-0.024	-0.597
ts75_tb100_tp20	0.075	1.905	0.100	2.540	-3.99	-0.080	-2.028
ts100_tb100_tp20	0.100	2.540	0.100	2.540	-6.58	-0.132	-3.343
ts125_tb100_tp20	0.125	3.175	0.100	2.540	-8.86	-0.177	-4.499
ts150_tb100_tp20	0.150	3.810	0.100	2.540	-10.78	-0.216	-5.476
ts200_tb100_tp20	0.200	5.080	0.100	2.540	-13.65	-0.273	-6.935
ts40_tb200_tp20	0.040	1.016	0.200	5.080	0	0	0
ts50_tb200_tp20	0.050	1.270	0.200	5.080	-0.40	-0.008	-0.205
ts75_tb200_tp20	0.075	1.905	0.200	5.080	-1.35	-0.027	-0.686
ts100_tb200_tp20	0.100	2.540	0.200	5.080	-2.27	-0.045	-1.153
ts125_tb200_tp20	0.125	3.175	0.200	5.080	-3.17	-0.063	-1.612
ts150_tb200_tp20	0.150	3.810	0.200	5.080	-4.05	-0.081	-2.056
ts200_tb200_tp20	0.200	5.080	0.200	5.080	-5.62	-0.112	-2.857
ts40_tb250_tp20	0.040	1.016	0.250	6.350	0	0	0
ts50_tb250_tp20	0.050	1.270	0.250	6.350	-0.30	-0.006	-0.150
ts75_tb250_tp20	0.075	1.905	0.250	6.350	-0.96	-0.019	-0.487
ts100_tb250_tp20	0.100	2.540	0.250	6.350	-1.59	-0.032	-0.808
ts125_tb250_tp20	0.125	3.175	0.250	6.350	-2.22	-0.044	-1.126
ts150_tb250_tp20	0.150	3.810	0.250	6.350	-2.84	-0.057	-1.442
ts200_tb250_tp20	0.200	5.080	0.250	6.350	-4.02	-0.080	-2.043

Table C-3: FE model PACTS tool PZT layer mid-plane strain results and voltage sensitivity calculations as a function of substrate and bond thicknesses using a constant 1.016 mm [0.040 in] PZT layer thickness.

Model	t_s		t_b		με	ε x t_p	
	in	mm	in	mm	normalized	με*in	με*mm
ts40_tb1_tp40	0.040	1.016	0.001	0.0254	0	0	0
ts50_tb1_tp40	0.050	1.270	0.001	0.0254	-3.2	-0.128	-3.261
ts75_tb1_tp40	0.075	1.905	0.001	0.0254	-9.6	-0.386	-9.792
ts100_tb1_tp40	0.100	2.540	0.001	0.0254	-13.9	-0.556	-14.122
ts125_tb1_tp40	0.125	3.175	0.001	0.0254	-16.7	-0.669	-16.999
ts150_tb1_tp40	0.150	3.810	0.001	0.0254	-18.7	-0.747	-18.971
ts200_tb1_tp40	0.200	5.080	0.001	0.0254	-21.1	-0.842	-21.393
ts40_tb50_tp40	0.040	1.016	0.05	1.27	0	0	0
ts50_tb50_tp40	0.050	1.270	0.05	1.27	-1.0	-0.039	-1.002
ts75_tb50_tp40	0.075	1.905	0.05	1.27	-3.3	-0.131	-3.320
ts100_tb50_tp40	0.100	2.540	0.05	1.27	-5.2	-0.208	-5.295
ts125_tb50_tp40	0.125	3.175	0.05	1.27	-6.8	-0.273	-6.922
ts150_tb50_tp40	0.150	3.810	0.05	1.27	-8.1	-0.324	-8.237
ts200_tb50_tp40	0.200	5.080	0.050	1.27	-10.0	-0.399	-10.142
ts40_tb100_tp40	0.040	1.016	0.100	2.54	0	0	0
ts50_tb100_tp40	0.050	1.270	0.100	2.54	-0.4	-0.018	-0.449
ts75_tb100_tp40	0.075	1.905	0.100	2.54	-1.5	-0.060	-1.518
ts100_tb100_tp40	0.100	2.540	0.100	2.54	-2.5	-0.099	-2.514
ts125_tb100_tp40	0.125	3.175	0.100	2.54	-3.4	-0.135	-3.424
ts150_tb100_tp40	0.150	3.810	0.100	2.54	-4.2	-0.167	-4.239
ts200_tb100_tp40	0.200	5.080	0.100	2.54	-5.5	-0.220	-5.580
ts40_tb200_tp40	0.040	1.016	0.200	5.08	0	0	0
ts50_tb200_tp40	0.050	1.270	0.200	5.08	-0.2	-0.007	-0.180
ts75_tb200_tp40	0.075	1.905	0.200	5.08	-0.6	-0.023	-0.589
ts100_tb200_tp40	0.100	2.540	0.200	5.08	-1.0	-0.038	-0.973
ts125_tb200_tp40	0.125	3.175	0.200	5.08	-1.3	-0.053	-1.346
ts150_tb200_tp40	0.150	3.810	0.200	5.08	-1.7	-0.067	-1.709
ts200_tb200_tp40	0.200	5.080	0.200	5.08	-2.4	-0.094	-2.396
ts40_tb250_tp40	0.040	1.016	0.250	6.35	0	0	0
ts50_tb250_tp40	0.050	1.270	0.250	6.35	-0.1	-0.005	-0.138
ts75_tb250_tp40	0.075	1.905	0.250	6.35	-0.4	-0.017	-0.438
ts100_tb250_tp40	0.100	2.540	0.250	6.35	-0.7	-0.028	-0.712
ts125_tb250_tp40	0.125	3.175	0.250	6.35	-1.0	-0.038	-0.978
ts150_tb250_tp40	0.150	3.810	0.250	6.35	-1.2	-0.049	-1.240
ts200_tb250_tp40	0.200	5.080	0.250	6.35	-1.7	-0.069	-1.755

Table C-4: FE model PACTS tool PZT layer mid-plane strain results and voltage sensitivity calculations as a function of substrate and bond thicknesses using a constant 2.032 mm [0.080 in] PZT layer thickness.

Model	t_s		t_b		με	ε x t_p	
	in	mm	in	mm	normalized	με*in	με*mm
ts40_tb1_tp80	0.040	1.016	0.001	0.025	0	0	0
ts50_tb1_tp80	0.050	1.270	0.001	0.025	-0.134	-0.011	-0.271
ts75_tb1_tp80	0.075	1.905	0.001	0.025	-1.025	-0.082	-2.082
ts100_tb1_tp80	0.100	2.540	0.001	0.025	-2.038	-0.163	-4.142
ts125_tb1_tp80	0.125	3.175	0.001	0.025	-2.928	-0.234	-5.950
ts150_tb1_tp80	0.150	3.810	0.001	0.025	-3.661	-0.293	-7.439
ts200_tb1_tp80	0.200	5.080	0.001	0.025	-4.733	-0.379	-9.618
ts40_tb50_tp80	0.040	1.016	0.05	1.270	0	0	0
ts50_tb50_tp80	0.050	1.270	0.05	1.270	-0.163	-0.013	-0.332
ts75_tb50_tp80	0.075	1.905	0.05	1.270	-0.684	-0.055	-1.390
ts100_tb50_tp80	0.100	2.540	0.05	1.270	-1.224	-0.098	-2.488
ts125_tb50_tp80	0.125	3.175	0.05	1.270	-1.726	-0.138	-3.508
ts150_tb50_tp80	0.150	3.810	0.05	1.270	-2.175	-0.174	-4.419
ts200_tb50_tp80	0.200	5.080	0.050	1.270	-2.911	-0.233	-5.915
ts40_tb100_tp80	0.040	1.016	0.100	2.540	0	0	0
ts50_tb100_tp80	0.050	1.270	0.100	2.540	-0.112	-0.009	-0.227
ts75_tb100_tp80	0.075	1.905	0.100	2.540	-0.420	-0.034	-0.853
ts100_tb100_tp80	0.100	2.540	0.100	2.540	-0.732	-0.059	-1.487
ts125_tb100_tp80	0.125	3.175	0.100	2.540	-1.031	-0.083	-2.096
ts150_tb100_tp80	0.150	3.810	0.100	2.540	-1.313	-0.105	-2.668
ts200_tb100_tp80	0.200	5.080	0.100	2.540	-1.813	-0.145	-3.684
ts40_tb200_tp80	0.040	1.016	0.200	5.080	0	0	0
ts50_tb200_tp80	0.050	1.270	0.200	5.080	-0.064	-0.005	-0.130
ts75_tb200_tp80	0.075	1.905	0.200	5.080	-0.214	-0.017	-0.434
ts100_tb200_tp80	0.100	2.540	0.200	5.080	-0.356	-0.028	-0.724
ts125_tb200_tp80	0.125	3.175	0.200	5.080	-0.494	-0.040	-1.004
ts150_tb200_tp80	0.150	3.810	0.200	5.080	-0.628	-0.050	-1.276
ts200_tb200_tp80	0.200	5.080	0.200	5.080	-0.888	-0.071	-1.805
ts40_tb250_tp80	0.040	1.016	0.250	6.350	0	0	0
ts50_tb250_tp80	0.050	1.270	0.250	6.350	-0.054	-0.004	-0.109
ts75_tb250_tp80	0.075	1.905	0.250	6.350	-0.172	-0.014	-0.349
ts100_tb250_tp80	0.100	2.540	0.250	6.350	-0.279	-0.022	-0.567
ts125_tb250_tp80	0.125	3.175	0.250	6.350	-0.381	-0.031	-0.775
ts150_tb250_tp80	0.150	3.810	0.250	6.350	-0.481	-0.038	-0.977
ts200_tb250_tp80	0.200	5.080	0.250	6.350	-0.680	-0.054	-1.381

Table C-5: FE model PACTS tool PZT layer mid-plane strain results and voltage sensitivity calculations as a function of substrate and bond thicknesses using a constant 2.540 mm [0.100 in] PZT layer thickness.

Model	t_s		t_b		με	ε x t_p	
	in	mm	in	mm	normalized	με*in	με*mm
ts40_tb1_tp100	0.040	1.016	0.001	0.025	0	0	0
ts50_tb1_tp100	0.050	1.270	0.001	0.025	0.095	0.010	0.242
ts75_tb1_tp100	0.075	1.905	0.001	0.025	-0.170	-0.017	-0.432
ts100_tb1_tp100	0.100	2.540	0.001	0.025	-0.674	-0.067	-1.711
ts125_tb1_tp100	0.125	3.175	0.001	0.025	-1.190	-0.119	-3.022
ts150_tb1_tp100	0.150	3.810	0.001	0.025	-1.654	-0.165	-4.201
ts200_tb1_tp100	0.200	5.080	0.001	0.025	-2.392	-0.239	-6.075
ts40_tb50_tp100	0.040	1.016	0.05	1.270	0	0	0
ts50_tb50_tp100	0.050	1.270	0.05	1.270	-0.040	-0.004	-0.102
ts75_tb50_tp100	0.075	1.905	0.05	1.270	-0.288	-0.029	-0.731
ts100_tb50_tp100	0.100	2.540	0.05	1.270	-0.600	-0.060	-1.523
ts125_tb50_tp100	0.125	3.175	0.05	1.270	-0.912	-0.091	-2.317
ts150_tb50_tp100	0.150	3.810	0.05	1.270	-1.205	-0.121	-3.061
ts200_tb50_tp100	0.200	5.080	0.050	1.270	-1.710	-0.171	-4.342
ts40_tb100_tp100	0.040	1.016	0.100	2.540	0	0	0
ts50_tb100_tp100	0.050	1.270	0.100	2.540	-0.050	-0.005	-0.126
ts75_tb100_tp100	0.075	1.905	0.100	2.540	-0.224	-0.022	-0.569
ts100_tb100_tp100	0.100	2.540	0.100	2.540	-0.420	-0.042	-1.068
ts125_tb100_tp100	0.125	3.175	0.100	2.540	-0.617	-0.062	-1.568
ts150_tb100_tp100	0.150	3.810	0.100	2.540	-0.807	-0.081	-2.050
ts200_tb100_tp100	0.200	5.080	0.100	2.540	-1.154	-0.115	-2.932
ts40_tb200_tp100	0.040	1.016	0.200	5.080	0	0	0
ts50_tb200_tp100	0.050	1.270	0.200	5.080	-0.039	-0.004	-0.100
ts75_tb200_tp100	0.075	1.905	0.200	5.080	-0.139	-0.014	-0.352
ts100_tb200_tp100	0.100	2.540	0.200	5.080	-0.237	-0.024	-0.603
ts125_tb200_tp100	0.125	3.175	0.200	5.080	-0.334	-0.033	-0.848
ts150_tb200_tp100	0.150	3.810	0.200	5.080	-0.428	-0.043	-1.088
ts200_tb200_tp100	0.200	5.080	0.200	5.080	-0.614	-0.061	-1.559
ts40_tb250_tp100	0.040	1.016	0.250	6.350	0	0	0
ts50_tb250_tp100	0.050	1.270	0.250	6.350	-0.026	-0.003	-0.066
ts75_tb250_tp100	0.075	1.905	0.250	6.350	-0.117	-0.012	-0.298
ts100_tb250_tp100	0.100	2.540	0.250	6.350	-0.194	-0.019	-0.492
ts125_tb250_tp100	0.125	3.175	0.250	6.350	-0.267	-0.027	-0.677
ts150_tb250_tp100	0.150	3.810	0.250	6.350	-0.338	-0.034	-0.858
ts200_tb250_tp100	0.200	5.080	0.250	6.350	-0.481	-0.048	-1.221

C.4 Selected Geometry

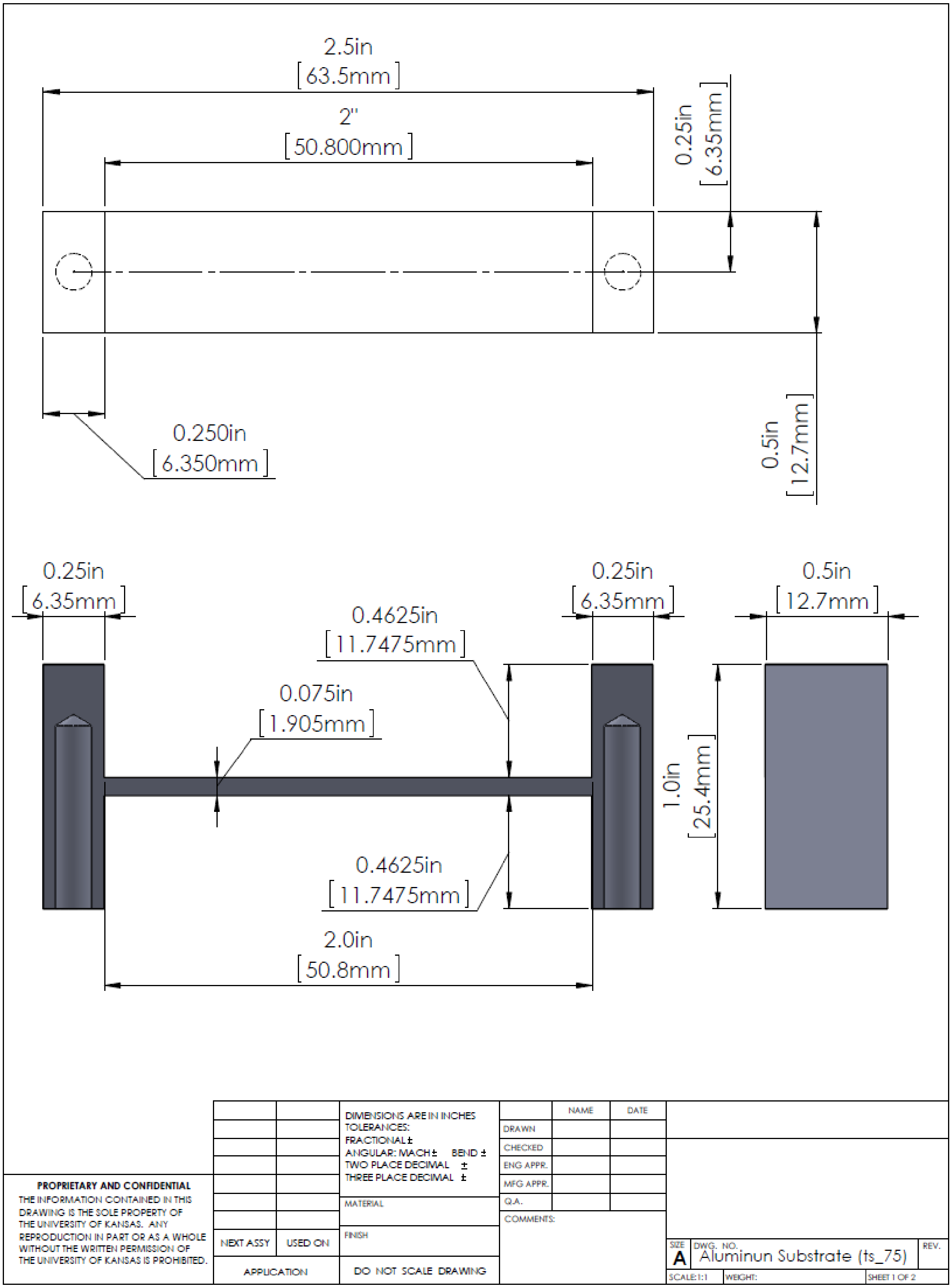

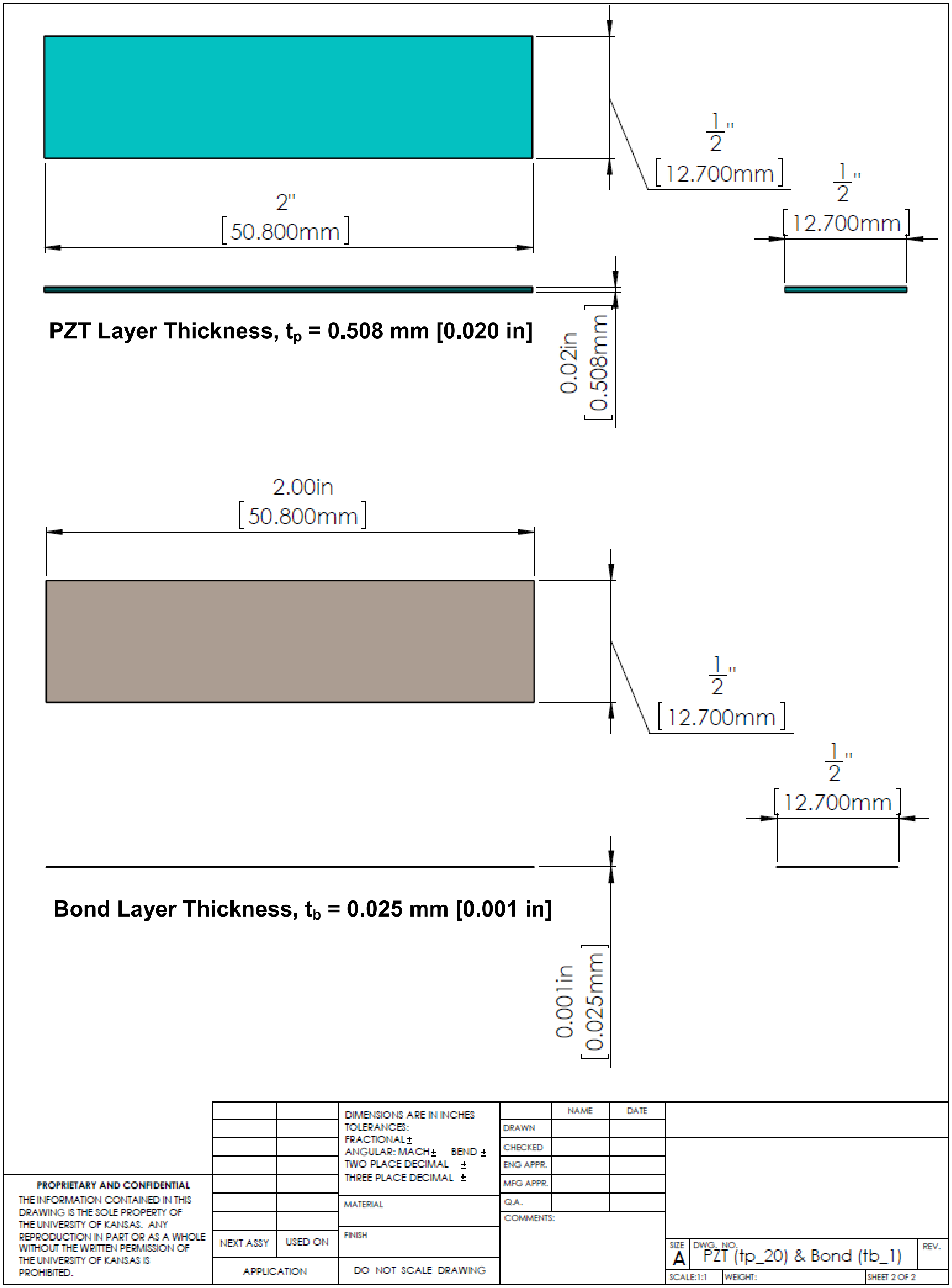

PZT Layer Thickness, t_p = 0.508 mm [0.020 in]

Bond Layer Thickness, t_b = 0.025 mm [0.001 in]

DIMENSIONS ARE IN INCHES
TOLERANCES:
FRACTIONAL ±
ANGULAR: MACH ± BEND ±
TWO PLACE DECIMAL ±
THREE PLACE DECIMAL ±

MATERIAL

FINISH

DO NOT SCALE DRAWING

NEXT ASSY | USED ON

APPLICATION

	NAME	DATE
DRAWN		
CHECKED		
ENG APPR.		
MFG APPR.		
Q.A.		

COMMENTS:

SIZE A
DWG. NO. PZT (tp_20) & Bond (tb_1)
REV.
SCALE:1:1
WEIGHT:
SHEET 2 OF 2

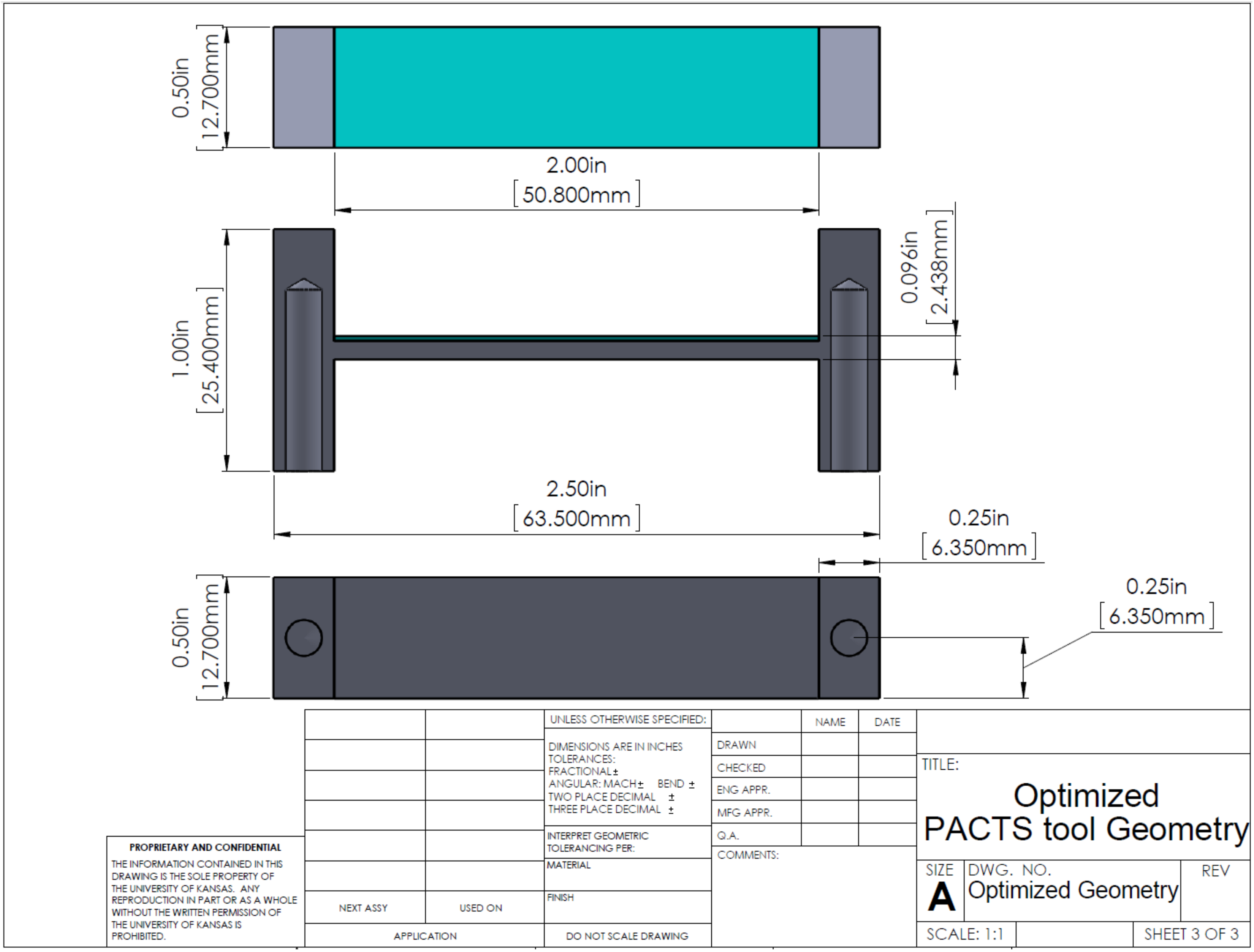
0.50in
[12.700mm]
2.00in
[50.800mm]
1.00in
[25.400mm]
0.096in
[2.438mm]
2.50in
[63.500mm]
0.25in
[6.350mm]
0.50in
[12.700mm]
0.25in
[6.350mm]
PROPRIETARY AND CONFIDENTIAL
THE INFORMATION CONTAINED IN THIS DRAWING IS THE SOLE PROPERTY OF THE UNIVERSITY OF KANSAS. ANY REPRODUCTION IN PART OR AS A WHOLE WITHOUT THE WRITTEN PERMISSION OF THE UNIVERSITY OF KANSAS IS PROHIBITED.
NEXT ASSY
USED ON
APPLICATION
UNLESS OTHERWISE SPECIFIED:
DIMENSIONS ARE IN INCHES
TOLERANCES:
FRACTIONAL±
ANGULAR: MACH± BEND ±
TWO PLACE DECIMAL ±
THREE PLACE DECIMAL ±
INTERPRET GEOMETRIC TOLERANCING PER:
MATERIAL
FINISH
DO NOT SCALE DRAWING
NAME
DATE
DRAWN
CHECKED
ENG APPR.
MFG APPR.
Q.A.
COMMENTS:
TITLE:
Optimized
PACTS tool Geometry
SIZE
A
DWG. NO.
Optimized Geometry
REV
SCALE: 1:1
SHEET 3 OF 3

APPENDIX D: ARTIFICIAL CRACK SYSTEM

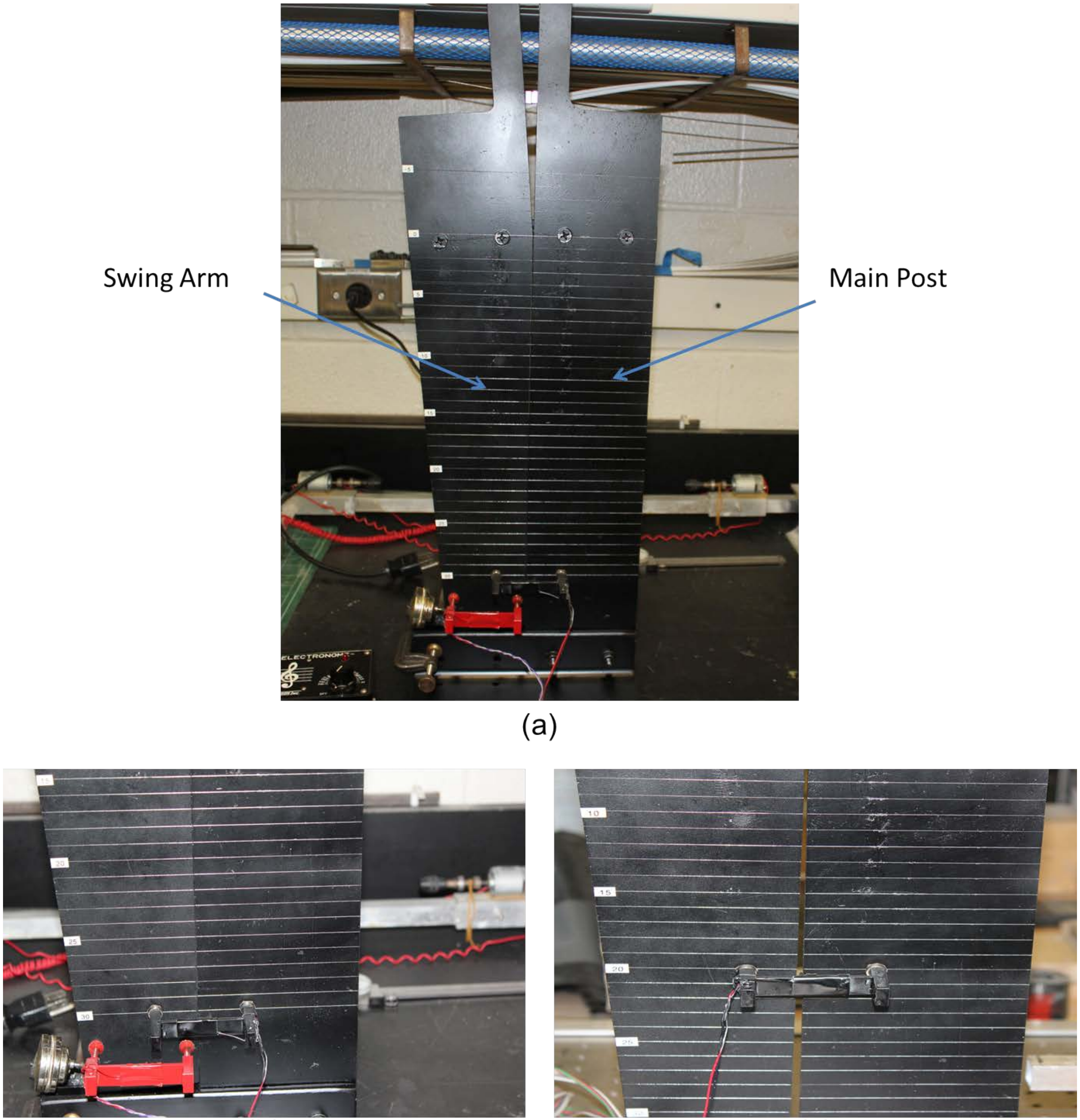

(a)

(b)

(c)

Figure D-1: (a) Artificial Crack System and close up of (b) closed crack and (c) open crack configurations.

D.1 Artificial Crack System Geometry

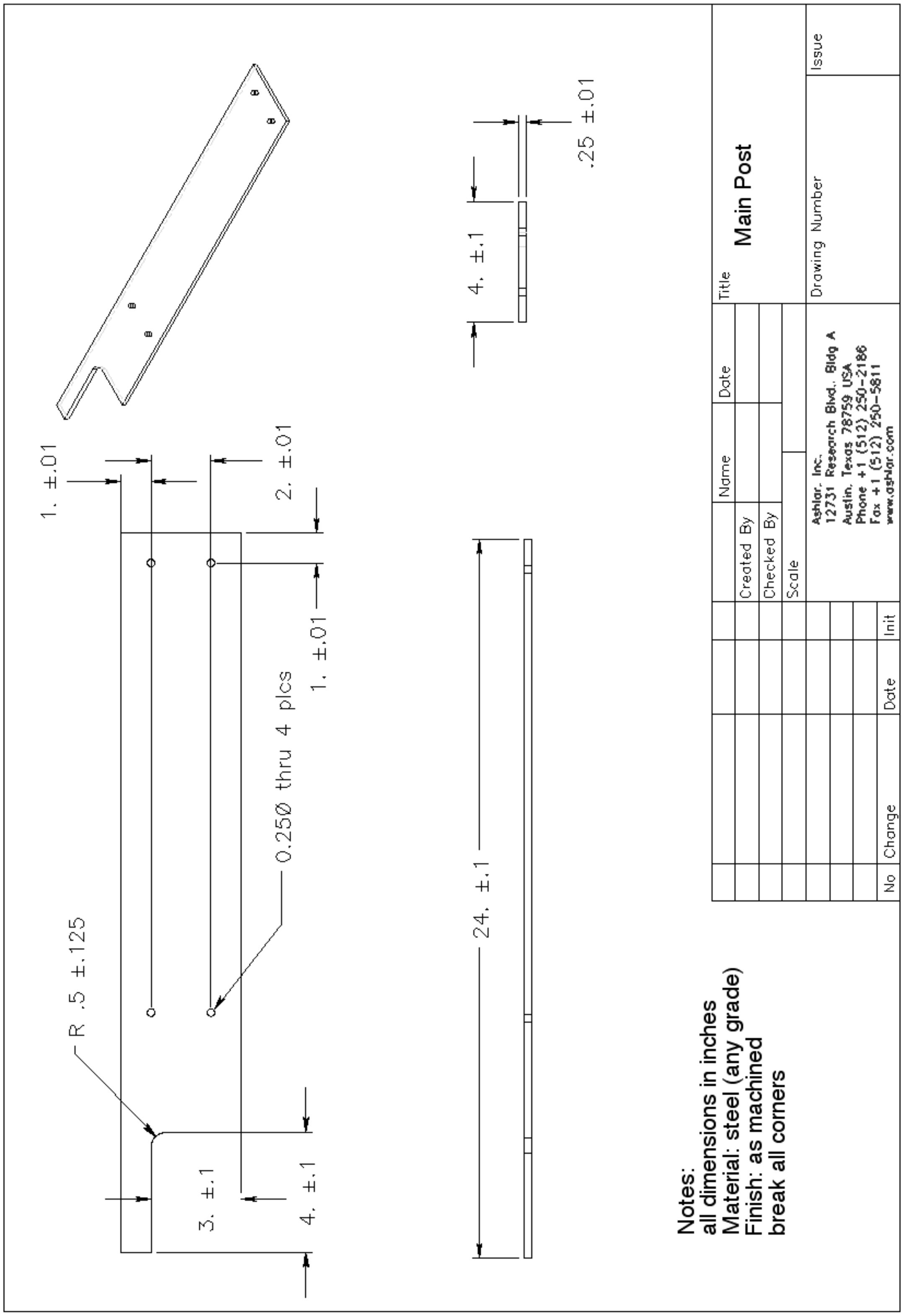

Figure D-2: Drawing of Artificial Crack System Main Post

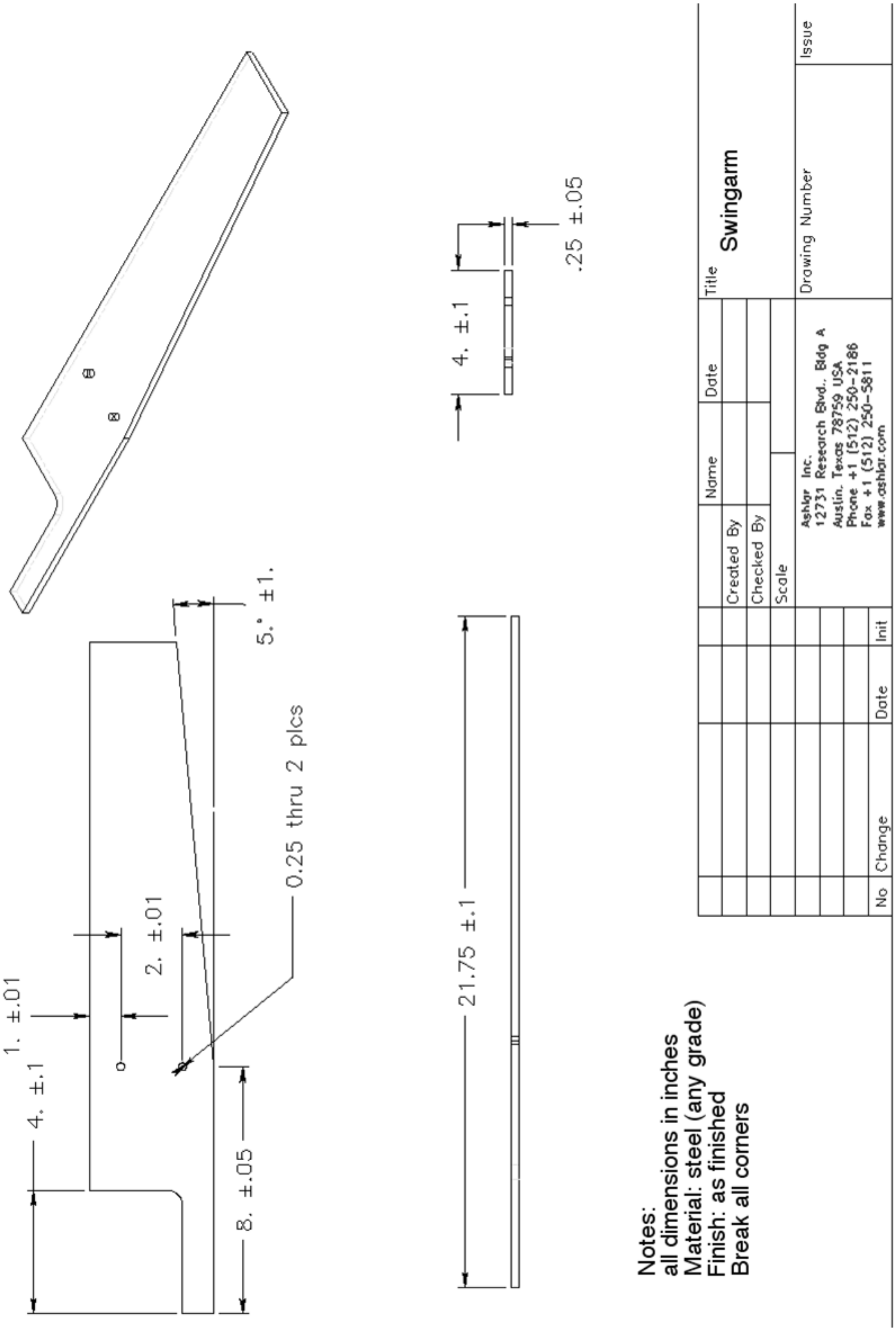

Figure D-3: Drawing of Artificial Crack System Swing-arm.

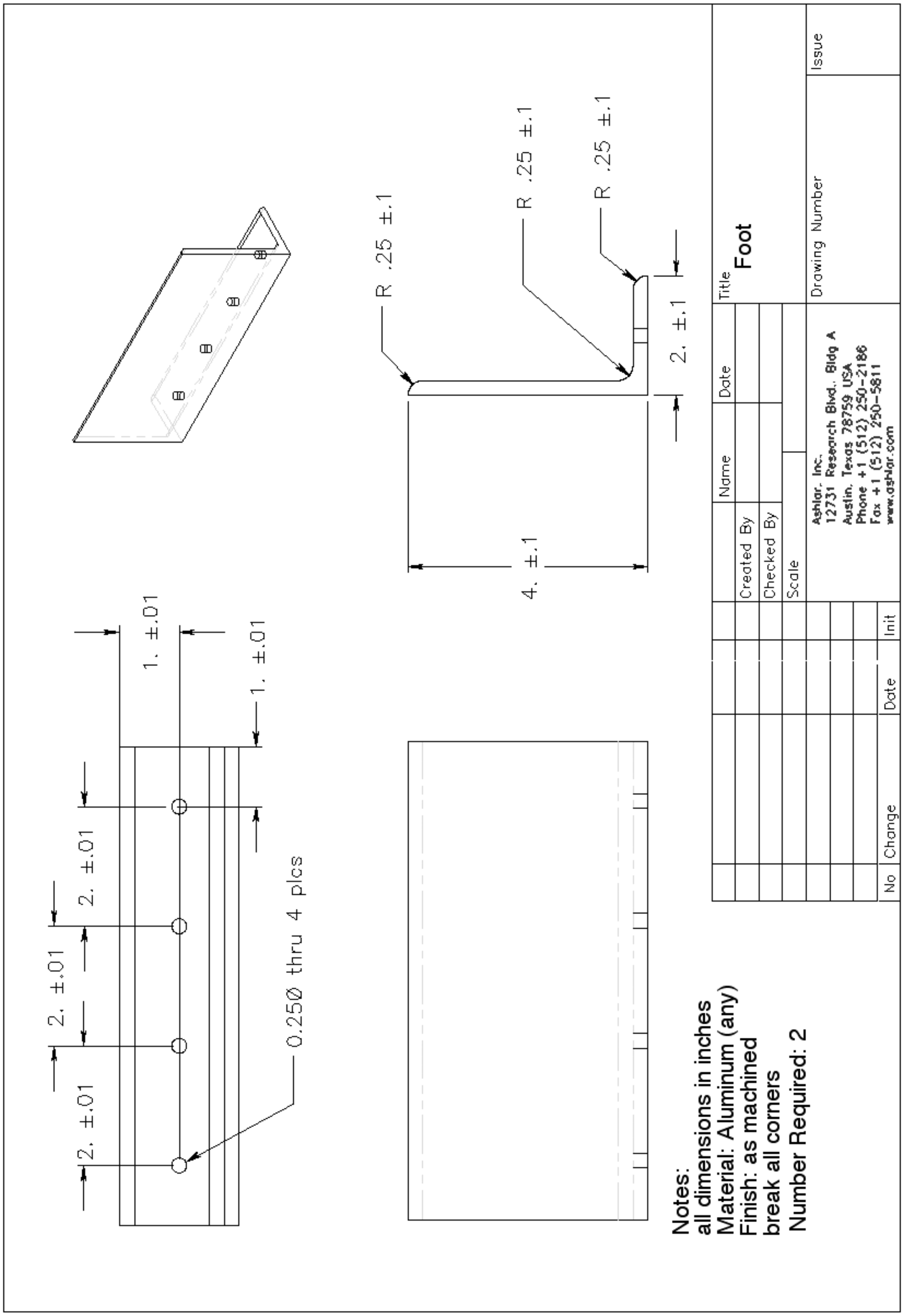

Figure D-4: Drawing of Artificial Crack System Foot.

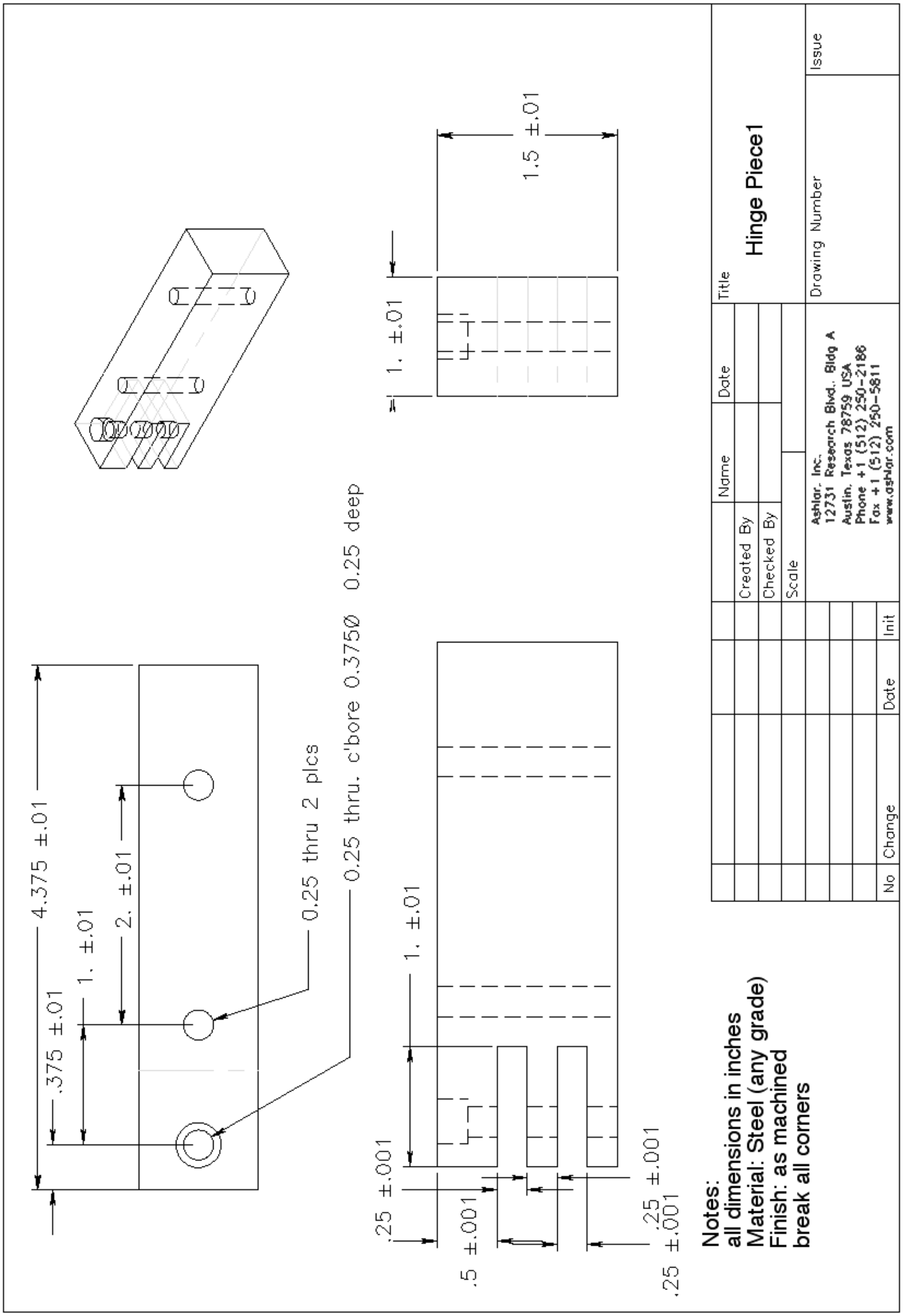

Figure D-5: Drawing of Artificial Crack System Hinge Piece 1.

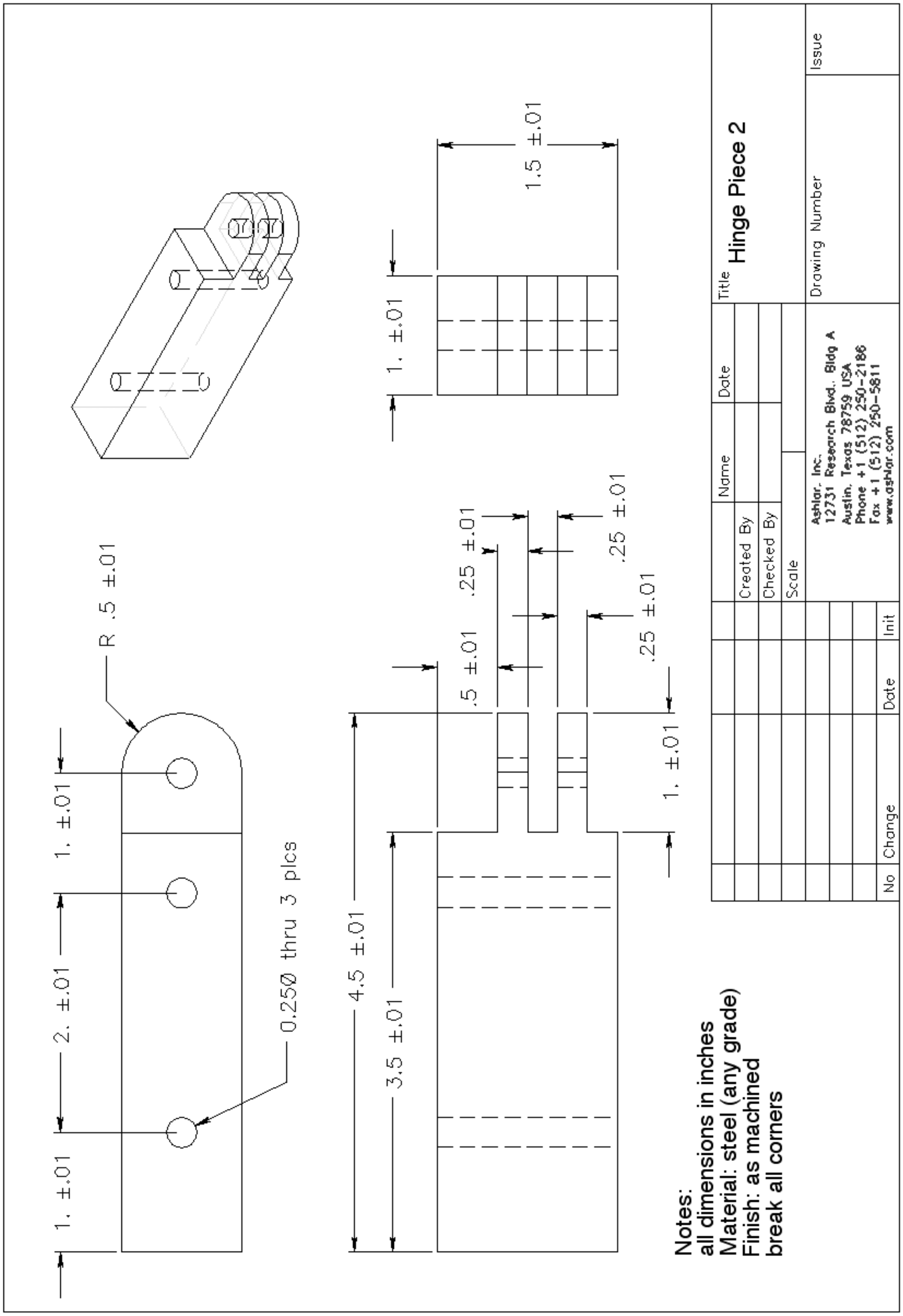

Figure D-6: Drawing of Artificial Crack System Hinge Piece 2.

D.2 Artificial Crack System Experimental Data

Table D-1: Artificial Crack System experimental results

Distance from Crack Center		Reading at 60 seconds
mm	**in**	**mV**
0	0	2
10	0.394	1
20	0.787	1
30	1.18	1
40	1.57	2
50	1.97	2
100	3.94	4
150	5.91	6
200	7.87	8
250	9.84	10
300	11.8	12

APPENDIX E: ACRYLIC SPECIMEN TEST DOCUMENTS

E.1 ASTM E399 Geometry

Compact C(T) Specimen - Standard Proportions and Tolerances in Metric Units (ASTM 2012)

Thickness, B $B = 38.1\cdot mm$

$W := 2\cdot B = 76.2\cdot mm$

$1.25\cdot W = 95.25\cdot mm$

$0.25\cdot W = 19.05\cdot mm$

$0.275\cdot W = 20.955\cdot mm$

$0.6\cdot W = 45.72\cdot mm$

$a := 0.5\cdot W = 38.1\cdot mm$ $crack_{fatigue} := \max(0.025\cdot W, 0.05in) = 1.905\cdot mm$

$a - crack_{fatigue} = 36.195\cdot mm$

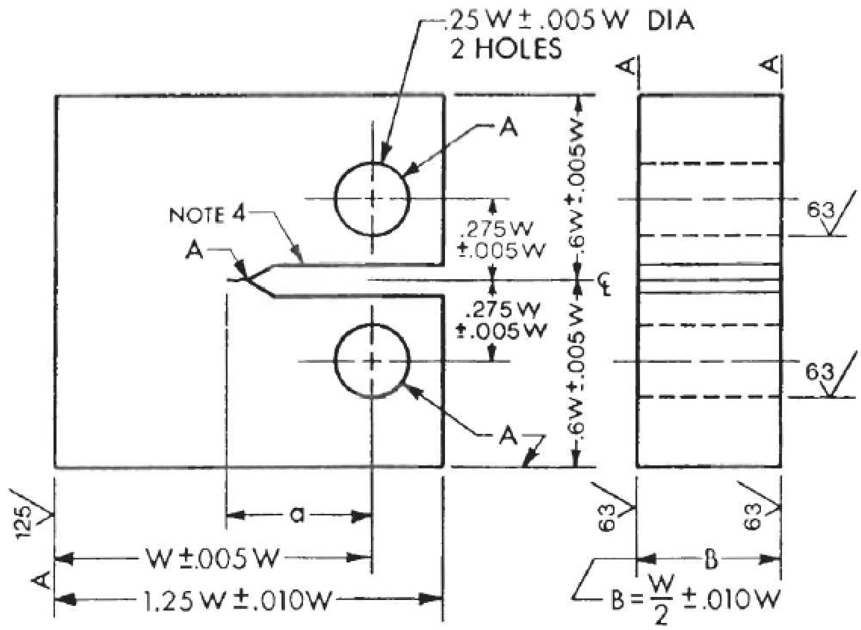

Compact C(T) Specimen - Standard Proportions and Tolerances in English Units (ASTM 2012)

Thickness, B $B := 1.5\text{in}$

$W := 2 \cdot B = 3\text{ in}$

$1.25 \cdot W = 3.75\text{ in}$

$0.25 \cdot W = 0.75\text{ in}$

$0.275 \cdot W = 0.825\text{ in}$

$0.6 \cdot W = 1.8\text{ in}$

$a := 0.5 \cdot W = 1.5\text{ in}$ $\text{crack}_{\text{fatigue}} := \max(0.025 \cdot W, 0.05\text{in}) = 0.075\text{ in}$

$a - \text{crack}_{\text{fatigue}} = 1.425\text{ in}$

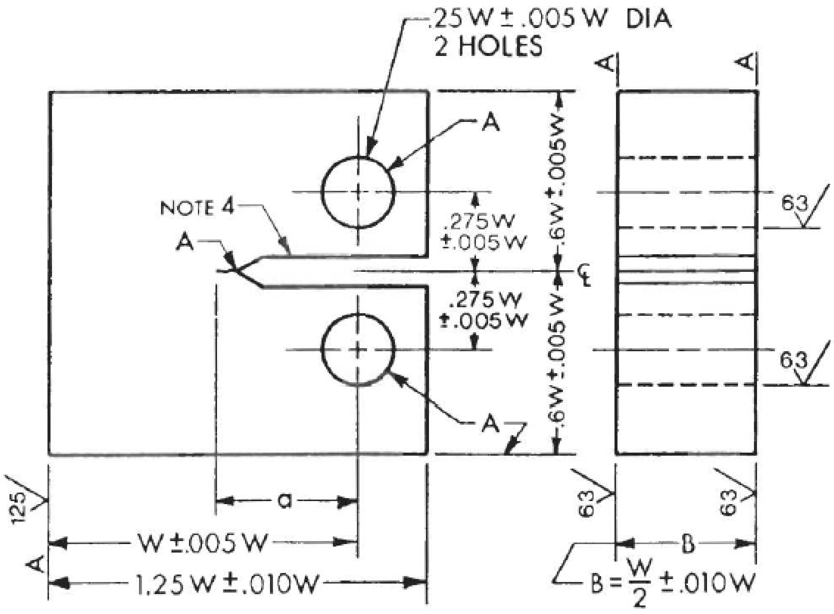

E.2 Compact Tension Specimen Drawings

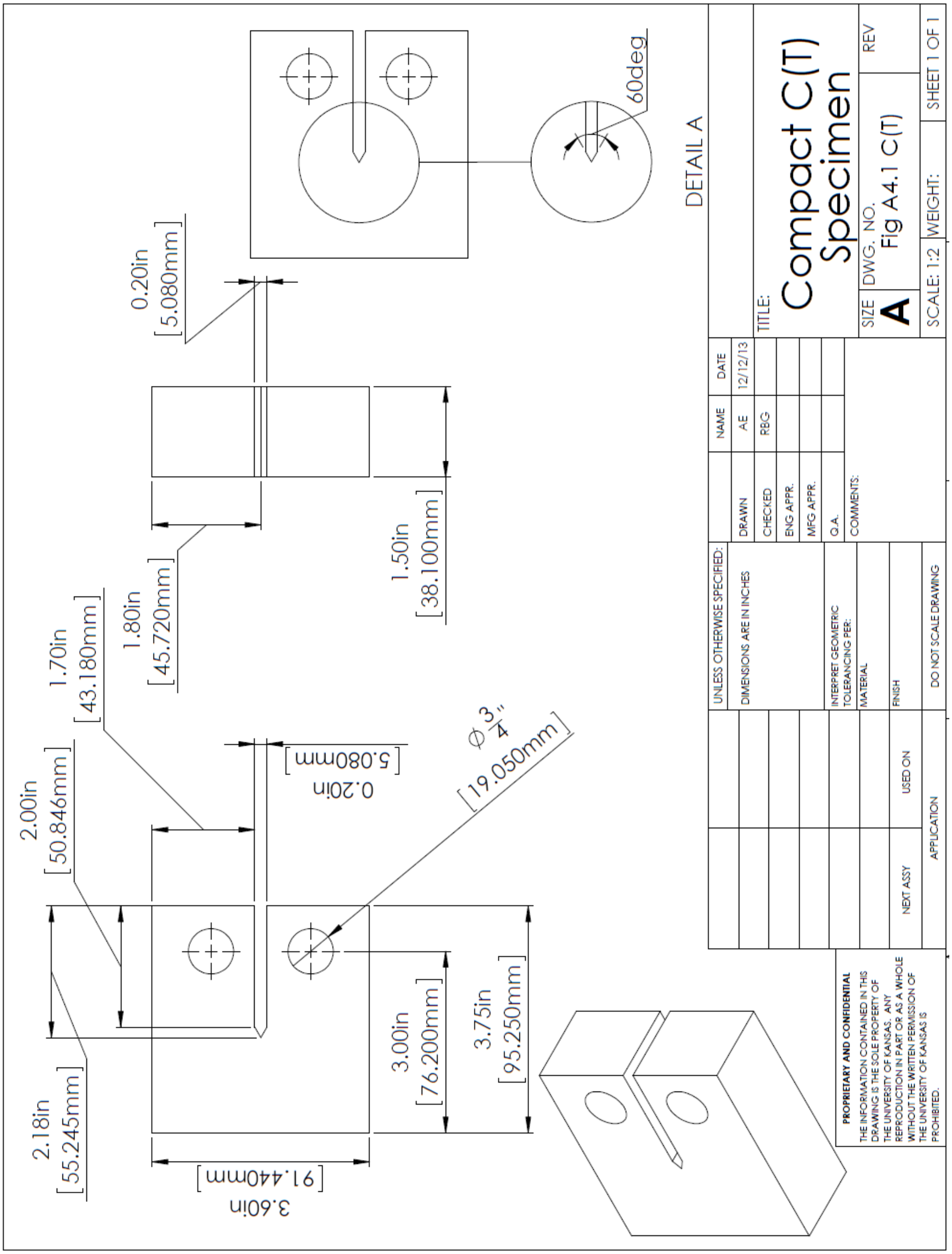

Figure E-1: Acrylic specimen geometry.

E.3 Acrylic Specimen Dynamic Test Results

Table E-1: Experimental results for acrylic proof of concept testing.

Distance from Crack Tip		Voltage Reading at 60 sec.
mm	**in**	**(mV)**
50	1.969	0
40	1.575	2.42
30	1.181	1.83
20	0.787	1.35
10	0.394	0.813
0	0	0.423
-10	-0.394	0.308
-20	-0.787	0.226

Figure E-2: Acrylic specimen test voltage reading results at distances ahead and behind the crack tip boundary with linear trend lines.

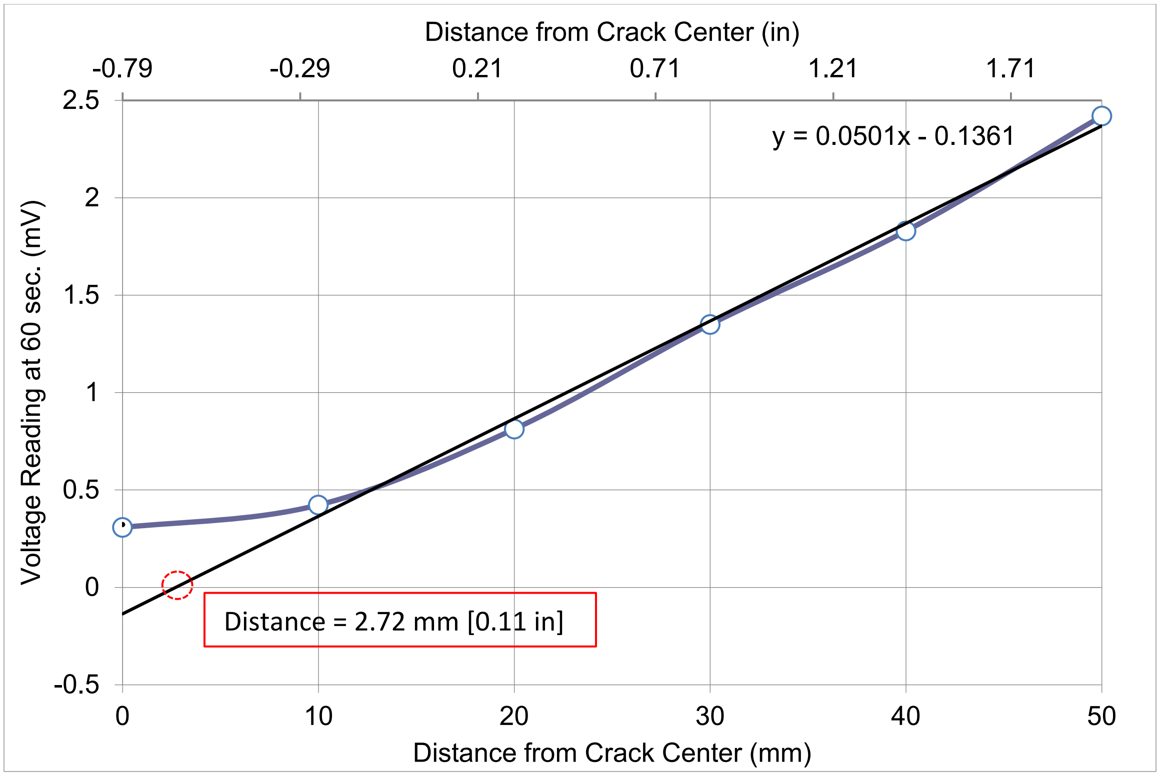

Figure E-3: Acrylic specimen test voltage reading results at distances behind the crack tip and the approximated crack tip boundary location using the using the extension on the linear portion of the results and zero voltage.

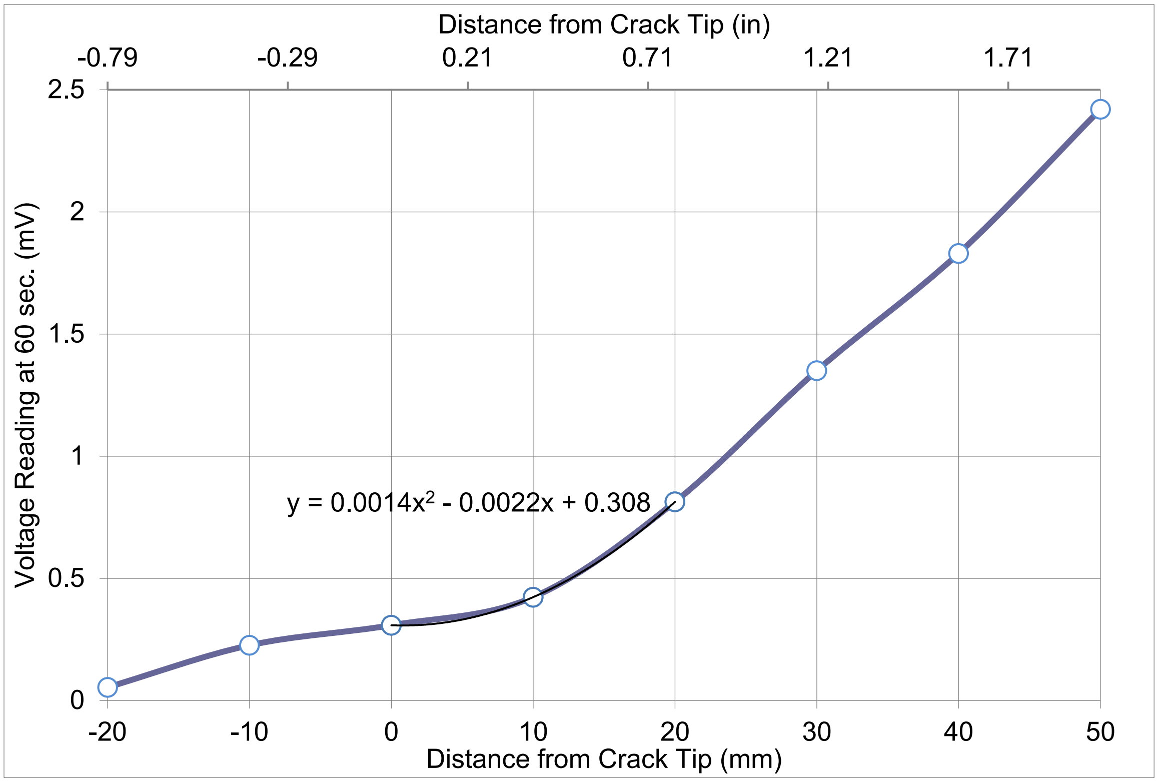

Figure E-4: Acrylic specimen test voltage reading results at distances behind the crack tip and the equation of the non-linear section used in the crack tip location analysis.

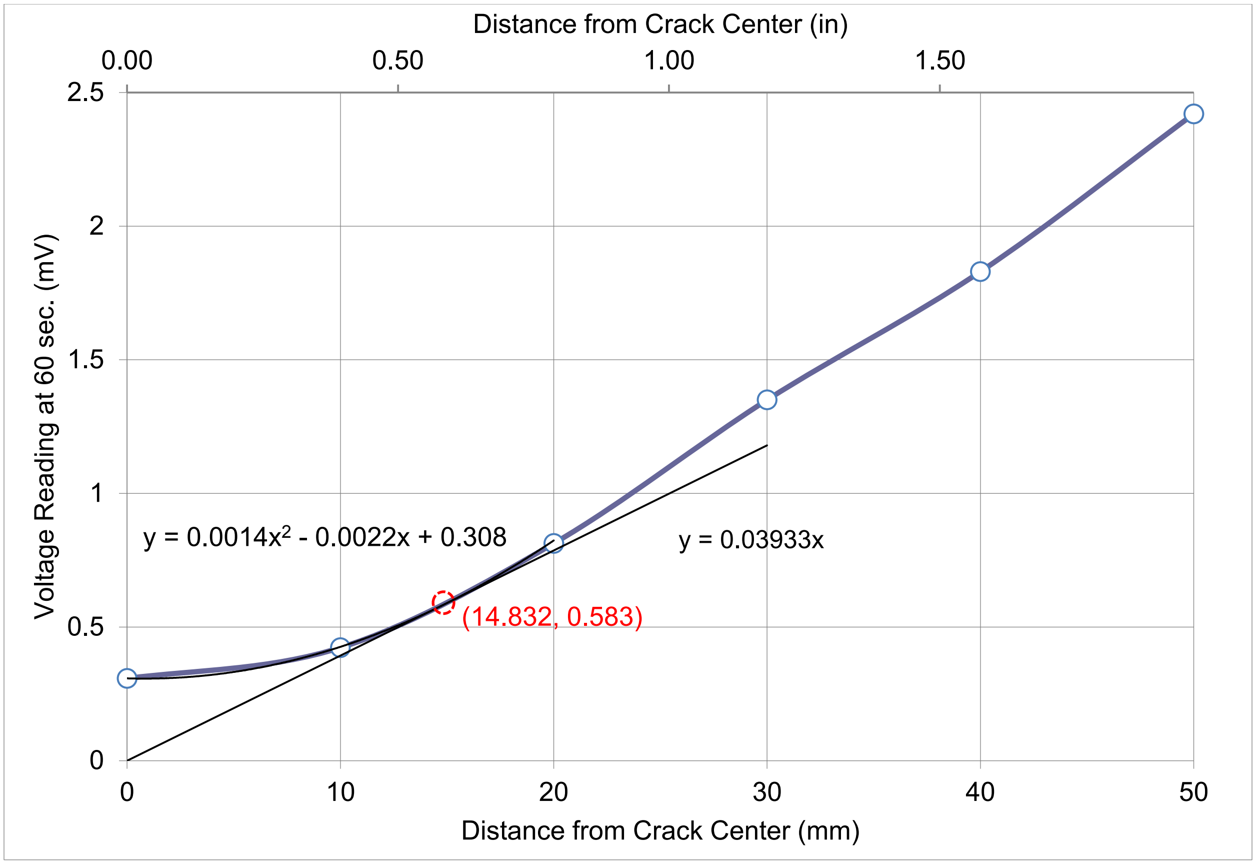

Figure E-5: Acrylic specimen test voltage reading results at distances behind the crack tip and the equations of the non-linear section used in the crack tip location analysis and the line tangent to the non-linear region through the crack tip boundary.

E.4 Calculation of Crack Tip Boundary Location

Given the equation on the 2nd order polynomial non-linear portion of the voltage readings, $y_{nonlinear}$, as a function of distance from the crack tip, x.

$$y_{nonlinear}(x) = 0.0014x^2 - 0.0022x + 0.308$$

The derivative of the non-linear equation, or the slope of the curve, $y'_{nonlinear,}$ yields

$$y'_{nonlinear}(x) = \frac{d}{dx} y_{nonlinear}(x) \rightarrow 0.0028 \cdot x - 0.0022$$

The slope of the straight line through a point (X, Y) on the curve and (0,0) is given by

$$\frac{Y - 0}{X - 0} \rightarrow \frac{Y}{X}$$

Setting the curve slope equal to the slope of the straight line

$$\frac{Y}{X} = y'_{nonlinear}$$

if $\quad Y = y_{nonlinear} \quad$ and $\quad X = x$

then,

$$\frac{y_{nonlinear}(x)}{x} = y'_{nonlinear}(x) \text{ solve}, x \rightarrow \begin{pmatrix} -14.832 \\ 14.832 \end{pmatrix}$$

Since we are using distances behind the crack tip,

$$x = 14.832 \quad \text{mm}$$

Substitution of x into the curve, yields

$$y_{nonlinear}(x) = 0.583 \quad \text{mV}$$

The point (14.832, 0.583) on the curve and (0,0) provide two points of the straight line, and using the slope, m, and the point slope equation

$m = \dfrac{y_{nonlinear}(x)}{x} = 0.039$ and point $\quad y_1 = 0 \quad x_1 = 0$

Therefore, the quation on the line tangent to the non-linear portion of the results and through a point of zero voltage and the crack tip can be written as:

$$y(x) = m \cdot (x - x_1) + y_1 \rightarrow y(x) = 0.03933 \cdot x$$

or

$$\boxed{y = 0.03933x}$$

E.5 Acrylic Compact Tension Specimen Ultimate Load

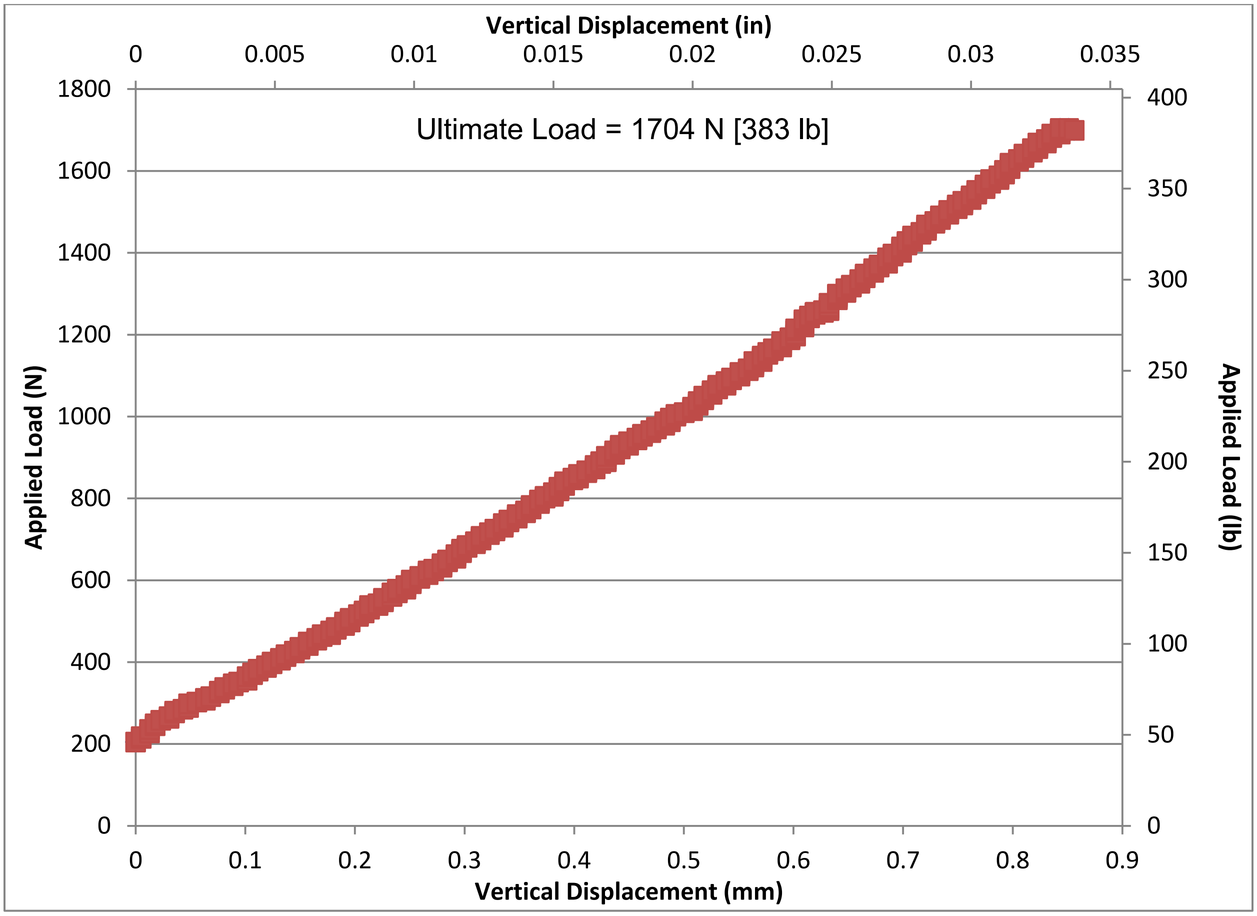

Figure E-6: Ultimate load of 1704 N [383 lb] determined experimentally for the acrylic specimen material used in the PACTS tool proof of concept testing.

Table E-2: Acrylic compact tension specimen ultimate load test data.

	Vertical Position		Load			Vertical Position		Load	
	mm	in	N	lb		mm	in	N	lb
1	0	0	204.608	46	41	0.13716	0.0054	418.112	94
2	0.00508	0.0002	213.504	48	42	0.14478	0.0057	422.56	95
3	0.00508	0.0002	217.952	49	43	0.14478	0.0057	427.008	96
4	0.0127	0.0005	226.848	51	44	0.14986	0.0059	431.456	97
5	0.0127	0.0005	235.744	53	45	0.14986	0.0059	435.904	98
6	0.01778	0.0007	244.64	55	46	0.14986	0.0059	435.904	98
7	0.01778	0.0007	249.088	56	47	0.15748	0.0062	440.352	99
8	0.02286	0.0009	257.984	58	48	0.15748	0.0062	444.8	100
9	0.03048	0.0012	262.432	59	49	0.15748	0.0062	449.248	101
10	0.03048	0.0012	266.88	60	50	0.1651	0.0065	453.696	102
11	0.03556	0.0014	275.776	62	51	0.1651	0.0065	453.696	102
12	0.03556	0.0014	280.224	63	52	0.1651	0.0065	458.144	103
13	0.04318	0.0017	284.672	64	53	0.17018	0.0067	462.592	104
14	0.04826	0.0019	289.12	65	54	0.17018	0.0067	467.04	105
15	0.04826	0.0019	298.016	67	55	0.1778	0.007	467.04	105
16	0.05588	0.0022	302.464	68	56	0.1778	0.007	471.488	106
17	0.0635	0.0025	306.912	69	57	0.1778	0.007	475.936	107
18	0.0635	0.0025	311.36	70	58	0.18288	0.0072	480.384	108
19	0.06858	0.0027	315.808	71	59	0.18288	0.0072	480.384	108
20	0.0762	0.003	324.704	73	60	0.18288	0.0072	484.832	109
21	0.0762	0.003	329.152	74	61	0.1905	0.0075	489.28	110
22	0.08128	0.0032	333.6	75	62	0.1905	0.0075	493.728	111
23	0.08128	0.0032	338.048	76	63	0.1905	0.0075	498.176	112
24	0.0889	0.0035	342.496	77	64	0.19558	0.0077	498.176	112
25	0.0889	0.0035	346.944	78	65	0.19558	0.0077	502.624	113
26	0.09398	0.0037	351.392	79	66	0.19558	0.0077	507.072	114
27	0.1016	0.004	355.84	80	67	0.2032	0.008	511.52	115
28	0.1016	0.004	364.736	82	68	0.2032	0.008	515.968	116
29	0.10668	0.0042	369.184	83	69	0.2032	0.008	515.968	116
30	0.10668	0.0042	373.632	84	70	0.20828	0.0082	520.416	117
31	0.11176	0.0044	378.08	85	71	0.20828	0.0082	520.416	117
32	0.11176	0.0044	382.528	86	72	0.20828	0.0082	524.864	118
33	0.11938	0.0047	386.976	87	73	0.21336	0.0084	529.312	119
34	0.11938	0.0047	391.424	88	74	0.21336	0.0084	533.76	120
35	0.12446	0.0049	395.872	89	75	0.21336	0.0084	538.208	121
36	0.12446	0.0049	400.32	90	76	0.22098	0.0087	538.208	121
37	0.13208	0.0052	404.768	91	77	0.22098	0.0087	542.656	122
38	0.13208	0.0052	404.768	91	78	0.22606	0.0089	547.104	123
39	0.13208	0.0052	409.216	92	79	0.22606	0.0089	551.552	124
40	0.13716	0.0054	413.664	93	80	0.22606	0.0089	556	125

	Vertical Position		Load			Vertical Position		Load	
	mm	in	N	lb		mm	in	N	lb
81	0.23368	0.0092	560.448	126	121	0.31496	0.0124	707.232	159
82	0.23368	0.0092	560.448	126	122	0.32258	0.0127	711.68	160
83	0.23368	0.0092	569.344	128	123	0.32258	0.0127	716.128	161
84	0.23876	0.0094	569.344	128	124	0.32766	0.0129	720.576	162
85	0.23876	0.0094	573.792	129	125	0.32766	0.0129	725.024	163
86	0.23876	0.0094	578.24	130	126	0.32766	0.0129	725.024	163
87	0.24638	0.0097	578.24	130	127	0.33528	0.0132	729.472	164
88	0.24638	0.0097	582.688	131	128	0.33528	0.0132	733.92	165
89	0.24638	0.0097	587.136	132	129	0.33528	0.0132	738.368	166
90	0.25146	0.0099	591.584	133	130	0.34036	0.0134	742.816	167
91	0.25146	0.0099	596.032	134	131	0.34036	0.0134	742.816	167
92	0.25146	0.0099	600.48	135	132	0.34036	0.0134	747.264	168
93	0.25908	0.0102	604.928	136	133	0.34798	0.0137	751.712	169
94	0.25908	0.0102	604.928	136	134	0.34798	0.0137	756.16	170
95	0.25908	0.0102	609.376	137	135	0.34798	0.0137	760.608	171
96	0.2667	0.0105	613.824	138	136	0.3556	0.014	765.056	172
97	0.2667	0.0105	618.272	139	137	0.3556	0.014	765.056	172
98	0.2667	0.0105	622.72	140	138	0.3556	0.014	769.504	173
99	0.27178	0.0107	622.72	140	139	0.36068	0.0142	773.952	174
100	0.27178	0.0107	627.168	141	140	0.36068	0.0142	778.4	175
101	0.2794	0.011	631.616	142	141	0.36068	0.0142	782.848	176
102	0.2794	0.011	636.064	143	142	0.3683	0.0145	787.296	177
103	0.2794	0.011	640.512	144	143	0.3683	0.0145	791.744	178
104	0.28448	0.0112	644.96	145	144	0.3683	0.0145	791.744	178
105	0.28448	0.0112	649.408	146	145	0.3683	0.0145	796.192	179
106	0.28448	0.0112	649.408	146	146	0.37338	0.0147	800.64	180
107	0.2921	0.0115	653.856	147	147	0.37338	0.0147	805.088	181
108	0.2921	0.0115	658.304	148	148	0.381	0.015	805.088	181
109	0.2921	0.0115	662.752	149	149	0.381	0.015	809.536	182
110	0.29718	0.0117	667.2	150	150	0.381	0.015	813.984	183
111	0.29718	0.0117	671.648	151	151	0.38608	0.0152	818.432	184
112	0.29718	0.0117	676.096	152	152	0.38608	0.0152	822.88	185
113	0.30226	0.0119	680.544	153	153	0.38608	0.0152	827.328	186
114	0.30226	0.0119	680.544	153	154	0.39116	0.0154	831.776	187
115	0.30226	0.0119	684.992	154	155	0.39116	0.0154	831.776	187
116	0.30988	0.0122	689.44	155	156	0.39116	0.0154	836.224	188
117	0.30988	0.0122	693.888	156	157	0.39116	0.0154	840.672	189
118	0.30988	0.0122	693.888	156	158	0.39878	0.0157	845.12	190
119	0.31496	0.0124	698.336	157	159	0.39878	0.0157	849.568	191
120	0.31496	0.0124	702.784	158	160	0.40386	0.0159	849.568	191

	Vertical Position		Load			Vertical Position		Load	
	mm	in	N	lb		mm	in	N	lb
161	0.40386	0.0159	854.016	192	201	0.49276	0.0194	1000.8	225
162	0.40386	0.0159	858.464	193	202	0.49276	0.0194	1005.248	226
163	0.41148	0.0162	862.912	194	203	0.50038	0.0197	1009.696	227
164	0.41148	0.0162	867.36	195	204	0.50038	0.0197	1009.696	227
165	0.41148	0.0162	867.36	195	205	0.508	0.02	1014.144	228
166	0.4191	0.0165	871.808	196	206	0.508	0.02	1018.592	229
167	0.4191	0.0165	876.256	197	207	0.508	0.02	1023.04	230
168	0.4191	0.0165	880.704	198	208	0.51308	0.0202	1027.488	231
169	0.42418	0.0167	885.152	199	209	0.51308	0.0202	1031.936	232
170	0.42418	0.0167	889.6	200	210	0.51308	0.0202	1036.384	233
171	0.42418	0.0167	889.6	200	211	0.51816	0.0204	1040.832	234
172	0.42926	0.0169	889.6	200	212	0.51816	0.0204	1045.28	235
173	0.42926	0.0169	894.048	201	213	0.51816	0.0204	1049.728	236
174	0.42926	0.0169	902.944	203	214	0.52578	0.0207	1054.176	237
175	0.43688	0.0172	907.392	204	215	0.52578	0.0207	1058.624	238
176	0.43688	0.0172	911.84	205	216	0.52578	0.0207	1063.072	239
177	0.43688	0.0172	916.288	206	217	0.53086	0.0209	1067.52	240
178	0.44196	0.0174	920.736	207	218	0.53086	0.0209	1071.968	241
179	0.44196	0.0174	925.184	208	219	0.53086	0.0209	1076.416	242
180	0.44196	0.0174	929.632	209	220	0.53848	0.0212	1076.416	242
181	0.44958	0.0177	929.632	209	221	0.53848	0.0212	1080.864	243
182	0.44958	0.0177	934.08	210	222	0.53848	0.0212	1085.312	244
183	0.44958	0.0177	938.528	211	223	0.54356	0.0214	1089.76	245
184	0.4572	0.018	942.976	212	224	0.54356	0.0214	1094.208	246
185	0.4572	0.018	942.976	212	225	0.54356	0.0214	1094.208	246
186	0.4572	0.018	947.424	213	226	0.55118	0.0217	1098.656	247
187	0.46228	0.0182	951.872	214	227	0.55118	0.0217	1103.104	248
188	0.46228	0.0182	956.32	215	228	0.55118	0.0217	1107.552	249
189	0.46228	0.0182	956.32	215	229	0.5588	0.022	1112	250
190	0.4699	0.0185	960.768	216	230	0.5588	0.022	1116.448	251
191	0.4699	0.0185	965.216	217	231	0.5588	0.022	1116.448	251
192	0.4699	0.0185	965.216	217	232	0.56388	0.0222	1120.896	252
193	0.47498	0.0187	969.664	218	233	0.56388	0.0222	1125.344	253
194	0.47498	0.0187	974.112	219	234	0.56388	0.0222	1129.792	254
195	0.4826	0.019	978.56	220	235	0.56388	0.0222	1134.24	255
196	0.4826	0.019	983.008	221	236	0.5715	0.0225	1134.24	255
197	0.4826	0.019	987.456	222	237	0.5715	0.0225	1138.688	256
198	0.48768	0.0192	987.456	222	238	0.5715	0.0225	1143.136	257
199	0.48768	0.0192	991.904	223	239	0.5715	0.0225	1147.584	258
200	0.48768	0.0192	996.352	224	240	0.57658	0.0227	1152.032	259

	Vertical Position		Load			Vertical Position		Load	
	mm	in	N	lb		mm	in	N	lb
241	0.57658	0.0227	1152.032	259	281	0.6477	0.0255	1303.264	293
242	0.57658	0.0227	1156.48	260	282	0.6477	0.0255	1303.264	293
243	0.58166	0.0229	1160.928	261	283	0.6477	0.0255	1307.712	294
244	0.58166	0.0229	1165.376	262	284	0.6477	0.0255	1312.16	295
245	0.58166	0.0229	1165.376	262	285	0.65278	0.0257	1316.608	296
246	0.58928	0.0232	1169.824	263	286	0.65278	0.0257	1316.608	296
247	0.58928	0.0232	1174.272	264	287	0.65278	0.0257	1321.056	297
248	0.58928	0.0232	1178.72	265	288	0.6604	0.026	1325.504	298
249	0.58928	0.0232	1183.168	266	289	0.6604	0.026	1325.504	298
250	0.5969	0.0235	1187.616	267	290	0.6604	0.026	1329.952	299
251	0.5969	0.0235	1192.064	268	291	0.6604	0.026	1334.4	300
252	0.5969	0.0235	1192.064	268	292	0.66548	0.0262	1338.848	301
253	0.60198	0.0237	1196.512	269	293	0.66548	0.0262	1343.296	302
254	0.60198	0.0237	1200.96	270	294	0.66548	0.0262	1347.744	303
255	0.60198	0.0237	1209.856	272	295	0.66548	0.0262	1347.744	303
256	0.60198	0.0237	1214.304	273	296	0.6731	0.0265	1352.192	304
257	0.6096	0.024	1218.752	274	297	0.6731	0.0265	1356.64	305
258	0.6096	0.024	1223.2	275	298	0.6731	0.0265	1361.088	306
259	0.6096	0.024	1227.648	276	299	0.67818	0.0267	1365.536	307
260	0.6096	0.024	1232.096	277	300	0.67818	0.0267	1365.536	307
261	0.6096	0.024	1236.544	278	301	0.67818	0.0267	1369.984	308
262	0.61468	0.0242	1240.992	279	302	0.6858	0.027	1374.432	309
263	0.61468	0.0242	1240.992	279	303	0.6858	0.027	1378.88	310
264	0.61468	0.0242	1245.44	280	304	0.6858	0.027	1383.328	311
265	0.61468	0.0242	1245.44	280	305	0.6858	0.027	1387.776	312
266	0.61976	0.0244	1249.888	281	306	0.69088	0.0272	1392.224	313
267	0.61976	0.0244	1249.888	281	307	0.69088	0.0272	1396.672	314
268	0.61976	0.0244	1254.336	282	308	0.69088	0.0272	1396.672	314
269	0.61976	0.0244	1254.336	282	309	0.6985	0.0275	1401.12	315
270	0.61976	0.0244	1254.336	282	310	0.6985	0.0275	1405.568	316
271	0.62738	0.0247	1254.336	282	311	0.6985	0.0275	1410.016	317
272	0.62738	0.0247	1258.784	283	312	0.6985	0.0275	1414.464	318
273	0.63246	0.0249	1258.784	283	313	0.70358	0.0277	1418.912	319
274	0.63246	0.0249	1263.232	284	314	0.70358	0.0277	1423.36	320
275	0.63246	0.0249	1267.68	285	315	0.70358	0.0277	1427.808	321
276	0.63246	0.0249	1276.576	287	316	0.70866	0.0279	1427.808	321
277	0.64008	0.0252	1285.472	289	317	0.70866	0.0279	1432.256	322
278	0.64008	0.0252	1289.92	290	318	0.70866	0.0279	1436.704	323
279	0.64008	0.0252	1294.368	291	319	0.70866	0.0279	1441.152	324
280	0.64008	0.0252	1298.816	292	320	0.71628	0.0282	1445.6	325

	Vertical Position		Load			Vertical Position		Load	
	mm	in	N	lb		mm	in	N	lb
321	0.71628	0.0282	1445.6	325	361	0.79248	0.0312	1596.832	359
322	0.71628	0.0282	1450.048	326	362	0.79248	0.0312	1601.28	360
323	0.72136	0.0284	1454.496	327	363	0.79248	0.0312	1601.28	360
324	0.72136	0.0284	1458.944	328	364	0.79756	0.0314	1605.728	361
325	0.72136	0.0284	1463.392	329	365	0.79756	0.0314	1610.176	362
326	0.72136	0.0284	1467.84	330	366	0.79756	0.0314	1614.624	363
327	0.72898	0.0287	1472.288	331	367	0.79756	0.0314	1619.072	364
328	0.72898	0.0287	1472.288	331	368	0.80518	0.0317	1623.52	365
329	0.72898	0.0287	1476.736	332	369	0.80518	0.0317	1627.968	366
330	0.73406	0.0289	1481.184	333	370	0.80518	0.0317	1627.968	366
331	0.73406	0.0289	1485.632	334	371	0.81026	0.0319	1632.416	367
332	0.73406	0.0289	1490.08	335	372	0.81026	0.0319	1636.864	368
333	0.74168	0.0292	1494.528	336	373	0.81026	0.0319	1641.312	369
334	0.74168	0.0292	1494.528	336	374	0.81788	0.0322	1645.76	370
335	0.74168	0.0292	1498.976	337	375	0.81788	0.0322	1650.208	371
336	0.74168	0.0292	1503.424	338	376	0.81788	0.0322	1654.656	372
337	0.7493	0.0295	1507.872	339	377	0.82296	0.0324	1654.656	372
338	0.7493	0.0295	1512.32	340	378	0.82296	0.0324	1659.104	373
339	0.7493	0.0295	1516.768	341	379	0.82296	0.0324	1663.552	374
340	0.75438	0.0297	1516.768	341	380	0.82296	0.0324	1668	375
341	0.75438	0.0297	1521.216	342	381	0.83058	0.0327	1668	375
342	0.75438	0.0297	1525.664	343	382	0.83058	0.0327	1672.448	376
343	0.762	0.03	1530.112	344	383	0.83058	0.0327	1676.896	377
344	0.762	0.03	1534.56	345	384	0.83566	0.0329	1681.344	378
345	0.762	0.03	1534.56	345	385	0.83566	0.0329	1685.792	379
346	0.762	0.03	1539.008	346	386	0.83566	0.0329	1690.24	380
347	0.76708	0.0302	1543.456	347	387	0.84328	0.0332	1690.24	380
348	0.76708	0.0302	1547.904	348	388	0.84328	0.0332	1694.688	381
349	0.76708	0.0302	1552.352	349	389	0.84328	0.0332	1699.136	382
350	0.7747	0.0305	1556.8	350	390	0.84328	0.0332	1703.584	383
351	0.7747	0.0305	1561.248	351	391	0.8509	0.0335	1703.584	383
352	0.7747	0.0305	1561.248	351	392	0.85598	0.0337	1699.136	382
353	0.7747	0.0305	1565.696	352	393	0.9779	0.0385	987.456	222
354	0.77978	0.0307	1570.144	353	394	1.10236	0.0434	542.656	122
355	0.77978	0.0307	1574.592	354	395	1.22428	0.0482	302.464	68
356	0.77978	0.0307	1579.04	355					
357	0.7874	0.031	1579.04	355					
358	0.7874	0.031	1583.488	356					
359	0.7874	0.031	1587.936	357					
360	0.79248	0.0312	1592.384	358					